Monitoring of the mechanical properties of the crust beneath Japan from continuous data of the Hi-net network

Qing-Yu Wang

UNIVERSITÉ GRENOBLE ALPES

THÈSE

Pour obtenir le grade de

DOCTEUR DE LA COMMUNAUTE UNIVERSITÉ GRENOBLE ALPES

Spécialité : **Terre Solide (CETSOL)**

Arrêté ministériel : 25 mai 2016

Présentée par

Qing-Yu WANG

Thèse dirigée par **Michel CAMPILLO** , Professeur, UGA,
et codirigée par **Florent BRENGUIER** , Physicien d'Observatoire, UGA, et
codirigée par **Robert D. van der Hilst** , Professeur, MIT.

préparée au sein de **l'Institut des Sciences de la Terre**
et de l'école doctorale **Terre Univers Environnement**

Suivi temporel des propriétés mécaniques de la croûte sous le Japon à partir de données de bruit de fond sismique.

Thèse soutenue publiquement le **19 Décembre 2018**,
devant le jury composé de :

Takeshi Nishimura
Professeur, Tohoku University, Sendai, Japan, Rapporteur

Huajian Yao
Professor, University of Science and Technology of China, Hefei, China, Rapporteur

Anne Paul
Directrice de recherche CNRS, ISTerre, Grenoble, France, Présidente

Bérénice Froment
Research engineer, IRSN, Paris, France, Examinatrice

Robert D. van der Hilst
Professor, Massachusetts Institute of Technology, Boston, United States, Invité

Florent Brenguier
Physicien d'Observatoire, ISTerre, Grenoble, France, Co-Directeur de thèse

Michel CAMPILLO
Professeur, Université Grenoble Alpes, Grenoble, France, Co-Directeur de thèse

Remerciements

First, I would like to express my sincere gratitude to my supervisors, professor Michel Campillo, professor Florent Brenguier, and professor Robert D. Van der Hilst, whose patient and forward-looking guidance and constant encouragement are the most important guarantees for the smooth completion of this thesis. You all inspire me a lot with your positive attitude and serious-minded way of working. I really appreciate having the opportunity to work with all of you.

I started my first internship with Michel from the end of the first year of Master in 2014. The primary mission is to read the 2^{nd} edition of "Seismic wave propagation and scattering in the heterogeneous Earth" by professor Haruo Sato and to model the seismic waves energy based on the 2-D radiative transfer equations. Then I started to work on the ambient noise-based seismic monitoring with both Michel and Florent since the final internship of Master in 2015. Both internships deepened my passion for geophysics. And then I was fortunate enough to have the opportunity to continue working with them on noise-based monitoring in Japan.

Also, I would like to express my sincere gratitude

- especially to Albanne Lecointre, for her firm technical support and help during this thesis.

- to all our collaborators and all members in the "Ondes et Structures" group, for who give me a lot of support at work. I appreciate your inputs and all the discussions with you.

- to my jury members :

Takeshi Nishimura, Huajian Yao, Anne Paul, and Bérénice Froment, for whose careful evaluation of my thesis and the productive suggestions.

- to all the genuine and sincere friends and people that I have met during these years

at ISTerre and in Grenoble, for your devotion, illumination, and enlightenment to my life.

Finally, I want to thank my family for who give me the total liberty to do what I want to do and back me up, and thank Yang for who is a perfect work and life partner. I also want to give the special thanks to my seven years old English cocker dog, Sam, whose name was inspired by the film “I am legend”. Thanks to him, I travel little and work more.

The completion of this thesis draws a temporary period for my three-year doctoral life and my balanced daily life in France which should be an essential time that profoundly affects my way of thinking.

Leonard Cohen said, “There is a crack in everything that’s how the light gets in.” That’s easily where the seismic waves velocities get changed.

Résumé

Le Japon s'est doté du réseau sismologique à haute sensibilité (Hi-net) qui contient plus de 1000 stations permanentes, qui fournissent d'immenses ensembles des données continues au Japon. Dans le cadre d'un accord avec le NIED, nous bénéficions d'enregistrements continus de données à court et d'inclinomtres pour analyser les variations de vitesse sismiques.

Nous appliquons ici la méthode de surveillance avancée basée sur le bruit (doublet + inversion, (Brenguier *et al.*, 2014)) pour suivre l'évolution mécanique de la croûte à différentes échelles de temps avec une résolution temporelle allant de mensuelle à quotidienne sur différentes périodes. L'objectif est d'obtenir la première surveillance à grande échelle au Japon et d'étudier l'impact des perturbations environnementales sur la propagation des ondes sismiques. Un autre objectif important de cette thèse est d'étudier l'évolution post-sismique liée au séisme de Tohoku-oki (M_w 9.0) en 2011. La vitesse des ondes sismiques change dans les semaines et les mois qui ont suivi le séisme. Cependant, l'origine physique de ces changements n'est pas claire. En utilisant à la fois les enregistrements Hi-net à courte période et à inclinomètre, nous obtenons des changements de vitesse sismiques dans toute la croûte jusqu'à 50 km en profondeur. Le résultat de courte période fournit une meilleure compréhension des processus souterrains sous les impacts de certains forçages environnementaux tels que l'hydrologie, la thermoélasticité et certains effets de charge directe. Le résultat de longues périodes montre des réponses co et post-sismiques différentes avec la profondeur. Il s'agit d'une méthode supplémentaire et directe pour révéler en profondeur le champ de contrainte/déformation, ce qui améliore la perception du mécanisme d'un tremblement de terre.

Cette thèse comprend principalement les trois parties suivantes.

La première partie est consacrée à la présentation de la relation entre la fonction de Green et les corrélations croisées. La simulation numérique à Hokkaido vérifie également

l'établissement de la relation entre les deux.

La seconde partie concerne l'analyse des variations transitoires de vitesse des ondes sismiques dans la croûte provoquées par les perturbations environnementales. Les impacts des perturbations saisonnières environnementales sur la déformation de la croûte sont mesurés et discutés en fonction des observations géodésiques. Récemment, la surveillance du bruit sismique ambiant a fourni de nouvelles informations sur la déformation continue de la croûte, révélée par les changements temporels de vitesse sismiques. Dans cette étude, nous identifions les différents facteurs environnementaux responsables des effets saisonniers locaux et montrons comment une meilleure compréhension de ces perturbations de la croûte causée par l'environnement améliore les observations des modifications des propriétés sismiques induites par la tectonique. La comparaison des effets saisonniers entre les changements de vitesse sismique et les observations géodésiques du champ de gravité mesuré par GRACE et du déplacement vertical du GPS montre une forte corrélation.

La dernière partie consiste à étudier la réponse mécanique de la croûte aux grands séismes. La surveillance de la vitesse sismique basée sur le bruit peut directement sonder en permanence l'état mécanique de la croûte en profondeur. Dans ce travail, nous étudions la réponse de la croûte terrestre au séisme de Tohoku-oki M_w 9.0, 2011. Nous employons ici pour la première fois le réseau très dense de tiltmètre Hi-Net en tant que sismomètres longue période (8 - 50 s) pour que la surveillance basée sur le bruit échantillonne la croûte à plus de 5 km en profondeur, qui est la limite pour les données des sismomètres courte période. L'évolution spatio-temporelle des changements de vitesse sismiques dans différentes bandes de périodes révèle une réponse sismique dépendant de la profondeur. Le résultat pourrait avoir des implications à la fois sur la réponse viscoélastique de la croûte aux grands déformations ou sur une réponse complexe des vitesses sismiques de la croûte à un écoulement de fluide transitoire.

Cette thèse s'inscrit dans le cadre d'une collaboration plus générale entre ISTerre – Université Grenoble Alpes et le Massachusetts Institute of Technology visant à développer des outils de surveillance dans des contextes naturels et industriels.

Abstract

The Japanese High Sensitivity Seismograph Network (Hi-net) contains more than 1000 permanent stations, which provide large continuous data sets throughout Japan. In the framework of an agreement with NIED, we benefit from both short period and tilt meters data downhole recordings to analyze the seismic velocity variations. We apply here the advanced noise-based monitoring method (doublet + inversion, (Brenguier *et al.*, 2014)) to follow the mechanical evolution of the crust at different time scales with a temporal resolution from monthly to daily in different period ranges. The objective is to get the first large scale monitoring throughout Japan and study how environmental perturbations affect seismic waves propagation. Another important objective of this thesis is to study the 2011 M_w 9.0, Tohoku-oki earthquake-related postseismic evolution. Seismic waves velocity changes in the weeks and months following the earthquake. However, the physical origin of these changes is not clear. By using both Hi-net short period and tilt meter recordings, we achieve seismic velocity changes in the whole crust down to 50 km at depth. The short-period result provides a better understanding of the subsurface processes under the impacts of some surrounding environmental forcings such as hydrology, thermoelasticity, and some direct loading effects. The result from long periods shows different co- and post-seismic responses with depth. It is an additional and direct method to reveal the stress/strain field at depth, which improves the perception of the mechanism of an earthquake.

This thesis mainly consists of the following three parts.

The first part is devoted to the theoretical demonstration of the relationship between the Green's function and cross-correlations. The numerical simulation in Hokkaido also verifies the establishment of the in-between connection.

The second part is about the analysis of the transient changes of seismic wave velocity in the crust caused by environmental perturbations. The impacts of environmental

seasonal disturbances to crustal deformation are studied and discussed based on geodetic observations. Recently, ambient seismic noise-based monitoring provides new insights into the continuous deformation in the crust as revealed by the temporal seismic velocity changes. In this study, we identify the different environmental factors in charge of the local seasonal effects and show how better understanding these environmentally induced crustal perturbations improves the observations of tectonic-induced seismic property changes. The comparison of seasonal effects between seismic velocity changes and geodetic observations from both GRACE measured gravity field and GPS vertical displacement show strong correlation.

The last part is the study of the mechanical response of the crust to large earthquakes. Noise-based seismic velocity monitoring can directly probe the mechanical state of the crust at depth continuously in time. In this work, we study the response of the crust to the M_w 9.0, 2011 Tohoku-oki earthquake. we employ here for the first time the very dense network of Hi-net tiltmeters as long period (8 – 50 s) seismometers for the noise-based monitoring to sample the crust below 5 km depth, which is the limitation for the data of short period seismometers. Spatio-temporal evolution of seismic velocity changes in different period bands reveals depth-dependent seismic response. The result could have implications of both nonelastic response of the crust to large strain changes or a complex response of crustal seismic velocities to transient fluid flow.

This thesis is in the context of a more general collaboration between ISTerre – Université Grenoble Alpes, and the Massachusetts Institute of Technology aiming at developing tools for monitoring in natural and industrial contexts.

Table des matières

1 Introduction **13**
1.1 Background of the Thesis 13
1.2 Outline 14

I Noise-based Imaging and Monitoring **17**

2 Principles of Ambient Seismic Noise Correlation **19**
2.1 Elastic Wave Equation 19
2.2 Green's function and Cross-correlation 21
2.2.1 In Scalar Wavefield 23
2.2.2 In Elastodynamics 26
2.3 Numerical Simulation 26
2.4 Discussion and Conclusion 28

3 Applications of Ambient Seismic Noise Correlations **31**
3.1 Ambient Seismic Noise 32
3.2 Surface Waves Tomography 33
3.3 Body Waves 36
3.4 Ambient Seismic Noise-based Monitoring 37
3.4.1 Origins of Seismic Velocity Changes in the Earth 37
3.4.2 Principles 38
3.4.3 Methods 41
3.4.4 Some Improvements 45
3.5 Other Applications 46

II Environmental Crustal Seismic Velocity Changes 49

4 Seasonal Crustal Seismic Velocity Changes throughout Japan 51

4.1 Abstract . . . 53
4.2 Introduction . . . 54
4.3 Data and Methods . . . 55
4.4 Analysis of Seasonal Variations in $\delta v/v$ . . . 58
4.4.1 Seasonality Strength . . . 58
4.4.2 Three-months Average Seismic Velocity Changes . . . 58
4.4.3 Sub-Areal Analysis . . . 60
4.4.3.1 Kyushu Velocity Change Anomaly . . . 61
4.4.3.2 Hokkaido Velocity Change Anomaly . . . 63
4.4.3.3 Western Hokkaido and Honshu . . . 65
4.5 Linear Model Correction . . . 69
4.6 Discussion and Conclusion . . . 73
4.7 Appendix . . . 74
4.7.1 A1 : Comparison with GRACE . . . 74
4.7.2 A2 : Time shift measurement . . . 75
4.8 Statistical Analysis of the Seismic Velocity Changes . . . 78

5 Comparison of Seasonal Velocity Changes with Geodetic Observations 81

5.1 Introduction of GPS Data . . . 82
5.2 Comparison between GPS Vertical Displacement and Seismic Velocity Changes . . . 83
5.2.1 Kyushu . . . 84
5.2.2 Japanese Alps . . . 85
5.2.3 Eastern Hokkaido . . . 86
5.2.4 Western Coastal Side of Hokkaido and Honshu . . . 87
5.3 Comparison with Observations by GRACE . . . 88
5.4 Discussion and Conclusion . . . 90

III Earthquake-related Co- and Post- seismic Processes from

Noise-based Monitoring **93**

6 Seismic response of the M_w 9.0, 2011 Tohoku-oki earthquake beneath Japan from noise-based seismic velocity monitoring **95**

6.1 Tiltmeter Data Introduction 96
6.2 Abstract 98
6.3 Introduction 99
6.4 Data and Methods 100
6.5 Spatial and Temporal evolution of seismic velocity changes 101
6.5.1 Spatial distribution of postseismic velocity changes 104
6.5.2 Temporal Variation of Seismic Velocity at Depth 107
6.5.2.1 Averaged Seismic Velocity Changes 107
6.5.2.2 Inversion of Seismic Velocity Changes 108
6.5.2.3 Inversion with Random Perturbation 112
6.6 Discussion 118
6.7 Conclusion 126

Conclusions et perspectives **127**

Bibliographie **132**

Chapitre 1

Introduction

Sommaire

1.1 Background of the Thesis 13

1.2 Outline 14

1.1 Background of the Thesis

In the past decade or so, ambient noise-based seismology has become an essential branch of seismology. The rationale behind noise-based seismology is that the cross-correlation of two continuously recorded noise signals can be regraded as the Green's function, which represents waves generated at one station and recorded at another station. The reconstructed cross-correlation functions carry information of the wave field where the waves pass through between the two correlated stations.

The reconstruction of Green's function depends on the equipartition condition of the different modes of the elastic wave field. An equal excitation of all types of waves can be achieved by a homogeneous distribution of sources or through multiple scattering. The cross-correlation can be used as earthquake or active sources generating seismic signals to image and monitor the underground medium. The emergence of noise cross-correlation has made up for many of the shortcomings of traditional seismology. For example, surface wave tomography relies no longer on the occurrence of earthquakes or generation of active sources. The construction of continuous seismic signals helps us successively track changes in seismic wave velocity, which may be related to some slow slip events, eruptions of volcanoes, or some earthquakes.

This thesis is a comprehensive application of the ambient seismic noise-based monitoring in the whole of Japan. The Japanese Islands are located in the eastern margin of the Asian continent and the northwestern margin of the Pacific Ocean. This is an active plate boundary zone where four lithospheric plates converge on one another (Ishibashi, 2004). Therefore, Japan has experienced considerable seismic and volcanic activities. Under the impact of the 1995 Kobe earthquake, Japan started to deploy the high-sensitivity seismograph network (Hi-net) (Okada *et al.*, 2004; Obara *et al.*, 2005) from 2000 till 2008. There are in total around 800 stations (Fig. 1.1(a)). All of them are installed at the bottom of a borehole more than 100 m at depth to record weak and fast activities. Fig. 1.1(b) illustrate the constitution of Hi-net stations in the borehole. The deepest borehole is Iwatsuki (IWTH) station located in Saitama city. Its depth is 3510 m. The dense distribution of Hi-net allows us to monitor $\delta v/v$ using more than 1000 downhole stations with both short period and tilt meter stations.

We apply the latest noise monitoring method by Brenguier *et al.* (2014) to continuously recorded seismic noise data. The big dataset allows us to follow the changes in physical properties of the crust throughout Japan. We except to first understand how the near surface could be affected by some transient perturbations. Then we will try to monitor the seismic velocity changes using tilt meter data for the first time and go to long period bands. The results at long period will help understanding deeper structural changes and possible depth-dependent changes.

1.2 Outline

This thesis consists of three main parts :

Part I shows an introduction of the principles and the development of ambient seismic noise correlation in seismology over the last decade years. The focus of this part is to present different methods of noise-based monitoring and compare their pros and cons.

Part II is about environmental seismology. How to use noise correlation to follow the subsurface seismic velocity changes and identify the annual signals in different regions throughout Japan. In this part, we also show some geodetic observations (GRACE measured equivalent water height, and GPS recorded vertical displacements) and their uniformity with seismic velocity changes.

Part III is a Tohoku-oki earthquake-related study. We first verify the feasibility of

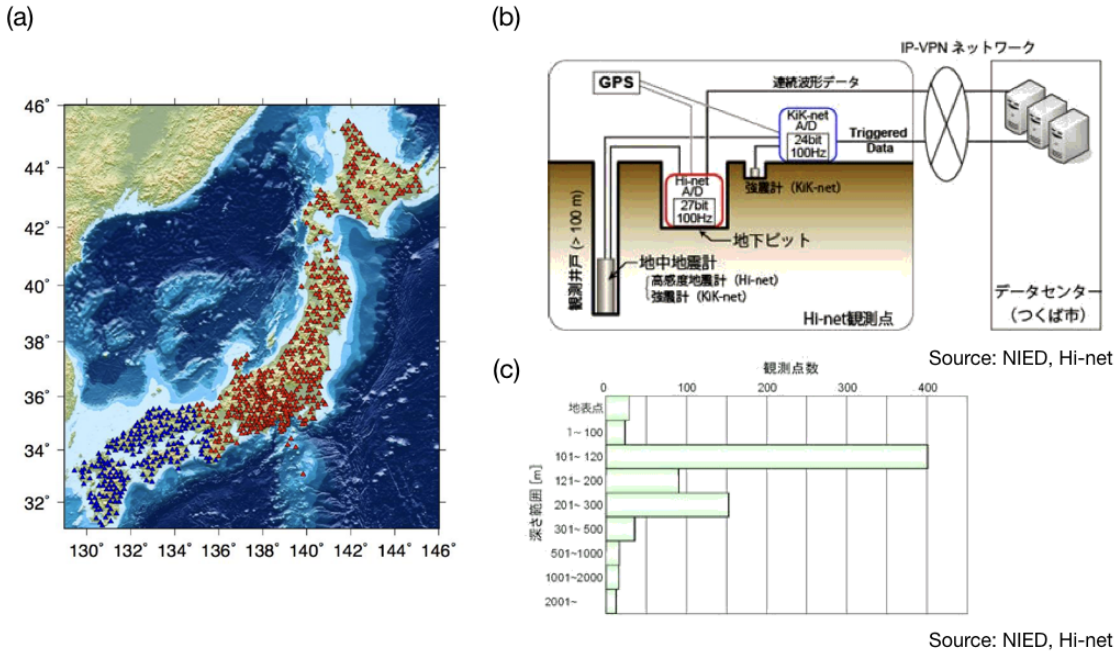

FIGURE 1.1 – (a) Hi-net station distribution. Blue triangles indicate data from 2008 to 2012. Red triangles indicate data from 2011 to 2012. (b) The constitution of Hi-net stations in downhole. (c) Depths distribution of number of Hi-net stations.

using tilt meter data to monitor the seismic velocity changes down to 50 km in the crust. We monitor the changes in different period ranges in 8 – 50 s. The depth-dependent co- and post- seismic velocity changes reveal a complex response of crustal seismic velocities to both static strain by the earthquake and transient deformation.

Première partie

Noise-based Imaging and Monitoring

Chapitre 2

Principles of Ambient Seismic Noise Correlation

Sommaire

2.1 Elastic Wave Equation 19

2.2 Green's function and Cross-correlation 21

2.2.1 In Scalar Wavefield 23

2.2.2 In Elastodynamics 26

2.3 Numerical Simulation 26

2.4 Discussion and Conclusion 28

We start this chapter from wave equations to the theoretical establishment of the relationship between Green's function and noise cross-correlation. We show a numerical simulation which verify the relationship deduced between the Green's function and cross-correlation. At the end we will discuss the limitations in practical applications.

2.1 Elastic Wave Equation

Firstly, wave equation is a second order partial differential equation that relates spatial derivatives of propagation of wave disturbances and second time in a simple wave. Considering a homogeneous medium, the equation of motion in terms of displacements and stress variables can be expressed as by eq.2.1.

$$\rho \frac{\partial^2 u_i}{\partial t^2} = f_i + \partial_j \tau_{ij}, \tag{2.1}$$

where ρ is density, u_i is displacement, τ_{ij} is stress tensor, and f_i is a body force term. Both of u_i and τ_{ij} are functions of position x and time t. According to the linear, isotropic relationship between stress and strain,

$$\tau_{ij} = \lambda \delta_{ij} e_{kk} + 2\mu e_{ij}, \tag{2.2}$$

where the strain tensor is,

$$e_{ij} = \frac{1}{2} \left(\partial_i u_j + \partial_j u_i \right), \tag{2.3}$$

thus, $e_{kk} = \partial_k u_k$. λ and μ are lamé parameters, we can substitute 2.3 into 2.2 and 2.1. Then we obtain :

$$\rho \frac{\partial^2 u_i}{\partial t^2} = f_i + \partial_i \lambda \partial_k u_k + \partial_j \mu \left(\partial_i u_j + \partial_j u_i \right) + \lambda \partial_i \partial_k u_k + \mu \partial_i \partial_j u_j + \mu \partial_j \partial_j u_i. \tag{2.4}$$

The equation 2.4 turns into following when using the vector Laplacian of the displacement field.

$$\rho \frac{\partial^2 \mathbf{u}}{\partial t^2} = \mathbf{f} + \nabla \lambda \left(\nabla \cdot \mathbf{u} \right) + \nabla \mu \cdot \left[\nabla u + \left(\nabla u \right)^T \right] + \left(\lambda + 2\mu \right) \nabla \nabla \cdot \mathbf{u} - \mu \nabla \times \nabla \times \mathbf{u}. \tag{2.5}$$

This is one form of motion equation in terms of displacements for an elastic isotropic medium (Aki et Richards, 2002). When ignoring the second and third terms of gravity and velocity gradient and assuming an homogeneous medium, the standard form of seismic wave equation becomes,

$$\rho \frac{\partial^2 \mathbf{u}}{\partial t^2} = \mathbf{f} + \left(\lambda + 2\mu \right) \nabla \left(\nabla \cdot \mathbf{u} \right) - \mu \nabla \times \nabla \times \mathbf{u}. \tag{2.6}$$

Without considering the force term $\mathbf{f}$, equation 2.6 can be regrouped in terms of Helmholtz potentials as,

$$\nabla\left[\left(\lambda+2\mu\right)\nabla^2\Phi(x,t)-\rho\frac{\partial^2\Phi\left(x,t\right)}{\partial t^2}\right]=-\nabla\times\left[\mu\nabla^2\mathbf{\Psi}(x,t)-\rho\frac{\partial^2\mathbf{\Psi}\left(x,t\right)}{\partial t^2}\right], \quad (2.7)$$

where $\Phi(x,t)$ is a scalar potential and $\mathbf{\Psi}(x,t)$ is the curl of a vector potential, both are functions of space and time (Stein et Wysession, 2003) (Chapter 2.4). The two solutions of 2.7 give the P- and S-wave velocity, which are $\alpha=\sqrt{\frac{\lambda+2\mu}{\rho}}$ and $\beta=\sqrt{\frac{\mu}{\rho}}$ respectively, and this is valid for a homogeneous medium.

The force term $\mathbf{f}$ can also be decomposed in Helmholtz potentials as : $\mathbf{f}=\nabla\Phi+\nabla\times\Psi$.

The general displacement $\mathbf{u}\left(x,t\right)$ due to a body force $\mathbf{F}\left(t\right)$ can be written as following and $\mathbf{u}\left(x,t\right)=\mathbf{F}\left(t\right)*G_{ij}$, where $*$ is a time convolution and G_{ij} represents the displacements recorded at one receiver when a body force $\mathbf{F}$ is applied as source. It is fundamental to investigate the medium wherein waves pass through.

$$\begin{aligned}\mathbf{u}\left(x,t\right)=&\frac{1}{4\pi\rho}\left(3\gamma_i\gamma_j-\delta_{ij}\right)\frac{1}{r^3}\int_{r/\alpha}^{r/\beta}\tau\mathbf{F}(t-\tau)d\tau\\&+\frac{1}{4\pi\rho\alpha^2}\gamma_i\gamma_j\frac{1}{r}\mathbf{F}\left(t-\frac{r}{\alpha}\right)\\&+\frac{1}{4\pi\rho\beta^2}\left(\gamma_i\gamma_j-\delta_{ij}\right)\frac{1}{r}\mathbf{F}\left(t-\frac{r}{\beta}\right),\end{aligned} \quad (2.8)$$

where $\gamma_i=x_i/r=\partial r/\partial x_i$ and r is the distance between source and receiver. The three terms on the right describe separately the displacements of the near field, the far-field P wave, and the far-field S wave. We can observe that the amplitude of different terms depend on the distance r. This is the elastodynamic Greens's function in an unbounded isotropic and homogeneous medium.

2.2 Green's function and Cross-correlation

Ambient seismic noise related techniques are based on the theory that waves recorded at two receivers are correlated to give the Green's function. It provides an alternative way to obtain seismograms which relies no longer on the occurrence of earthquakes or active

sources. The relationship between the Green's function and the cross-correlation equation has been discussed for decades, and the development process is mainly as follows.

Aki (1957) first gave the early hint to noise-correlation by offering an approach (SPAC) to estimate phase velocity of microtremors in order to reveal the nature of the medium. For 1D structure, Claerbout (1968) gave an important result that new seismic responses are produced by cross-correlating seismic recordings at different sites. The author shows that the reflection seismogram of a horizontally layered medium can be generated by the auto-correlation of its transmission response. The first application on the helioseismic tomography by Duvall *et al.* (1993) determines the travel time of waves along subsurface ray paths by cross-correlating the signals at two separated surface points. Later for acoustic thermal fluctuations, Weaver et Lobkis (2001) argued the possibility of extraction of information on waves propagation between two ultrasonic sensors when cross-correlating the recorded signals. This is true in the diffuse field created by a distant source or by thermal fluctuations in the specimen (Weaver et Lobkis, 2002). Campillo et Paul (2003) first showed the extraction of the ballistic wave Green's function from correlation of the seismic coda recorded at seismic stations in Mexico because of the diffusive characteristics of coda, which is the later arrivals in seismograms (Aki et Chouet, 1975). Weaver et Lobkis (2004) pointed out that one can retrieve the Green's function in open heterogeneous systems. The emerged Green's function is the full Green's function of the medium, symmetrized in time, with all reflections and scatterings and propagation modes. Also for scalar wave in a homogeneous elastic background, scatters can act as secondary sources, the high-frequency Green's function can be obtained by cross-correlating signals recordings with the stationary phase approximation (Snieder et Beukel, 2004). Roux *et al.* (2005) first theoretically demonstrated the correlation between the Green's function and the derivative of noise correlation functions in a 3D homogenenous medium with and without attenuation. Wapenaar et Fokkema (2006) showed that, for an arbitrary 3D inhomogeneous acoustic lossless medium, an integral over sources on an arbitrarily shaped surfaces of cross-correlations of wavefield serve as the Green's function between any two points in the shaped surface. For all these studies, the authors confirm the feasibility of reconstruction of the Green's functions from the ambient noise field. However, the underlying assumptions of physical constraints on the medium and the characteristics of wavefield are different. Yet the reconstruction of these Green's functions depends strongly on the spatio-temporal noise sources distribution. Either a fully diffusive medium or an even noise source distribution is required for the convergence of

the exact Green's function rebuilt from noise.

2.2.1 In Scalar Wavefield

In this section, we start from re-showing some mathematical derivation of the relationship between Green's function and cross-correlations equations in simple scalar wavefield. The analytical expression of spatial correlation of scalar waves in the frequency domain has been studied by Aki (1957); Duvall *et al.* (1993); Chávez-García et Luzón (2005) in 1- and 2-D. Nakahara (2006) demonstrates that in 1-, 2-, and 3-D random scalar fields, the normalized spatial correlation can be used to provide information about the propagation of waves between receivers.

In scalar wave field, the wave equation for waves propagating changes into

$$\frac{\partial^2 \mathbf{u}\left(x,t\right)}{\partial x^2} - \frac{1}{c^2}\frac{\partial^2 \mathbf{u}\left(x,t\right)}{\partial t^2} = \mathbf{P}, \tag{2.9}$$

where c is the speed of propagation of waveform. $\mathbf{P}$ is an impulsive source in both time and space and equal to $\delta\left(\mathbf{r}\right)\delta\left(t\right)$. The corresponding Green's function $G\left(\mathbf{r}_1,t;\mathbf{r}_2,t'\right)$ which satisfies the equation above is

$$\left(\nabla^2 - \frac{1}{c^2}\frac{\partial^2}{\partial t^2}\right) G\left(\mathbf{r}_1,t;\mathbf{r}_2,t'\right) = \delta\left(\mathbf{r}_1-\mathbf{r}_2\right)\delta\left(t-t'\right), \tag{2.10}$$

between receivers $\mathbf{r}_1$ and $\mathbf{r}_2$.

The 1D Green's function for 1D wave equation is deduced as :

$$G\left(\mathbf{r}_1,t;\mathbf{r}_2,t'\right) = \frac{c}{2}H\left(t-r/c\right), \tag{2.11}$$

where H denotes the Heaviside's unit step function and r is the distance between receivers $\mathbf{r}_1$ and $\mathbf{r}_2$.

The principle of noise correlation is that the cross-correlation of two signals at receivers $\mathbf{r}_1$ and $\mathbf{r}_2$ can be regarded as having a source at $\mathbf{r}_1$ producing waves that are recorded at $\mathbf{r}_2$ in the causal part (positive time) of the correlation function and from $\mathbf{r}_2$ to $\mathbf{r}_1$ in the anticausal part (negative time) when the noise sources distribution is homogeneous or the wave field is well diffusive. For any two signals $\mathbf{u}_1(t)$ at $\mathbf{r}_1$ and $\mathbf{u}_2(t)$ at $\mathbf{r}_2$ having interdistance equal to r, the normalized correlation of $\mathbf{u}_1(t)$ and $\mathbf{u}_2(t)$ is defined as,

$$\begin{aligned} C\left(\mathbf{r}_1, \mathbf{r}_2, t\right) &= \frac{1}{2\pi} \int_{-\infty}^{\infty} C_{1,2}\left(r, \omega\right) exp\left(-i\omega t\right) d\omega \\ &= \frac{1}{2}\left(\delta\left(t - \frac{r}{c}\right) + \delta\left(t + \frac{r}{c}\right)\right). \end{aligned} \tag{2.12}$$

The time derivative of Eq. 2.11 is

$$\frac{dG\left(\mathbf{r}_1, \mathbf{r}_2, , t\right)}{dt} = \frac{c}{2}\delta\left(t - \frac{r}{c}\right). \tag{2.13}$$

Substituting Eq. 2.13 into Eq. 2.12, we get

$$C\left(\mathbf{r}_1, \mathbf{r}_2, t\right) = \frac{1}{c}\left(\frac{dG\left(\mathbf{r}_1, \mathbf{r}_2, , t\right)}{dt} - \frac{dG\left(\mathbf{r}_1, \mathbf{r}_2, , -t\right)}{dt}\right). \tag{2.14}$$

This is the relationship between the Green's function and cross-correlation functions in 1D scalar wavefield. The former one can be retrieved from the integral of the normalized spatial correlations (Nakahara, 2006). Then for 3D, the Green's function with an impulsive point source can be deduced as

$$G\left(\mathbf{r}_1, t; \mathbf{r}_2, t'\right) = -\frac{1}{4\pi R}\delta\left(T - \frac{R}{c}\right), \tag{2.15}$$

where $T = t - t'$ and $R = |\mathbf{r}_1 - \mathbf{r}_2|$.

The relationship between the normalized cross-correlation functions and Green's function has been shown firstly by Roux *et al.* (2005) for scalar waves.

$$\begin{aligned} C\left(\mathbf{r}_1, \mathbf{r}_2, t\right) &= \frac{1}{2\pi} \int_{-\infty}^{\infty} C_{1,2}\left(r, \omega\right) exp\left(-i\omega t\right) d\omega \\ &= \frac{1}{4\pi} \int_{-\infty}^{\infty} \frac{\exp\left(i\omega\left(t - r/c\right)\right)}{i\omega r/c} d\omega - \frac{1}{4\pi} \int_{-\infty}^{\infty} \frac{\exp\left(i\omega\left(t + r/c\right)\right)}{i\omega r/c} d\omega. \end{aligned} \tag{2.16}$$

The time derivative of the cross-correction between signals at receivers $\mathbf{r}_1$ and $\mathbf{r}_2$ $C\left(\mathbf{r}_1, \mathbf{r}_2, t\right)$ is

$$\begin{aligned}\frac{d}{dt}C_{1,2} &= \frac{1}{4\pi r/c}\left(\delta\left(t-r/c\right)-\delta\left(t+r/c\right)\right)\\ &= c\left(G\left(\mathbf{r_1},\mathbf{r_2},t\right)-G\left(\mathbf{r_1},\mathbf{r_2},-t\right)\right).\end{aligned} \tag{2.17}$$

The right two terms correspond to the forward and backward Green's function between $\mathbf{r}_1$ and $\mathbf{r}_2$. The time derivative of cross-correlation is proportional to the Green's function, which means there is a $\pi/2$ phase shift between them. This does not affect the noise-based monitoring using directly the cross-correlation functions, as all the time shifts are measured relatively. However it has an influence on the travel-time based-tomography. This phase difference should be corrected when the exact arrival time is needed. Both relationships that we reproduce above are valid under the assumptions that noise sources are spatially homogeneous and the medium is acoustic lossless infinite.

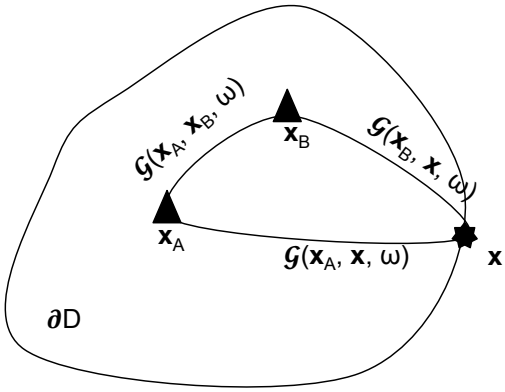

FIGURE 2.1 – Sketch of a bounded area with locations of two receivers $\mathbf{x}_A$ and $\mathbf{x}_B$ and a source coordinate $\mathbf{x}$ at ∂D.

When goes into a 3D bounded medium Wapenaar et Fokkema (2006) first deduced the relationship between the imaginary part of Green's function and the integral of the Fourier transform of cross-correlation of observations of wave field at two locations $\mathbf{x}_A$ and $\mathbf{x}_B$, which are inside of the boundary. $\mathcal{G}$ denotes the Fourier transform of G. This relationship in the frequency domain is deduced based on the acoustic source-receiver reciprocity theorem and shown as

$$\begin{aligned}2jIm\left(\mathcal{G}\left(\mathbf{x}_A,\mathbf{x}_B,\omega\right)\right) = \int_{\partial D}\frac{1}{P\left(\mathbf{x}\right)}&(\mathcal{G}^*\left(\mathbf{x}_A,\mathbf{x},\omega\right)\partial_i\mathcal{G}\left(\mathbf{x}_B,\mathbf{x},\omega\right)\\ &-\partial_i\mathcal{G}^*\left(\mathbf{x}_A,\mathbf{x},\omega\right)\mathcal{G}\left(\mathbf{x}_B,\mathbf{x},\omega\right))n_i d^2\mathbf{x}.\end{aligned} \tag{2.18}$$

The left part denotes the imaginary part of the Green's function between $\mathbf{x}_A$ and $\mathbf{x}_B$. P indicates the acoustic pressure. $*$ is the complex conjugation. The integral for the right term is arbitrary and along the source coordination $\mathbf{x}$.

2.2.2 In Elastodynamics

In elastodynamics, the extraction of Green's function has been experimentally proved by cross-correlation in diffuse elastic wavefield generated by multiple scatterings (Campillo et Paul, 2003) or by random distribution of noise sources (Shapiro et Campillo, 2004) for the surface-wave part in seismology. Sanchez-Sesma et Campillo (2006) first theoretically demonstrated that the 2D Green's function can be retrieved from cross-correlation under the condition that the incident waves are isotropic plane waves. They show the proportional relationship between the Fourier transform of averaged cross-correlation of and the imaginary part of the Green's function as following under the assumption that $E_s/E_p = \alpha^2/\beta^2$.

$$\langle \mathbf{u}_i(\mathbf{r}_1;\omega)\, \mathbf{u}_j^*(\mathbf{r}_2;\omega)\rangle = -8E_s k^{-2} Im\left(G_{ij}(\mathbf{r}_1,\mathbf{r}_2;\omega)\right), \tag{2.19}$$

where $E_s = \rho\omega^2 S^2/2$, k is S wavenumber and equal to ω/β. β is S wave speed. $\mathbf{r}_1, \mathbf{r}_2$ are locations of two receivers.

For 3D, the relationship between the Fourier transform of averaged cross-correlation of and the imaginary part of the Green's function is shown as :

$$\langle \mathbf{u}_i(\mathbf{r}_1;\omega)\, \mathbf{u}_j^*(\mathbf{r}_2;\omega)\rangle = -2\pi E_s k^{-3} Im\left(G_{ij}(\mathbf{r}_1,\mathbf{r}_2;\omega)\right), \tag{2.20}$$

where $E_s = \rho\omega^2 S^2$ in 3D, and k is S wavenumber and equal to ω/β.

2.3 Numerical Simulation

To confirm the theoretical relationship between cross-correlation and Green's function, we simulate the elastic wave propagation in 3-D heterogeneous media without attenuation using the velocity model by Matsubara *et al.* (2017) in Japan using the SEM code developped by Trinh *et al.* (2017). The region is defined in Hokkaido as a square

with length of 400 km. Two receivers r_1 and r_2 are centered in this square. The interdistance of two receivers is 60 km. The source frequency is 0.2 Hz. Fig. 2.2 shows the sketch of the array setting.

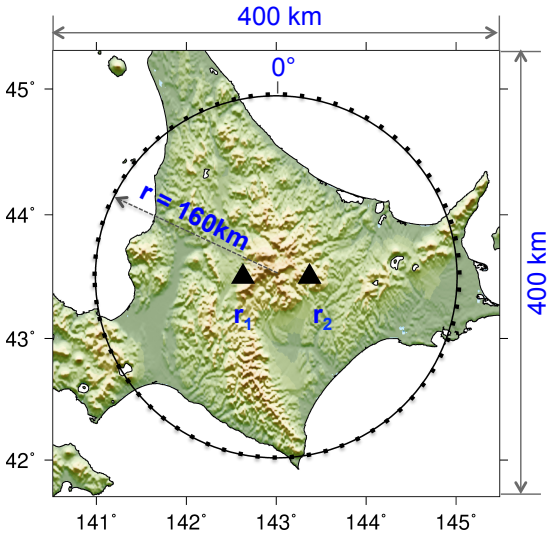

FIGURE 2.2 – Sketch map of the array set. Two black triangles indicate the two receivers r_1 and r_2. The black circle indicates locations of sources with a radius of 160 km.

Considering that noise sources come isotropically from all possible azimuths from 0° to 360°. We calculate the cross-correlations of all the recorded signals at the two receivers. The cross-correlations are plotted against the clockwise azimuths (Fig. 2.3). We observe clearly the direct arrivals and the later coda waves.

The stack of all cross-correlations in Fig. 2.4 (blue dashed curve) is supposed to be symmetric and resemble the Green's function with a phase shift of $\pi/2$. The derivative of stacked cross-correlations fits well into the Green's function between r_1 and r_2 except the amplitude which are slightly different. This similarity verifies the interrelationship between the cross-correlation equation and the Green's function that, in time domain : $\frac{\partial}{\partial t}C(t) \propto G_{r_1,r_2}(t) - G_{r_2,r_1}(-t)$, the derivative of cross-correlation equation yields an exact representation of the Green's function with an amplitude factor.

Yao et van der Hilst (2009) discuss in detail the phase relationship between cross-correlations and Green's function. We zoom in one part of the later arrival from 40 s to 60 s and we observe that even the coda part of the derivative of stacked cross-correlations are in phase with the Green's function. And the cross-correlations still differ from the green's function with a $\pi/2$ phase shift. This simulation confirms the availability of the

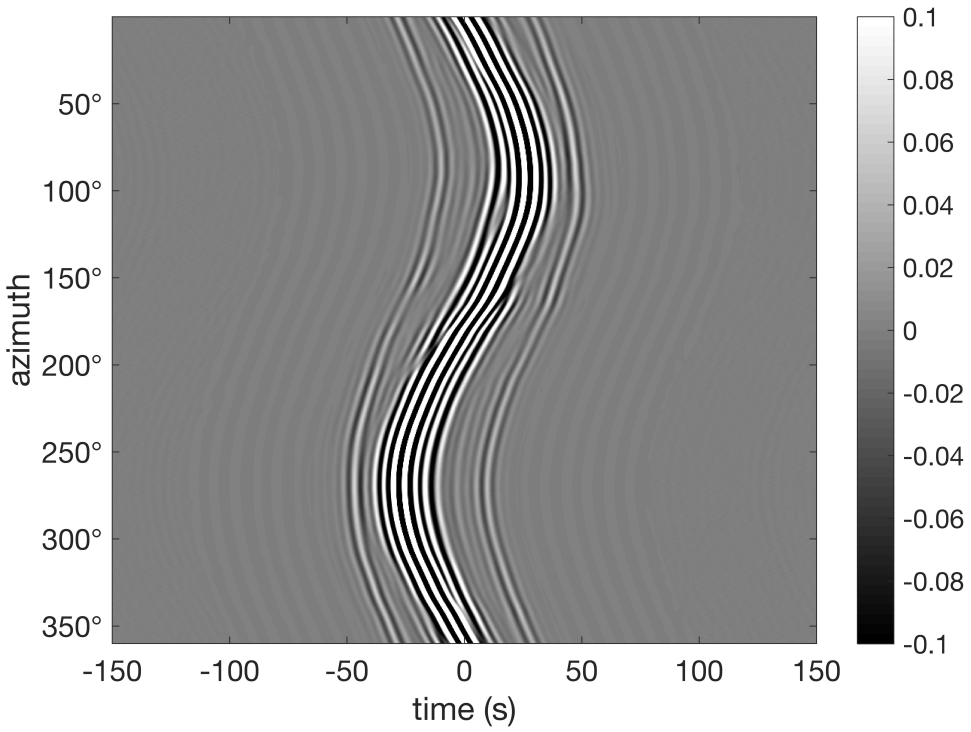

FIGURE 2.3 – Normalized cross-correlations of signals recorded at receivers r_1 and r_2 from 0° to 360°.

later portion of the cross-correlation. And realistically, we can use directly the cross-correlations for the propose of monitoring. As we measure the relative time changes within different pairs of cross-correlations.

2.4 Discussion and Conclusion

The validation of the equivalence between the Green's function and correlation functions have been proved under different assumptions. In practice, the distribution of noise sources are out of control and non-isotropic, which is unfavorable for reconstructing a symmetric Green's function (Paul *et al.*, 2005). The travel time measurements based on the direct arrival waves are strongly affected by the non-isotropic distribution of noise sources. However the presence of scatterings can compensates this influence to some extent. The theoretical bias in travel time measurements on direct arrival waves has first been discussed by Weaver *et al.* (2009) on considering a fully asymptotic limit for the far-field sources in homogeneous medium. Later Froment *et al.* (2010) show the bias of

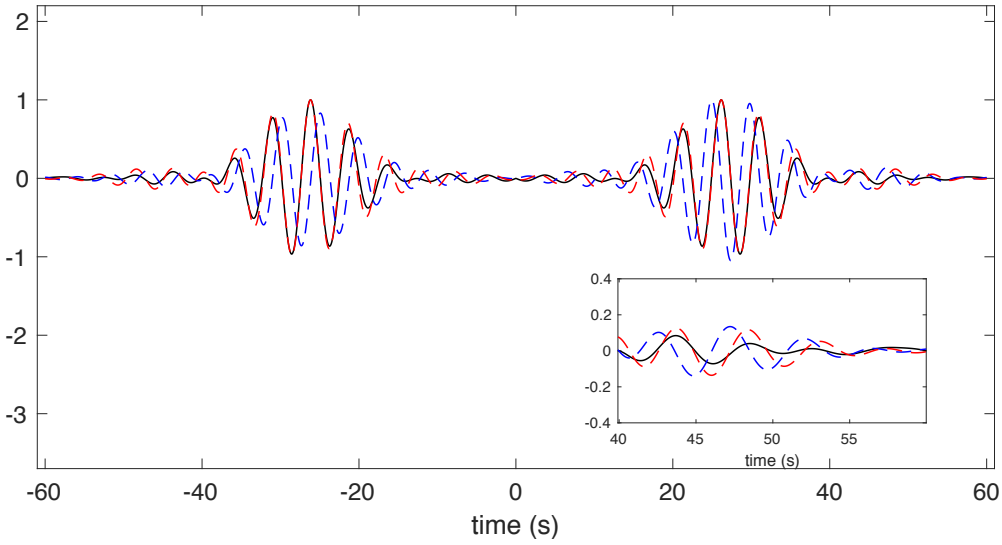

FIGURE 2.4 – The blue dashed curve indicates the stack of cross-correlations with all possible azimuths. The black curve is the green's function between r_1 and r_2. The red curve is the derivative of stacked cross-correlations. Zoom in from 40 s to 60 s is shown down in the lower right.

travel time from different levels of uneven noise distribution. They also show that when using the coda waves of cross-correlations, the bias almost disappears. This is the benefit of using coda waves for monitoring. Colombi *et al.* (2014) evaluate the temporal stability of the coda of cross-correlations. This provides us the opportunity to assess theoretical errors when using the coda waves part for monitoring. We estimate the theoretical error using the method introduced by Colombi *et al.* (2014) for our case with parameters : frequency f = 0.3 Hz, the mean free path l = 100 km, and velocity c = 3 km/s at lapse time t = 60 s. We get the theoretical fractional error is $1.5 \cdot 10^{-4}$ when noise sources are extremely in-isotropic ($B_2 = -0.6$). Furthermore, the coda waves of cross-correlation is less subject to non-homogeneous origins of noise sources. Therefore, the expected error for our monitoring should be smaller than $1.5 \cdot 10^{-4}$.

So when dealing with actual problems, we need to take different methods to enhance the stability of reconstruction of Green's functions. For example, the preprocessing of noise data before cross-correlation (Bensen *et al.*, 2007), stack of cross-correlation equations, filtering (Stehly *et al.*, 2011; Moreau *et al.*, 2017), cross-correlation of cross-correlation ($C3$) (Stehly *et al.*, 2008) or quality control and selection based on signal-to-noise ratio. This will be further discussed in the application of ambient seismic noise

Chapter.

Chapitre 3

Applications of Ambient Seismic Noise Correlations

Sommaire

3.1 Ambient Seismic Noise 32

3.2 Surface Waves Tomography 33

3.3 Body Waves 36

3.4 Ambient Seismic Noise-based Monitoring 37

3.4.1 Origins of Seismic Velocity Changes in the Earth 37

3.4.2 Principles 38

3.4.3 Methods 41

3.4.4 Some Improvements 45

3.5 Other Applications 46

This chapter mainly introduces the applications of ambient seismic noise correlation methods in seismology over the last decade, such as surface wave tomography, body wave extraction, and monitoring. We introduce briefly different aspects of these applications and focus on noise-based monitoring. The emphasis is given on the comparison between different methods and the presentation of cutting-edge aspects on what improvements have been made.

3.1 Ambient Seismic Noise

Ambient seismic noise is a persistent vibration of the ground that is recorded by seismometers. The origin of noise is diverse and distinct for lower and higher frequencies (Gutenberg, 1958; Donn, 1966; Bonnefoy-Claudet *et al.*, 2006). For higher frequency ($f > 1Hz$), noise comes mostly from human activities with daily and weekly variations. Whereas for lower frequency ($f < 1Hz$), noise is mainly due to natural causes like the interaction of the oceanic swell with the solid Earth and atmospheric turbulence in storm areas, and standing waves in the ocean resulting from the interference of oppositely moving wave trains of the same period. Notably, in the frequency band 0.3 – 0.05 Hz, the ambient noise is often referred to as microseisms, which is not produced by earthquakes or explosions. Microseisms may occur when atmospheric disturbances generated energy is converted into energy of ocean waves that then transmit a portion of this energy either to the ocean bottom or to coast. Then elastic waves travel through the crust and can be recorded. Physically, ambient seismic noise consists primarily of the fundamental mode of surface waves, with dominating Rayleigh waves(Toksoz et Lacoss, 1968).

The spectra of microseisms contain two prominent energy peaks are around 14 s and 7 s of period, which are called primary and secondary microseismic peaks respectively. The primary peak resembles the spectrum of ocean gravity waves. The expected sources areas for these are in the shallow water as the limitation of penetration of gravity waves at this period (Haubrich *et al.*, 1963; Friedrich *et al.*, 1998). However, Stehly *et al.* (2006) also show that the primary microseism could be generated in oceanic deep basins. The interaction between the gravity waves and ocean floor can produce both Rayleigh and Love waves. And the latter one requires horizontal forces that come from the interaction between propagating ocean waves and sea-bottom topography (Saito, 2010). While for the secondary microseism, Longuet-Higgins (1950) suggests that it originates from surface pressure oscillations caused by the interaction between oppositely travelling components with the same frequency in the ocean wave spectrum. Such interactions can be acquired from both coastal and deep water (Hillers *et al.*, 2012).

For very long period $> 30s$, continuous oscillations of Earth surface which are often referred to as "hum" have also been observed. The excitation of hum is confirmed to be the interaction between atmosphere, ocean and seafloor, probably through the conversion of storm energy to oceanic infragravity waves that interact with seafloor topography by Rhie et Romanowicz (2004) using an array-based method. Based on the array analysis of

tiltmeter recordings in the Japanese islands, Nishida *et al.* (2008a) find clear evidence of background Love and Rayleigh waves. They suggest the most likely excitation mechanism is shear traction acting on a sea-bottom horizon as a result of the linear topographic coupling of infragravity waves.

The location of noise sources varies in time and space Stehly *et al.* (2006). The dominant sources distribution is anisotropic in azimuth, which leads to a non-accurate reconstruction of Green's function. The connection between the Green's function and noise correlations is underlying the theory that noise sources come from all directions. This can be solved by using well scattered coda waves or by stacking the multi-directional cross-correlations. We will introduce this later in detail in the applications of noise correlations part.

3.2 Surface Waves Tomography

Ambient seismic noise consists primarily of the fundamental mode of surface waves (Toksoz et Lacoss, 1968). Surface waves propagation between two sensors can be well retrieved from the correlation of ambient seismic noise (Shapiro et Campillo, 2004) or from the correlation of coda waves (Campillo et Paul, 2003). The first attempt of ambient seismic noise-based surface waves group-speed tomography is made by Shapiro *et al.* (2005) to image the upper crust of California. This improves the local resolution of crustal structure. Then ambient noise surface waves tomography has been widely applied from small scale ex : volcanic system (Brenguier *et al.*, 2007) ; regional scale ex : Yao *et al.* (2008); Stehly *et al.* (2009) ; continental scale ex : Yang *et al.* (2007); Bensen *et al.* (2007) to global scale ex : Nishida *et al.* (2009); Haned *et al.* (2016) to investigate the underground structure from shallow to the upper mantle.

Traditional ambient noise tomography employs a two-step inversion approach based on ray-theory. 2-D velocity maps are estimated using surface wave group or phase velocity measurements, followed by 1-D depth inversion of local dispersion curves to obtain shear-wave velocity models, which together form a pseudo 3-D velocity model. Most previous studies for improving ambient noise tomography are in the same 2-step workframe, including retrieval of Green's functions (Stehly *et al.*, 2008; Moreau *et al.*, 2017) ; 2-D Helmholtz tomography (Lin *et al.*, 2009; Lin et Ritzwoller, 2011) ; 2-D non-linear velocity map inversion (Bodin *et al.*, 2012a; Young *et al.*, 2013) and 1-D non-linear depth inversion (Bodin *et al.*, 2012b; Shen *et al.*, 2012; Lu *et al.*, 2018). Fang *et al.* (2015) directly

invert for 3-D model without constructing intermediate group or phase velocity maps, so that the resulting 3-D model is constrained as a whole.

Recent advances in computational resources and numerical techniques allow new ambient noise inversion approaches based on solving the wave-equation, referred to as 'ambient noise wave-equation tomography'. The new approach takes advantages of accurate 3-D numerical simulation of wave-field and misfit kernels. It overcomes main drawbacks of traditional ambient noise tomography by taking into account 3-D and finite-frequency effects. Current applications of ambient noise wave-equation tomography (Gao et Shen, 2014; Chen *et al.*, 2014) make use of the traveltime information. Efforts are also made towards ambient noise full waveform inversion considering amplitude information (Fichtner, 2014, 2015). However, since the amplitude are influenced by the anisotropic distribution of ambient noise source and preprocessing procedure, the ambient noise full waveform inversion is still under development and need to be improved.

In Japan, Nishida *et al.* (2008b) first use tiltmeter recordings to reconstruct the Green's functions for imaging entire Japan. The authors take advantage of dense array of Hi-net tiltmeters and obtain 3-D S wave velocity structure (Fig. 3.1) ($0.1^\circ \times 0.1^\circ \times 1$ km grid) from the surface to a depth of 50 km.

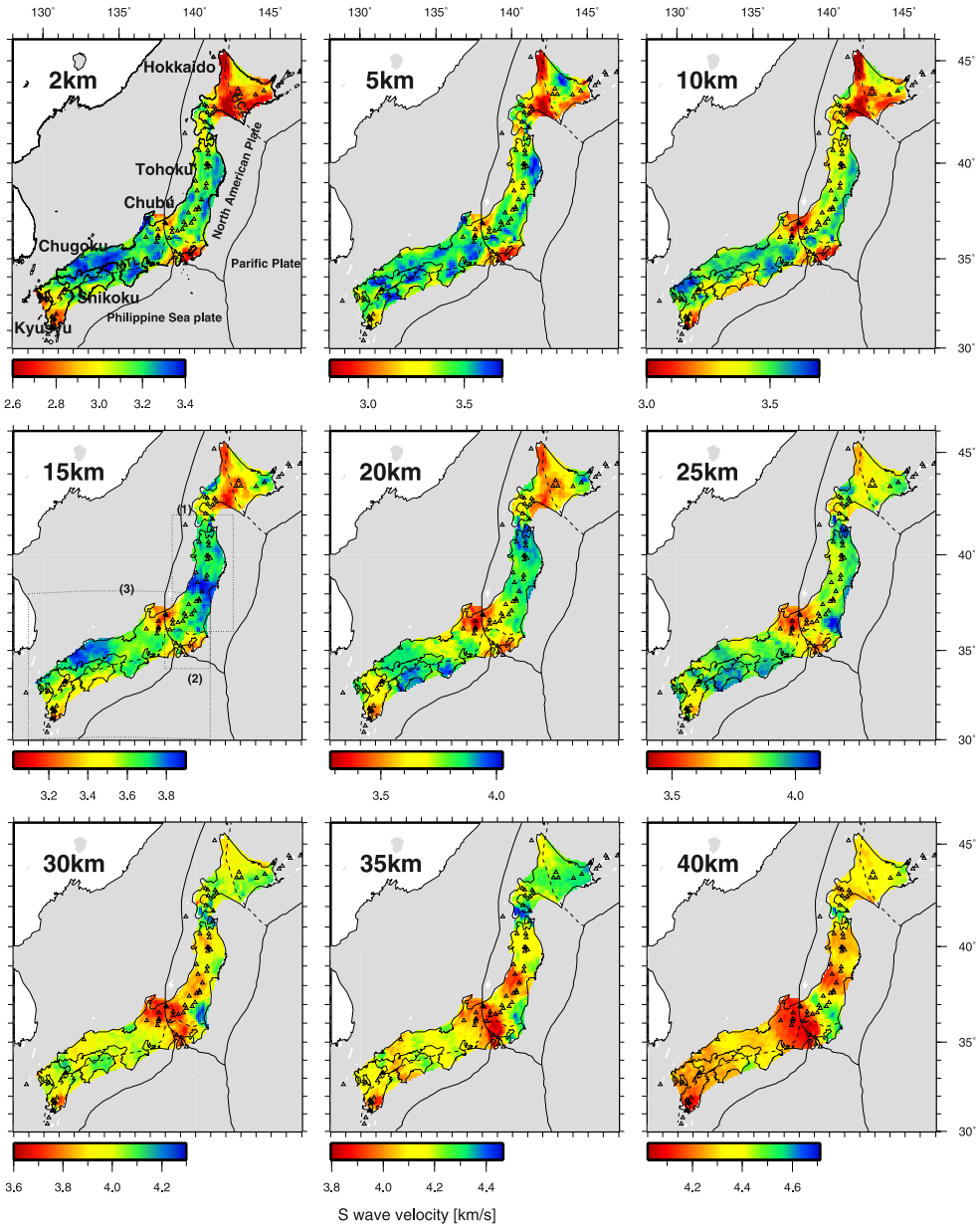

FIGURE 3.1 – Depth slices of a resultant S wave velocity structure in Japan after Nishida *et al.* (2008b).

3.3 Body Waves

Despite surface waves predominate the reconstructed Green's function, extraction of body waves has been verified first by Roux *et al.* (2005) from the cross-correlation of noise recordings in the Parkfield network, California (Fig. 3.2). Later, Draganov *et al.* (2007) show the results on the retrieval of reflections arrivals in regional seismology. Both Moho-reflected body wave (SmS) and its multiples have been identified by Zhan *et al.* (2010). They also report that relatively weak body waves can be masked by uneven distribution of noise sources by the surface waves' precursors. Poli *et al.* (2012a,b) also show the emergence of body waves at high-frequency (0.5–2 Hz) on the northern part of the fennoscandian region and Moho-reflected body waves from the 410 km and 660 km discontinuities at depth from noise correlations. This provides the possibility of imaging of the mantle transition zone with ambient seismic noise using body waves. Global propagagtion of body waves have been retrieved by Nishida (2013) using seismic hum with frequency-wave number filtering in the range of 5 to 40 mHz. Boué *et al.* (2013); Nakata *et al.* (2015) extract body waves to probe separately the deepest part of the Earth at global scale and regional scale in California.

The Fig. 3.2 represent the first observation of P waves from ambient seismic noise correlation by Roux *et al.* (2005) using noise recording on the dense temporary seismic network installed in the Parkfield area.

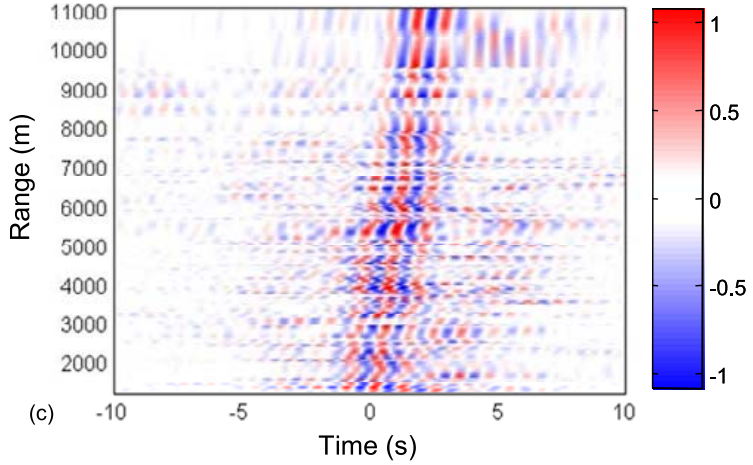

FIGURE 3.2 – Range-time representation of the Z-Z compo- nent of the noise correlation tensor averaged over one month in three frequency bands [0.7 – 1.3 Hz]. The plot has been normalized by its own maximum after Roux *et al.* (2005).

3.4 Ambient Seismic Noise-based Monitoring

In this section, we focus on noise-based monitoring and discuss the motivation behind monitoring, the principles, and some conventional methods. In the end, we introduce some comparisons and improvements made in our actual work in Japan.

3.4.1 Origins of Seismic Velocity Changes in the Earth

Changes in the subsurface stress field is an important indicator for studying nucleation and triggering of earthquakes, as well as the activity of natural and humanmade reservoirs (Silver *et al.*, 2007a). However the estimation of the stress state mainly relies on either downhole strainmeters or some geodetic observations. The former one is geographically and temporarily restricted, and the latter one lacks direct information at depth. Usually, the changes of the physical properties of the rocks in the crust are accompanied by changes of seismic wave velocity. Numerous studies have proven the dependence of seismic velocity in the crust on stress, some theoretical analysis (O'Connell et Budiansky, 1974; Schoenberg, 1980), through some early experimental proofs (Birch, 1961; Nur et Simmons, 1969; Nur, 1971), and field works (Reasenberg et Aki, 1974; Yamamura *et al.*, 2003; Silver *et al.*, 2007b). Therefore, monitoring of seismic velocity changes can be used as an effective tool to probe changes of the subsurface stress field.

The continuous noise recordings provide us with a unique chance to reconstruct the continuous Green's functions between any couple of seismic stations (Campillo et Paul, 2003; Shapiro et Campillo, 2004; Campillo, 2006). The possibility to reconstruct these Green's functions repetitively in time, e.g. at different calendar days, leads to continuously monitoring the seismic velocity changes, and thus changes in the physical properties of the crust. The origins of seismic wave velocity changes are diverse and usually can be linked to some environmental factors induced transient stress changes, which includes rainfall-induced pore pressure change (Sens-Schönfelder et Wegler, 2006; Meier *et al.*, 2010; Tsai, 2011; Wang *et al.*, 2017; Johnson *et al.*, 2017), temperature induced thermoelastic effect (Ben-Zion et Leary, 1986; Meier *et al.*, 2010; Tsai, 2011; Richter *et al.*, 2014; Hillers *et al.*, 2015a), and tidal effects (Yamamura *et al.*, 2003; Hillers *et al.*, 2015b). There are also some environmental loading effects such as atmospheric pressure (Johnson *et al.*, 2017), snow (Wang *et al.*, 2017), groundwater (Johnson *et al.*, 2017) and sea surface height (Wang *et al.*, 2017) etc., which act by opening or closing the micro-

cracks in the medium. In addition to those environmental factors, there is also dynamic stress changes, such as the occurrence of an earthquake, which can produce a sudden quick drop of seismic velocity (Brenguier *et al.*, 2008a, 2014; Taira *et al.*, 2015; Wang *et al.*, 2017). This phenomenon has been experimentally and systematically studied by Lyakhovsky *et al.* (1997); Johnson et Sutin (2005) and is often referred to as nonlinear elastic behavior including both anomalous nonlinear fast dynamics (ANFD) and slow dynamics (SD). And Lyakhovsky *et al.* (2009) develop a nonlinear continuum damage model and successfully explain various deformational aspects of damaged materials with theoretical analyses and numerical simulations.

In this thesis, we will show a comprehensive study in Japan on seismic velocity changes, which are related to environmental factors induced transient stress changes and the 2011 Tohoku-oki earthquake generating both significant dynamic and static stress changes.

3.4.2 Principles

Fig. 3.3 (a) and (b) illustrate the continuous noise recordings at site A and B and the reconstructed Green's function between them from A to B in the positive causal part and from B to A in the negative anticausal part. When the local medium encounters changes, the seismic velocity change and thus the travel times too. Normally we measure the changes of seismic velocity using surface and coda waves. The basis of the monitoring using coda waves is that the medium undergoes a homogeneous change, the δt accumulates linearly with the lapse time. The relative $\delta v/v$ is equal to -$\delta t/t$ in case of a homogeneous perturbation. Coda waves are the multiple scattered waves, the tail part on the cross-correlation functions Fig. 3.3 (d). They sample the medium with a much longer path than the direct arrival waves Fig. 3.3 (c). Hence, the later coda wave arrivals are sensitive to very small velocity changes in the medium. Fig. 3.5 illustrates how the later coda waves are more sensitive to velocity changes than the direct arrivals. We artificially stretch the black wave form by a decrease of velocity of 0.01 $\delta v/v$ in Fig. 3.5 (a). The red curve clearly shows that the later part of time lag has a bigger phase shift. Fig. 3.5 (b) show real noise cross-correlations after the 2011 Tohoku-Oki earthquake. We can also see that the phase shift becomes more evident with increasing lapse time. Ambient seismic noise based monitoring has also proved to be valid even in the case where the

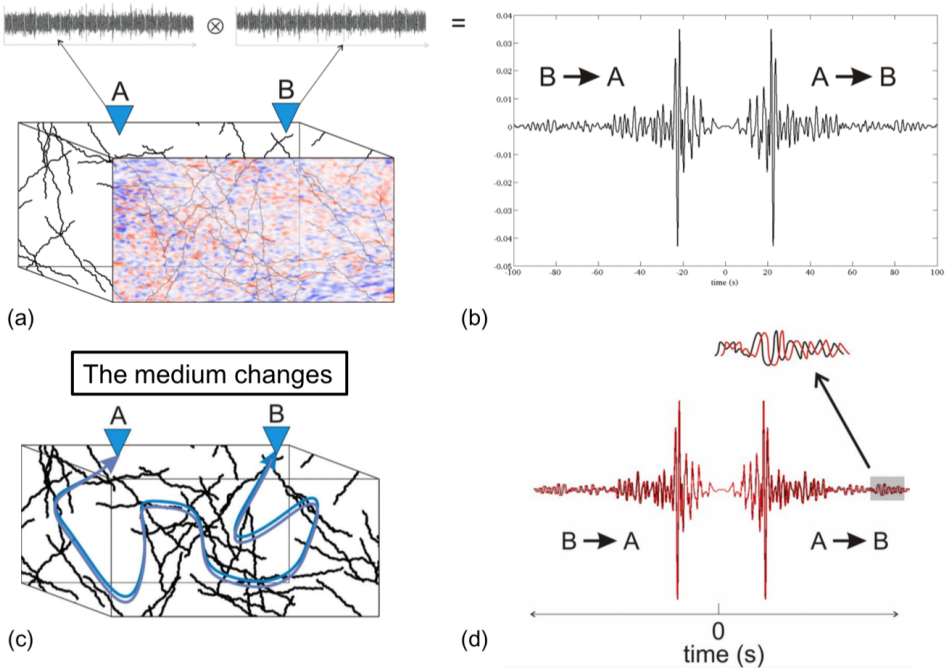

FIGURE 3.3 – (a) Noise recordings at stations A and B. (b) The cross-correlation function between A and B. (c) Stochastic medium changes of the wave path between A and B. (d) Two cross-correlation equations with a slight time shit. Schema from presentation by Brenguier 2017.

Green's functions are not well reconstructed (Hadziioannou *et al.*, 2009; Weaver *et al.*, 2009). Here we present daily cross-correlation functions from vertical components of Hi-net stations FSWH and TOWH in Japan in the frequency range 0.1 - 1 Hz from 2008 to 2012 3.4. The average cross-correlation (red curve) shows good symmetric waveforms. On the days of the occurrence of earthquakes, there is no distortion observed. We can still see very stable and clear scattered waves even until late tag times of 60 s.

Noise-based monitoring has provided insights into tectonic and volcanic processes, to allow the detection of long-term post-seismic relaxation in fault zones (Brenguier *et al.*, 2008a; Hobiger *et al.*, 2012; Froment *et al.*, 2013). Fig. 3.6 show the classic example of earthquakes related seismic velocity changes in the San Andreas fault zone (Brenguier *et al.*, 2008a). The result indicates that there is an immediate decrease in the seismic velocity coincident with earthquakes that is followed by a slow relaxation. Authors point out that the seismic velocity changes are related to both co-seismic damages in the shallow layers and to deep co-seismic stress changes and postseismic stress relaxation within the fault zone. Monitoring also offers insights into velocity decreases as precursors of volcanic

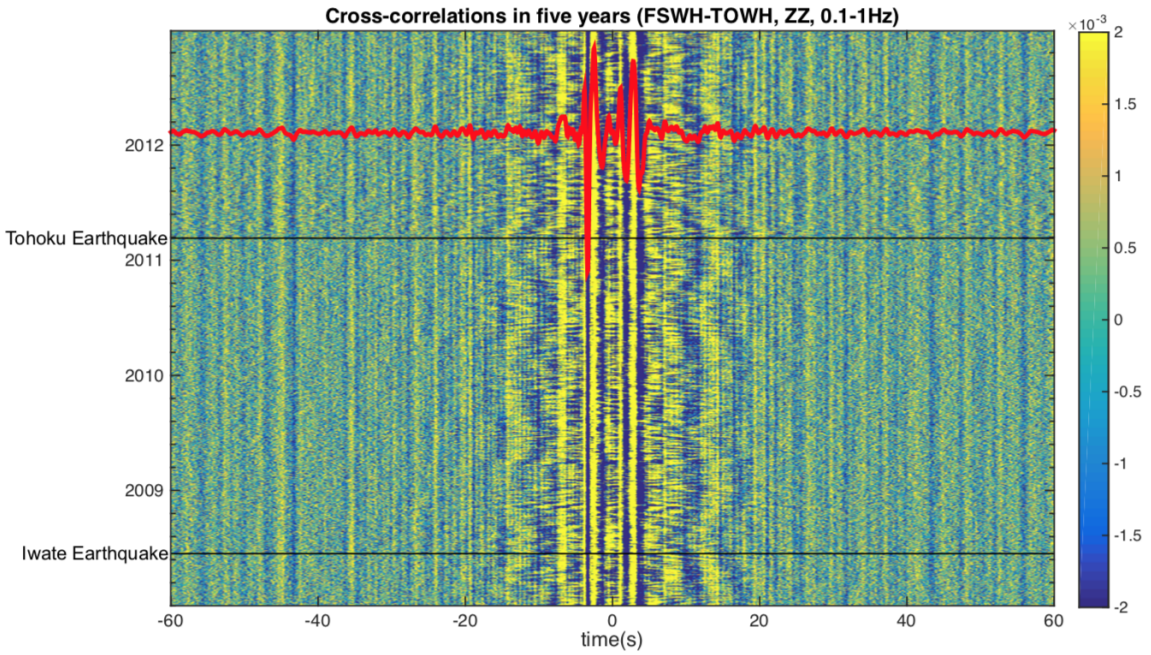

FIGURE 3.4 – Daily cross-correlation between two Hi-net stations FWSH and TOWH from 2008 to 2012. The red curve represent the mean cross-correlation functions. The two horizontal black lines indicate the day of two earthquakes.

eruptions (Wegler et Sens-Schönfelder, 2007; Brenguier *et al.*, 2008b, 2011; Obermann *et al.*, 2013), and interactions between seismic and volcanic systems (Brenguier *et al.*, 2014; Taira et Brenguier, 2016). Also seismic velocities can be affected by external environmental perturbations, such as rainfall (Sens-Schönfelder et Wegler, 2006; Meier *et al.*, 2010; Tsai, 2011; Hillers *et al.*, 2014), thermoelastic stress (Meier *et al.*, 2010; Hillers *et al.*, 2015a), and atmospheric pressure (Silver *et al.*, 2007a). Both environmental perturbations and earthquakes related seismic velocity changes will be introduced in detail for cases in Japan in the second and third parts of the thesis.

The noise-based monitoring probe very high accuracy of seismic velocity changes down to 10^{-5}. Time resolution can be as accurate as hourly or daily to detect velocity changes of different origins. However, the spatial resolution is relatively low as the travel path of coda waves cannot be accurately obtained. Regarding these problems, some improvements have been made in recent studies. We will mention this in the last section of this chapter.

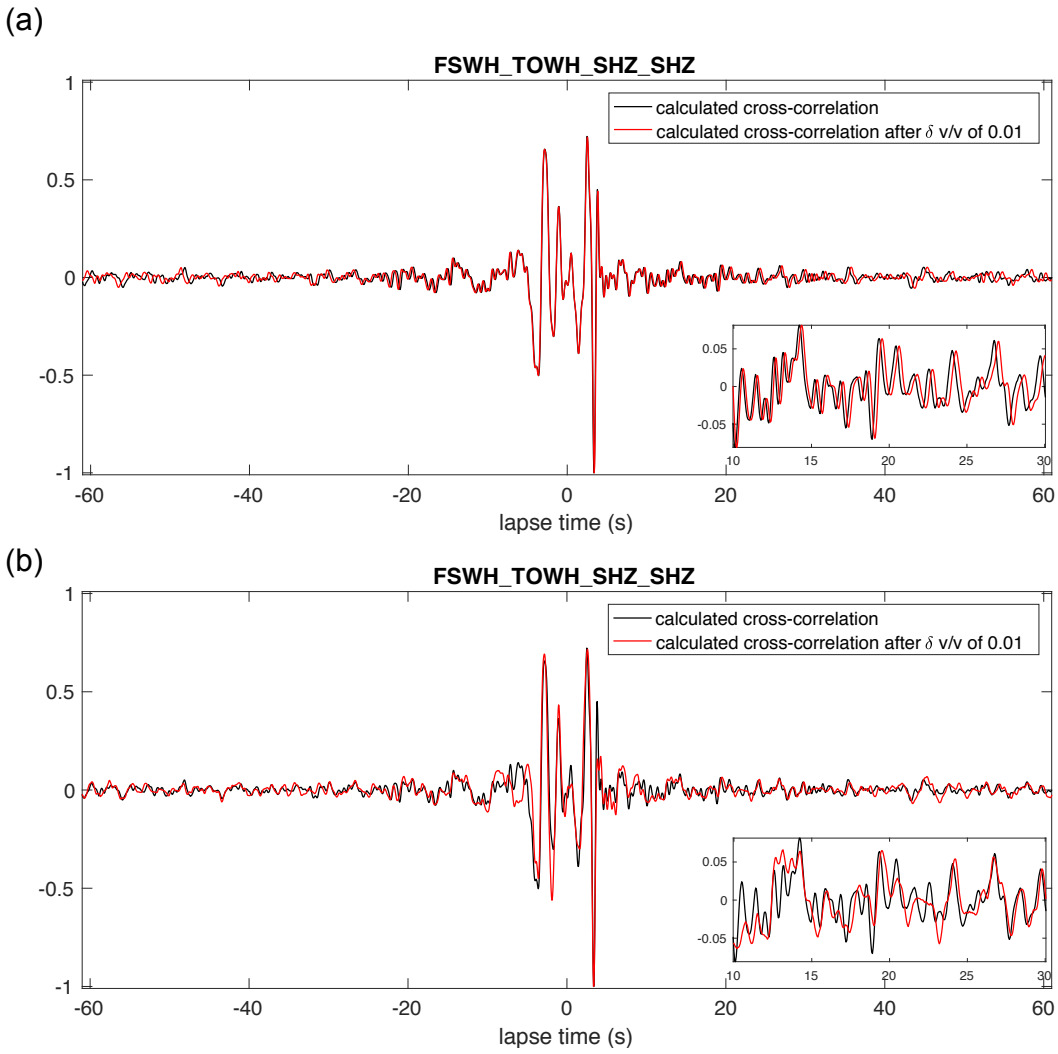

FIGURE 3.5 – (a) One cross-correlation from both vertical components of stations FSWH and TOWH. Black curve represents the calculated cross-correlation from noise recordings after preprocessing. Red curve represents the cross-correlation after artificially stretching by 0.01 velocity decrease compared to the black curve. (b) shows the same black curve as in (a). The red curve is another calculated cross-correlation after the 2011 Tohoku-Oki earthquake. Both are zoomed in from 10 s to 30 s.

3.4.3 Methods

Nowadays, there are three different fundamental ways for noise-based monitoring : stretching (Lobkis et Weaver, 2003; Sens-Schönfelder et Wegler, 2006), doublet (Poupinet *et al.*, 1984; Brenguier *et al.*, 2008a,b; Clarke *et al.*, 2011) and doublet – inversion

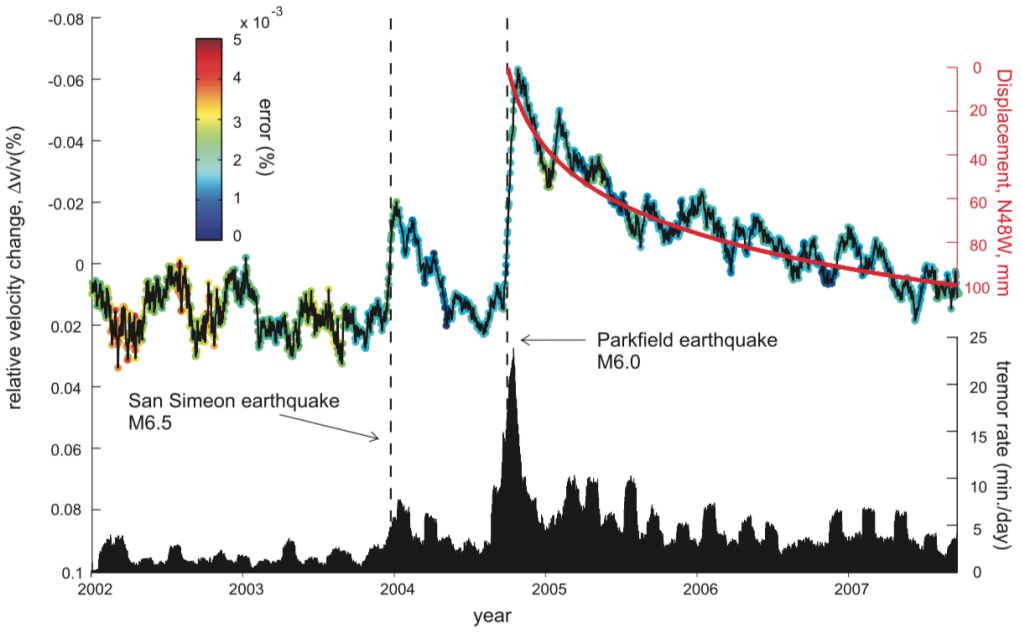

FIGURE 3.6 – afterBrenguier *et al.* (2008a)

(Brenguier *et al.*, 2014; Gómez-García *et al.*, 2018). In this section, we are going to briefly talk about the principles of the first two methods and focus on the third one, which has proved to be the most robust.

Basically, ambient seismic monitoring is based on time shift measurements between two cross-correlation functions. One is fixed as the reference (ccf_{ref}) and usually is the stack of a series of correlations over a specified period without big earthquakes. The other one is called current cross-correlation (ccf_{cur}), which is usually a daily or monthly stack of noise cross-correlations.

Stretching method is a time domain waveform based method. The ccf_{cur} is changed by stretching the waveform by a factor ϵ. Then the velocity changes are evaluated by solving an optimisation problem which from evaluation of cross-correlation coefficient between the ccf_{ref} and the stretched ccf_{cur} on the part of coda waves. The application of this method is fast and effective, however, it may be affected by the temporal variability of noise source frequency content (Zhan *et al.*, 2013; Daskalakis *et al.*, 2016).

Doublet method (called also **Moving Window Cross-Spectral** method) was

first introduced by Poupinet *et al.* (1984) for retrieving the relative velocity changes between earthquakes doublets. Recently, (Brenguier *et al.*, 2008a,b; Clarke *et al.*, 2011) apply this method to continuously recorded noise cross-correlations. This is a frequency domain measurement. The time changes between ccf_{cur} and ccf_{ref} are estimated in different time windows with an overlap. Usually, the moving window length is determined by the minimum frequency in the selected period range. The maximum lapse time used for measuring depends on the stability of the emerged Green's function by evaluating their energy envelops. The time shifts are measured within each window from the slope of a linear regression of the phase difference within the defined frequency range. The seismic velocity changes are given by the slope of the second linear regression of all the time shift from each moving window. Compared to stretching, the doublet method may be free of the bias from the temporally varied noise frequency content due to the separation of amplitude and phase spectra in the frequency domain before measuring time-shifts (Zhan *et al.*, 2013).

Doublet – Inversion Method is a new method that is based on the Doublet method (Brenguier *et al.*, 2014). The authors avoid the choice of an arbitrary ccf_{ref} function and improve the precision of the measurements by separately computing velocity changes for all of the possible daily ccf_{cur} functions for each station pair. Then they use a Bayesian least-squares inversion to retrieve the accurate daily continuous velocity change time series for every station pair. The basic steps of this method are represented as follows.

The definition of velocity changes at day i is :

$$\delta v_i = \frac{v_i - v_{ref}}{v_{ref}}. \tag{3.1}$$

Then the difference of velocity between day i and day j is :

$$\begin{aligned}
\delta v_j - \delta v_i &= \frac{v_i - v_{ref}}{v_{ref}} - \frac{v_j - v_{ref}}{v_{ref}} \\
&= \frac{v_j - v_i}{v_{ref}} \\
&= \frac{v_j - v_i}{v_i} \cdot \frac{v_i}{v_{ref}} \\
&= \delta v_{ij} \cdot \frac{v_i}{v_{ref}} \\
&= \delta v_{ij} \cdot \frac{v_i - v_{ref} + v_{ref}}{v_{ref}} \\
&= \delta v_{ij} \cdot (\delta v_i + 1) \simeq \delta v_{ij}.
\end{aligned} \tag{3.2}$$

This linear relationship of the velocity changes between ccf_{cur} to ccf_{cur} and ccf_{cur} to ccf_{ref} can be written as $d = Gm$ and allows inverting of daily velocity changes for n days from $n\,(n-1)\,/2$ pairs of ccf_{cur}. m is a vector of measured daily seismic velocity changes from day_1 to day_n using Doublet method. G is a sparse matrix of dimension $\left[\frac{n \cdot (n-1)}{2}, n\right]$ (see details in the supplementary materials by Brenguier *et al.* (2014)).

Then the solution of m is given by the following equation,

$$m = \left(G^t C_d^{-1} G + \alpha C_m^{-1}\right)^{-1} G^t C_d^{-1} d, \tag{3.3}$$

where C_d is a covariance matrix describing the Gaussian uncertainties of the data vector d. C_m is a priori covariance matrix weighted by the parameter α and is expressed as,

$$C_{mij} = \exp\left(\frac{-|i-j|}{2\beta}\right), \tag{3.4}$$

which sketches the correlation between the δv on day i and j. β is the parameter characterizing the correlation length (Lcorr), which actually controls the smooth strength of the inversion result.

This method is the most robust among the three presented methods. It has a big drawback : the amount of calculation is much more massive than the first two ways. But this method provides a very stable result by calculating all possible date-pairs noise cross-correlations. In this thesis, all the studies in Japan are based on the Doublet –

Inversion method.

3.4.4 Some Improvements

Although, the validation of noise-based monitoring has proved success even in cases when the Green's functions are not well reconstructed (Hadziioannou *et al.*, 2009; Weaver *et al.*, 2009), the improvement of the validated monitoring result can be realized through different ways. In this study, firstly the inversion after the doublet has a good ability to reduce fluctuations of velocity changes and can adjust the parameters to focus on long-term or short-term tendency. Nine components correlations also improve the ability of detection of earthquakes-related seismic velocity reductions. Fig. 3.7 shows the results of seismic velocity changes from different combinations of 3 components for station pair FSWH-TOWH using Lcorr = 5. Tohoku-oki earthquake-related seismic velocity decrease can be identified from each component-pair.

Also, the average of these nine velocity changes curves further enhances the identification of earthquake-related velocity changes shown in Fig.3.9 with different Lcorr values.

We compare the results by normal average and weighted (according to their errors) over the 9 components (Fig. 3.9). They are slightly different, and we take the latter one and apply for all the station-pairs.

For each site, we calculate all the possible cross-correlations within a distance of smaller than 30 km, measure the velocity changes through the cross-correlations with different directions, and average the results. This process is equivalent to superimposing cross-correlations in different directions to achieve a stable result from the theoretical Green's function.

It is also vital to primarily stabilize cross-correlations with the help of different ways, ex : using the Correlation of Correlations (C3) (Stehly *et al.*, 2008) to better retrieve the Green's function, even in the presence of a directive and poorly oriented ambient noise. Because coda waves of correlation are better equipartitioned compared to the noise sources. As well as applying filters in the curvelet transform space Stehly *et al.* (2011) to improve the SNR of stacked correlations. More recently, Moreau *et al.* (2017) verify the efficiency of the SVD-based Wiener filter on stabilizing correlation functions. We also test the SVD-based Wiener filter on cross-correlations of NN component-pair

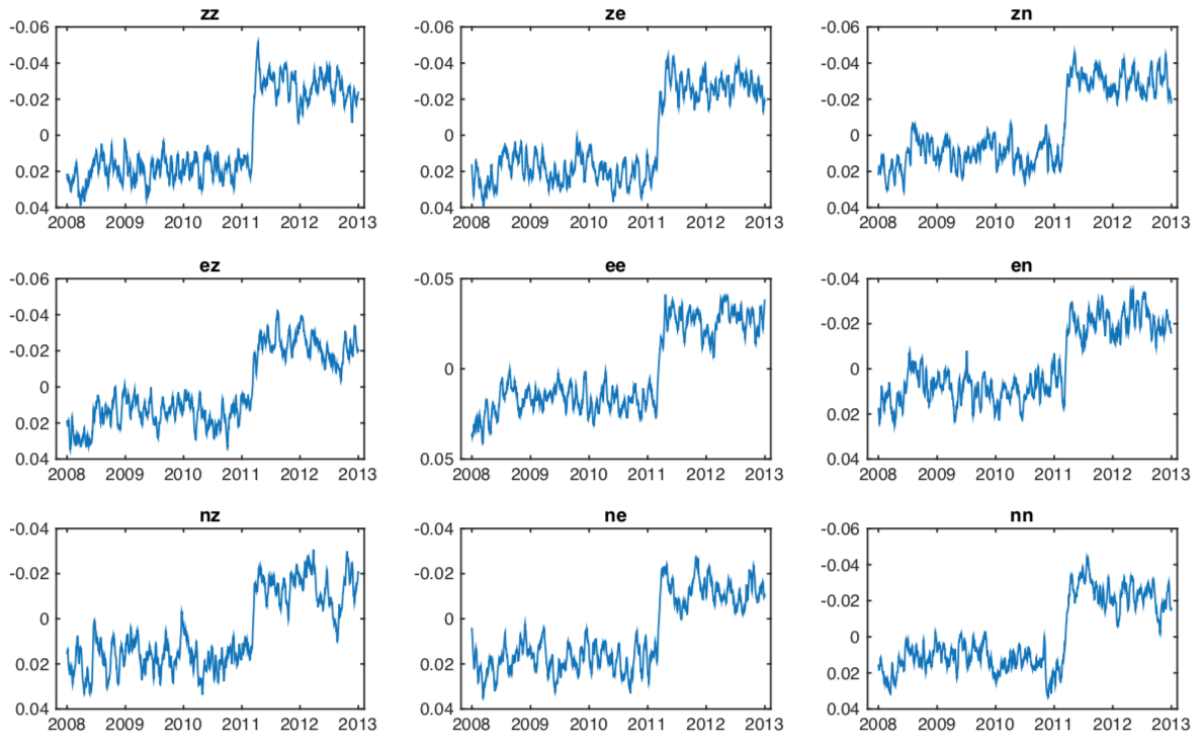

FIGURE 3.7 – Seismic velocity changes (%) from different combinations of 3 components for station pair FSWH-TOWH using Lcorr = 5.

of tiltmeter KMYH-NKWH from 2008 to 2012 with daily resolution. After filtering, the noise level of correlations decrease, and the signal-to-noise ratio is enhanced. We see the continuous coda waves till $\pm 400s$ lapse time. The only problem is that SVD filtering is time consuming when the dataset is huge as in Japan.

3.5 Other Applications

In addition to these deep-developed applications described above, there are currently also several popular applications such as the study on the amplitude information carried by the ambient field (Prieto *et al.*, 2011). The amplitude information contains both amplification effects from elastic structure and attenuation effects. The noise-based attenuation tomography (Lawrence et Prieto, 2011) provides complementary information to the noise-based or earthquake-based tomography. The reconstructed Green's function from ambient noise field can also used to predict long-period ground motion from earth-

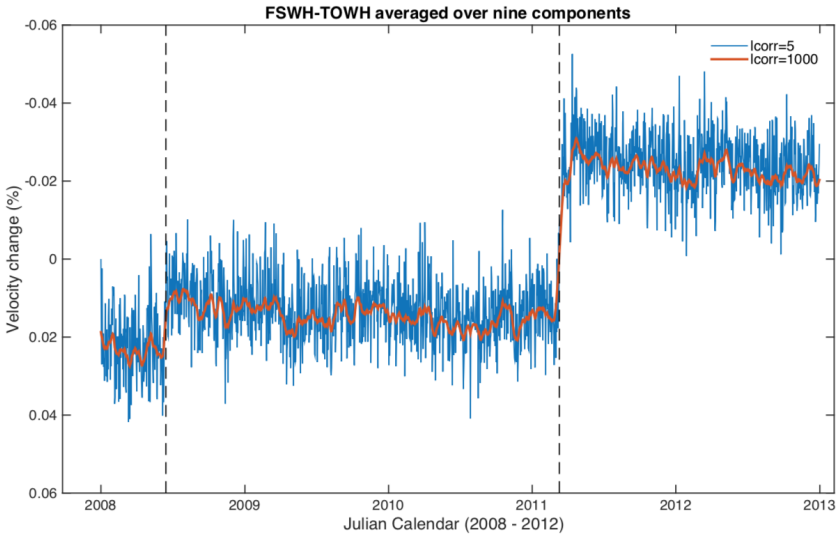

FIGURE 3.8 – Mean seismic velocity changes (%) from 9 combinations of 3 components for station pair FSWH-TOWH using Lcorr = 5 (red) and Lcorr = 1000 (blue).

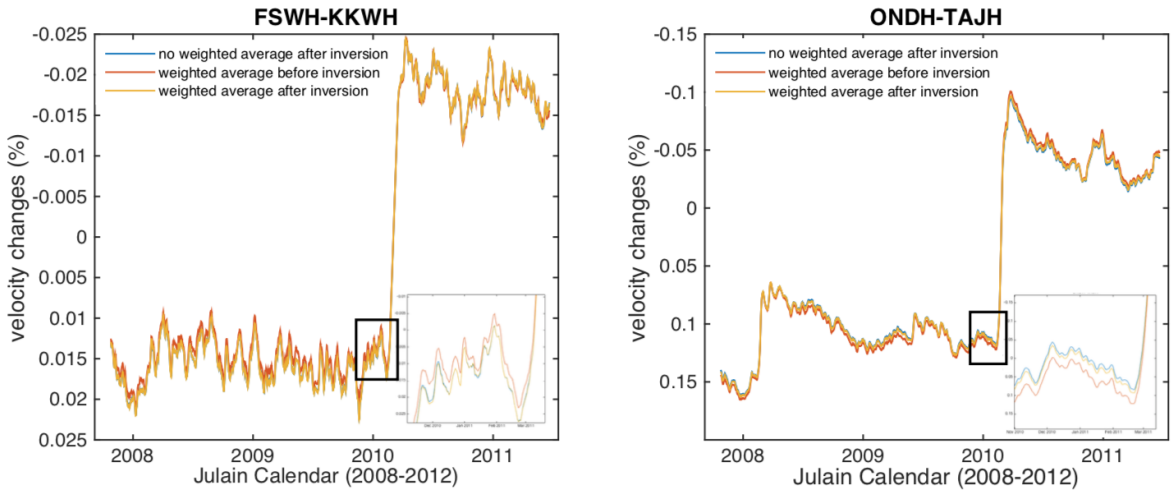

FIGURE 3.9 – Comparison of mean seismic velocity changes from different average method over 9 components.

quakes. The virtual earthquake approach developed by Denolle *et al.* (2013) shows clear improvements of the predicted ground motion related to the surface impulse response. Various earthquake-based scientific applications will be strongly reconsidered and further developed in the ambient seismic field.

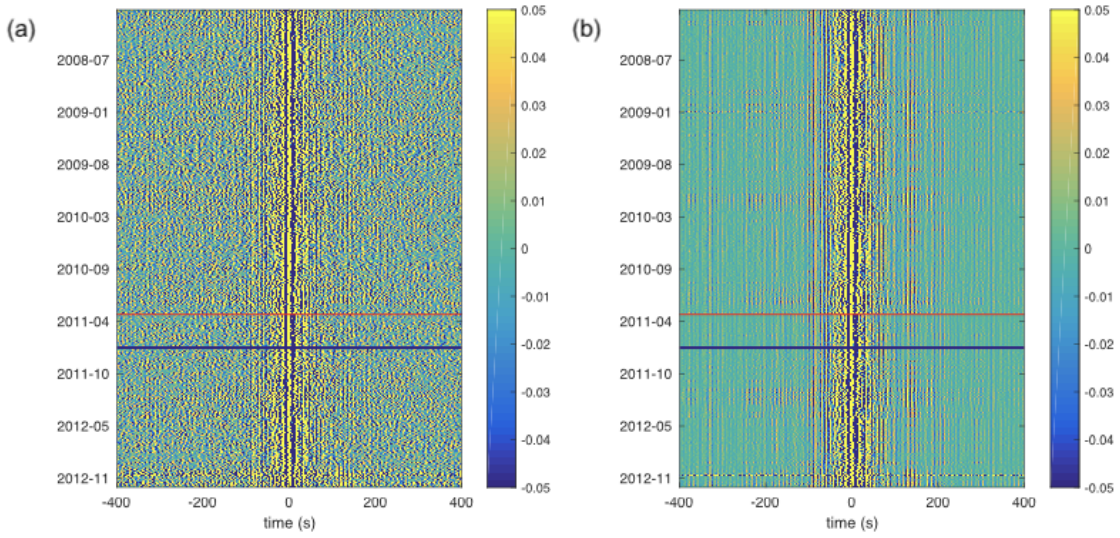

FIGURE 3.10 – Cross-correlations of one component pair KMYH-NKWH-NN from 2008 toe 2012 in 8 – 50 s. The left one is without any filter. The right one is after applying the SVD-based Wiener filter. Red line indicates the day of Tohoku-oki earthquake. Blue line indicates the gap of data.

Deuxième partie

Environmental Crustal Seismic Velocity Changes

Chapitre 4

Seasonal Crustal Seismic Velocity Changes throughout Japan

Sommaire

4.1 Abstract 53
4.2 Introduction 54
4.3 Data and Methods 55
4.4 Analysis of Seasonal Variations in $\delta v/v$ 58
4.4.1 Seasonality Strength 58
4.4.2 Three-months Average Seismic Velocity Changes 58
4.4.3 Sub-Areal Analysis 60
4.5 Linear Model Correction 69
4.6 Discussion and Conclusion 73
4.7 Appendix 74
4.7.1 A1 : Comparison with GRACE 74
4.7.2 A2 : Time shift measurement 75
4.8 Statistical Analysis of the Seismic Velocity Changes 78

In this chapter, we monitor the seismic velocity changes in the frequency band from 0.15 Hz to 0.90 Hz throughout Japan. We focus on studying some seasonal effects and identifying the dominant environmental factors in charge of the repeated annual patterns in different locations. We develop a linear model based on different local meteorological and oceanographical observations to simulate the seasonal signals and subtract them from

the measurements. In addition to the content related to the paper by Wang *et al.* (2017), we also do some statistical analysis by comparing the time series of seismic velocity changes before and after correcting the seasonal effects. Statistical results illuminate that seismic velocity changes after removing the seasonal signals are more consistent with Gaussian distribution compared with the directly measured velocity changes.

Qing-Yu Wang[1], Florent Brenguier[1], Michel Campillo[1], Albanne Lecointre[1], Tetsuya Takeda[2,3], and Yosuke Aoki[4]

published in JGR Solid Earth, 2017

1 Univ. Grenoble Alpes, CNRS, ISTerre, 38000 Grenoble, France.
2 National Research Institute for Earth Science and Disaster Prevention, Tsukuba Japan.
3 Ministry of Education, Culture, Sports, Science and Technology, Tokyo Japan.
4 Earthquake Research Institute, University of Tokyo, Tokyo, Japan.

4.1 Abstract

Noise-based crustal seismic velocity changes are known to be affected by environmental perturbations, such as rainfall, atmospheric pressure loading, and temperature changes. Similar to geodetic observations, these external perturbations can mask the effects of tectonic and volcanic processes. In this study, we benefit from the dense Hi-net short-period seismic network that covers the entire Japan to measure continuous changes in seismic velocities over a few years, using noise-based seismic monitoring. Some strong seasonal seismic velocity changes are observed in both southern Japan (Kyushu Island) and northern Japan (Hokkaido Island). Decreasing of seismic velocities in summer in southern Japan can be clearly explained by a model of increased crustal fluid pore pressure associated with high rainfall. In northern Japan, it is necessary to adopt a more complex model to explain the observed seismic velocity variations, which takes into account precipitation, snow depth, and sea-level changes. Moreover, western and eastern Hokkaido Island show very different responses to these different external perturbations. The models developed are used to remove the seasonal components of the seismic velocity changes. The minimum remaining detectable seismic velocity change reduces to 10^{-5}, which allows detection of crustal responses to small earthquakes that are previously hidden in the strong seasonal perturbations.

4.2 Introduction

Advances in ambient noise correlation methods (Campillo et Paul, 2003; Shapiro et Campillo, 2004; Campillo, 2006) have led to continuous monitoring of temporal variations of seismic velocity changes ($\delta v/v$) in the crust. Noise-based monitoring has provided insights into tectonic and volcanic processes, to allow detection of long-term post-seismic relaxation in fault zones (Brenguier *et al.*, 2008a; Hobiger *et al.*, 2012; Froment *et al.*, 2013), velocity decreases as precursors of volcanic eruptions (Wegler et Sens-Schönfelder, 2007; Brenguier *et al.*, 2008b, 2011; Obermann *et al.*, 2013), and interactions between seismic and volcanic systems (Brenguier *et al.*, 2014; Taira et Brenguier, 2016). Similar to geodetic observations (Heki, 2001), crustal seismic velocities are affected by external environmental perturbations, such as rainfall (Sens-Schönfelder et Wegler, 2006; Meier *et al.*, 2010; Tsai, 2011; Hillers *et al.*, 2014), thermoelastic stress (Meier *et al.*, 2010; Hillers *et al.*, 2015a), and atmospheric pressure (Silver *et al.*, 2007a). In volcanic areas, correction of these environmental seismic velocity perturbations improves the detection capability of precursors to volcanic eruptions (Rivet *et al.*, 2015).

Japan is prone to frequent seismic and volcanic activities. A dense distribution of the high-sensitivity seismograph network (Hi-net) (Okada *et al.*, 2004; Obara *et al.*, 2005) allows us to monitor $\delta v/v$ in the upper crust using 718 stations. In this study, we investigate seasonal crustal seismic $\delta v/v$ over a number of years and across the whole of Japan.

We apply here the approach of Brenguier *et al.* (2014) to continuous seismic records from the permanent short-period seismic network in Japan. We measure the accurate daily seismic $\delta v/v$ starting from 2008, and observe co-seismic and post-seismic responses to the M_w 6.9, 2008 Iwate-Miyagi Nairiku and M_w 9, 2011 Tohoku-Oki earthquakes. In addition to the relative seismic velocity decreases (10^{-3}) that are coincident with these earthquakes, the seasonal seismic velocity changes with amplitudes of 10^{-4} for both Kyushu Island and the northeastern corner of Hokkaido Island are observed. The summer-time reductions of seismic velocities in Kyushu can be clearly explained by a model of crustal fluid pore pressure increase that is associated with strong rainfall in summer. The best fitting curve in the northeastern corner of Hokkaido Island suggests an origin of both precipitation and snow. We also study some other regions that show strong seasonal repeatability with relatively small amplitudes of the seasonal changes in $\delta v/v$. Detailed comparative analysis between seismic measurements and different environ-

mental factors shows that the seasonal effects differ greatly from one region to another. It is necessary to adopt a more complex model to explain the observed seismic velocity changes on the basis of the meteorological and oceanographic observations. Finally, we introduce a linear model to remove the seasonal components of seismic $\delta v/v$. This procedure improves the detection capability of the crustal responses to small earthquakes that are previously hidden in these strong seasonal perturbations.

4.3 Data and Methods

We measure relative seismic velocity changes ($\delta v/v$) from the continuous noise recordings of the Hi-net stations in Japan (Figure 4.1a). We compiled a dataset composed of 718 Hi-net stations. The dataset that we were able to gather consists of 501 stations for north Japan with data spanning from 2008 to 2012 and 217 stations for south Japan with data spanning from 2011 to 2012.

To improve the temporal stability of the noise records before correlation, we apply one-bit normalization (Campillo et Paul, 2003; Shapiro et Campillo, 2004), which removes some irregular events and preserves the phase of the signal during this period. In the frequency domain, spectral whitening in the band from 0.08 Hz to 2.0 Hz can decrease the effects of temporal changes in the microseismic sources (Shapiro *et al.*, 2006). In the present study, we reconstruct the Green's functions by calculating the hourly cross-correlation functions using both the vertical and horizontal components, of station pairs up to 30 km apart to restrict the amount of measurements. Daily cross-correlation functions are provided by averaging the hourly cross-correlation functions, which improves the stability of the daily cross-correlation functions and enhances the signal-to-noise ratio. Delay measurements from the nine correlations that result from the three-component recordings enhance the stability of the evaluation of $\delta v/v$.

Based on these daily cross-correlation functions, we perform the doublet method similar to Brenguier *et al.* (2014) using a Bayesian least-squares inversion to retrieve accurate daily relative $\delta t/t$ time series for every component pair. The final curve of $\delta t/t$ is centered around 0. The doublet measurements are performed from $-60s$ to $+60s$ of time lag, and in the frequency band from 0.15 Hz to 0.90 Hz. At these frequencies, the depth sensitivity of the seismic coda waves to velocity perturbations can be considered similar to the surface-wave sensitivity (Obermann *et al.*, 2013, 2016). The depth sensitivity of the phase velocity of Rayleigh wave to a shear-wave velocity perturbation (Froment

et al., 2013) indicates that our measurements essentially characterize $\delta v/v$ to within 8 km in the upper crust. Because coda waves of the ambient noise correlation result from scattering, using this tail portion of the cross-correlation functions can effectively reduce the influence of the directivity that arises from the inhomogeneous distribution of the noise sources (Colombi *et al.*, 2014). Furthermore, the feasibility of seismic monitoring with multiple scattered waves has been demonstrated, even if the Green's function is not perfectly reconstructed (Hadziioannou *et al.*, 2011). Considering that the medium undergoes a homogeneous change, the $\delta t/t$ accumulates linearly with the lapsed time. The relative $\delta v/v$ is equal to -$\delta t/t$ in case of a homogeneous perturbation. Hence, the later coda wave arrivals are sensitive to very small velocity changes in the medium. Instead of using a simple arbitrary stack as the reference function, we enhance the accuracy by using a linear inversion of every day-to-day $\delta v/v$ measured with the doublet method (Brenguier *et al.*, 2014). Based on the frequency domain phase measurements, the doublet method is hardly affected by possible seasonal changes in the spectral content of the ambient noise, as might be the case for the stretching method (Zhan *et al.*, 2013; Hillers *et al.*, 2015a).

For each station pair, we average $\delta t/t$ by weighting according to the quality of the individual phase measurements over all of the nine components of the cross-correlations. Furthermore, for each station, we average $\delta v/v$ over all nearby station pairs less than 30 km apart. This procedure additionally improves the precision, and furthermore, it reduces the effects from the directivity of the sources. We can finally monitor the relative seismic $\delta v/v$ for 718 Hi-net stations distributed across the whole of Japan.

Figure 4.1b shows four randomly selected time series to demonstrate the seismic $\delta v/v$ in the different regions. The shapes and amplitudes of these time series are easily distinguishable from one region to another. From north to south, station TAJH (located in eastern Honshu) shows strong seismic velocity decreases that are coincident with the 2008 Iwate-Miyagi Nairiku earthquake and the 2011 Tohoku-Oki earthquake. The velocity tends to recover after the Iwate-Miyagi Nairiku earthquake. In spite of this, the $\delta v/v$ had not returned to its previous level when the Tohoku-Oki earthquake occurred. Station MWDH in central Honshu shows both the rapid velocity decrease due to the Tohoku-Oki earthquake and some strong seasonal fluctuations that correspond to velocity decreases in summer and increases in winter. Station OKBH shows two decreases in the seismic velocity related to the nearby 2009 Shizuoka earthquake and the 2011 Tohoku-Oki earthquake. The stations in the western Japan that are represented by the blue

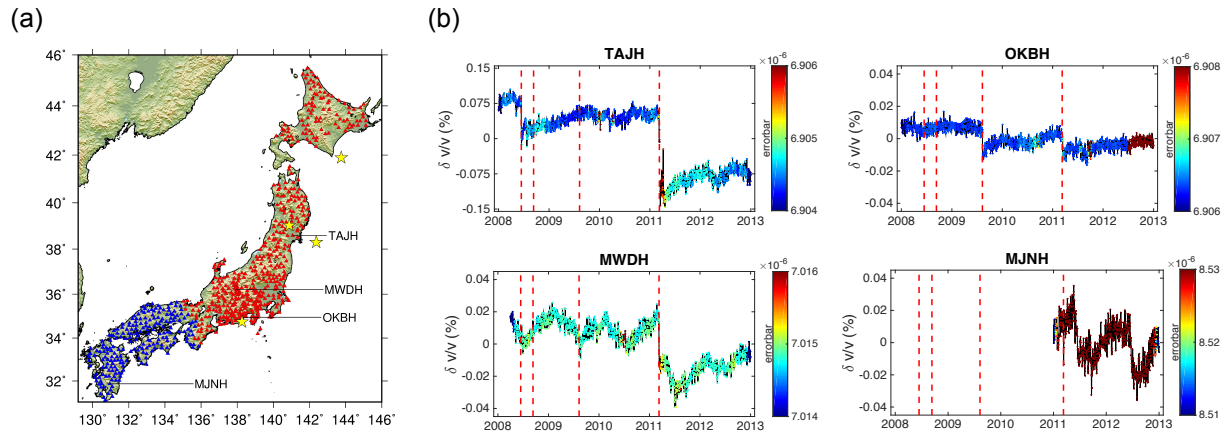

FIGURE 4.1 – (a) Distribution of the Hi-net stations in Japan. The blue triangles indicate data recorded from 2011 to 2012. The yellow stars indicate the locations of the epicenters of four earthquakes : M_w 6.8, 2008 Tokachi-Oki earthquake ($41.892°N$ $143.754°E$) ; M_w 6.9, 2008 Iwate-Miyagi Nairiku earthquake ($39.030°N$ $140.881°E$) ; M_w 6.2, 2009 Shizuoka earthquake ($34.743°N$ $138.264°E$) ; and M_w 9, 2011 Tohoku-Oki earthquake ($38.297°N$ $142.373°E$). (b) Randomly selected time series for the seismic $\delta v/v$ for the four stations, TAJH, MWDH, OKBH, and MJNH. The scattering of the colored points indicate the error. The four dashed vertical red lines indicate the days of Shizuoka earthquake, Iwate-Miyagi Nairiku earthquake, and Tohoku-Oki earthquake (from left to right).

triangles (Figure 4.1a) show seismic $\delta v/v$ in 2011 and 2012. MJNH in Kyushu exhibits strong seasonal changes, with increases in winter and decreases in summer. The velocity decreases from June and reaches its lowest in July, during the rainy season. However, the recovery of the seismic velocity is more gradual compared to the abrupt reduction. The shapes of these time series are complicated in different regions and cannot be easily represented by single sinusoidal curves, as presented by Hobiger *et al.* (2012). These seasonal characteristics suggest that the seismic $\delta v/v$ in Japan are subject to nonidentical environmental factors in different areas. In other words, the seasonality is strongly region-dependent.

4.4 Analysis of Seasonal Variations in $\delta v/v$

4.4.1 Seasonality Strength

We observe large seasonal variations in seismic velocity across Japanese islands. These seasonal signals should reflect the *in-situ* physical changes in the upper crustal properties, but limit the possibility to correctly track the tectonic changes. We want to show areas that are strongly affected by the seasonal variations. The Pearson correlation coefficients are calculated for the annual signals between two different years, and the mean correlation coefficients are mapped. The annual signals in the north are chosen from years 2008, 2009, and 2010, when there is no large earthquake. Figure 4.2b shows an example of how the correlation coefficient (CC) is computed for station KWNH in the west of Honshu, as according to equation 4.1.

$$CC\,(y_1,\ y_2) = \frac{cov\,(y_1,\ y_2)}{\sigma_{y_1}\sigma_{y_2}}, \tag{4.1}$$

where σ_{y1} and σ_{y2} are the variances of annual signal in two different years. Then the mean correlation coefficients with a spatial resolution of 1 km using a linear interpolation are mapped after applying Gaussian filter with 300 km full width. Assuming that a correlation coefficient ≥ 0.6 signifies large seasonal effects and the correlation coefficients represent a seasonality strength, the map of the seasonality strength (Figure 4.2a) shows that the seasonal effects are very strong in Hokkaido and Kyushu, and Honshu along the Sea of Japan.

4.4.2 Three-months Average Seismic Velocity Changes

To map the quarterly seismic $\delta v/v$ (Figure 4.3), the $\delta v/v$ is averaged over each 3-month period, beginning from January. Spatial smoothing is applied with a 300 km full width Gaussian filter. In northern Japan, the $\delta v/v$ is demeaned, detrended and averaged from the years 2009 to 2010, to avoid the large velocity reduction that is coincident with the 2008 Iwate-Miyagi Nairiku earthquake and the 2011 Tohoku-Oki earthquake. In southern Japan, the $\delta v/v$ is the detrended mean over the years 2011 to 2012.

The quarterly maps give an intuitive sense of the temporal and spatial variations of the seismic velocities. Large anomalies can be found in Kyushu and in the northeastern

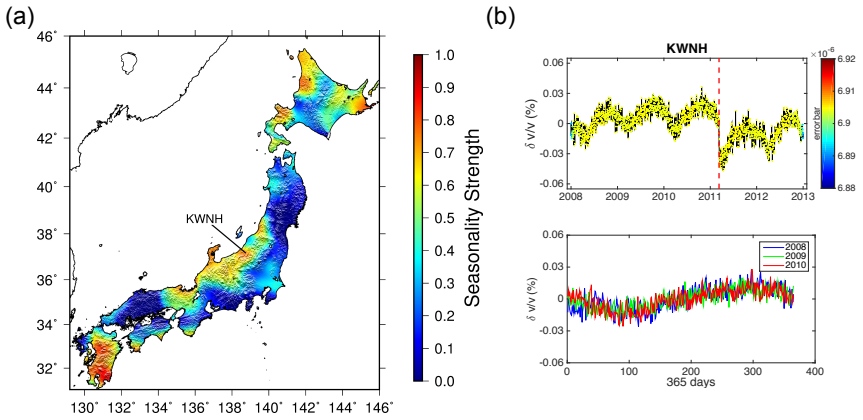

FIGURE 4.2 – (a) Seasonality strength distribution in Japan. (b) The example of station KWNH. The vertical dashed red line indicates the day of the Tohoku-Oki earthquake. The upper record shows the seismic $\delta v/v$ time series at station KWNH with color-coded errors (scale, right). The lower record shows the annual signals from 2008 to 2010.

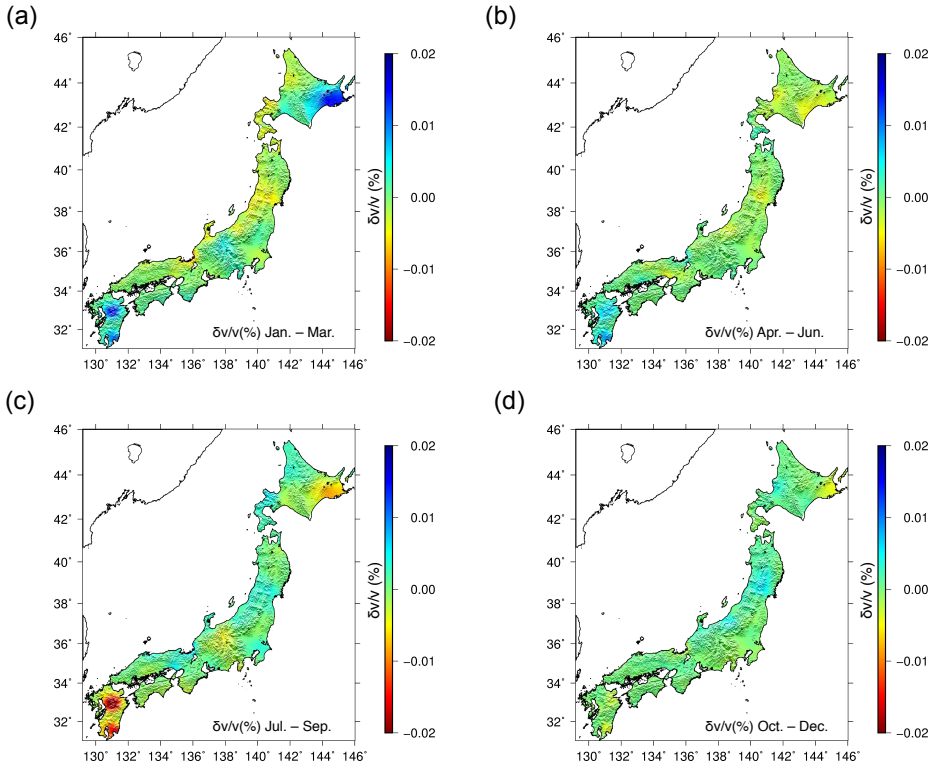

FIGURE 4.3 – Quarterly seismic $\delta v/v$ in Japan. (a) January to March. (b) April to June. (c) July to September. (d) October to December.

corner of Hokkaido (Figure 4.3a, c). However, the anomalies show different features in these two regions. Kyushu shows large decreases in seismic velocity in the third quarter. In contrast, the velocity in northeastern Hokkaido begins to decrease in the second quarter, and continues to be negative in the third quarter. This area is dominated by an increase in the seismic velocity in the first quarter. This difference suggests that the seismic velocities for these two islands may be controlled by different physical mechanisms or different variations of a single physical mechanism, or both.

The quarterly variation of seismic $\delta v/v$ is globally correlated with the quarterly variation of total water storage derived from the gravity-change measurements by GRACE (Gravity Recovery and Climate Experiment, available at http ://grgs.obs-mip.fr/grace/). The relatively positive $\delta v/v$ in the north in the first quarter is in agreement with high Equivalent Water Height (EWH, cm) due to snow depth in winter. The relatively negative $\delta v/v$ in the south in the third quarter corresponds to high EWH due to rainfall in summer. More complicated process has occurred in central Japan. Detailed comparison of quarterly variations of seismic $\delta v/v$ and GRACE is in appendix A. We believe that in Kyushu the negative changes in the velocity in the third quarter can be associated with the heavy rainfall in the monsoon season. The rapid increase in the pore pressure due to the large amount of precipitation might be the main driving force that leads to the decrease in seismic velocity. In contrast to Kyushu, Hokkaido has heavy snowfall every year. The combination of these various external environmental factors might produce complex deformation of the crust. Thus it is necessary to study the seasonal effects separately in these different areas, and to identify the predominant external forces.

4.4.3 Sub-Areal Analysis

The seismic $\delta v/v$ in both Kyushu and the northeastern corner of Hokkaido shows large seasonal fluctuations. The specific seasonal characteristics of each of these regions requires them to be analyzed separately. Seasonal seismic $\delta v/v$ are known to be influenced by meteorological effects (Sens-Schönfelder et Wegler, 2006; Meier *et al.*, 2010; Froment *et al.*, 2013; Hillers *et al.*, 2014; Rivet *et al.*, 2015). Thus, in this section, the time series of $\delta v/v$ are compared with the different meteorological effects. All of the meteorological data are from the Japan Meteorological Agency.

4.4.3.1 Kyushu Velocity Change Anomaly

Kyushu is located in the southwest of Japan. Little snowfall is recorded for Kyushu, except at high altitudes. In contrast, there is intense precipitation in the monsoon season. In the present study, the time series for $\delta v/v$ is calculated for 74 Hi-net seismic stations (Figure 4.4a), from 2011 to 2012.

Figure 4.4b shows that in Kyushu, temporal evolutions of seismic velocity in 2011 and 2012 are similar with transient reductions of velocity in July by an order of 10^{-4} and subsequent recoveries. Then the velocities recover gradually to their initial levels. This periodic velocity change is mostly controlled by annual variations of precipitation. Sens-Schönfelder et Wegler (2006) first noted that a decrease in the seismic velocity at Merapi Volcano is solely associated with precipitation. In southern Japan, Nakata et Snieder (2012) have also estimated that shear-wave velocity changes are negatively correlated with precipitation, using vertical arrays of surface and downhole seismic sites. The increase in pore water pressure leads to a decrease in the effective pressure of the rock, and reduces the shear modulus (Snieder et Beukel, 2004; Meier *et al.*, 2010; Tsai, 2011; Froment *et al.*, 2013; Hillers *et al.*, 2014; Rivet *et al.*, 2015).

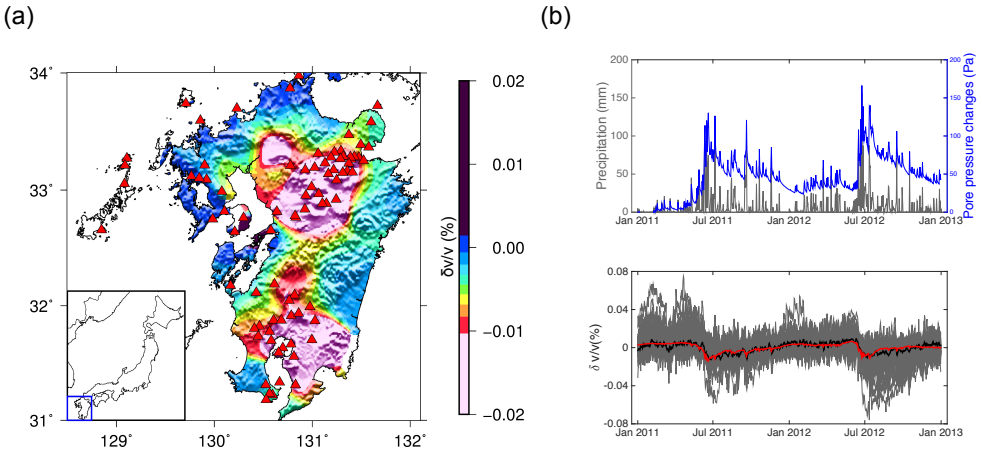

FIGURE 4.4 – (a) Mapping of the mean seismic $\delta v/v$ in July from 2011 to 2012 from the 74 Hi-net stations. The red triangles indicate locations of the quaternary volcanoes. (b) Upper record : Daily mean precipitation for Kyushu (gray) and computed relative diffused pore pressure changes (blue) from the 129 meteorological stations. Lower record : Time series of $\delta v/v$ for the Hi-net stations (gray) and the averaged $\delta v/v$ time series (black). The red curve gives the synthetic $\frac{\delta v}{v}_{syn}$ curve.

In our analysis, the mean seismic $\delta v/v$ (Figure 4.4b) suggests that the strong annual

variations are negatively correlated with the mean precipitation. Therefore, it appears that the direct ground water loading effect, that can increase $\delta v/v$, is not predominant. Instead, the pore pressure diffusion is more likely to be the dominant mechanism that controls the seasonal effects for Kyushu. The infiltration of rain water produces delayed pore pressure changes in the first kilometers of the crust. When the daily precipitation is at its maximum in July, the decrease in the seismic velocity also tends to be at its maximum. Meanwhile, $\delta v/v$ are slightly delayed due to the hydraulic diffusion, compared to the peaks of the daily precipitation. We map the mean seismic $\delta v/v$ in July over the years 2011 and 2012 after Gaussian smoothing of width 100 km. Figure 4.4a shows that the locations of the strong variations correlate well with the central and southern volcanic zones. The crustal rock in the volcanic zones should have more cracks and be more sensitive to external stress changes. This finding confirms the high susceptibility of velocity changes to external perturbations in volcanic regions, as reported by Brenguier *et al.* (2014).

The poroelastic effect is then computed from the daily precipitation records. Based on the one-dimensional fully coupled diffusion equation developed by Talwani *et al.* (2007) and used by Rivet *et al.* (2015) to improve the monitoring, the superposing pore pressure diffusion changes are calculated using equation 4.2. Here, we consider the direct pore pressure changes ($P(r,t)$) that are due to diffusion within a certain distance r from the daily precipitation at the surface.

$$P\left(r,\ t\right) = \sum_{i=1}^{n} \delta p_i \, erfc\left[\frac{r}{\left(4c\left(n-i\right)\delta t\right)^{1/2}}\right], \tag{4.2}$$

where δt is the time increment from the first day i, δp_i is the precipitation load changes ($\rho \cdot g \cdot \delta h_i$) at the sampled instant t_i, c is the diffusion rate (m^2/s). For each day at each station, the pore pressure is the mean value within the certain distance r. In this study, r is 8 km the same as depth sensitivity of seismic $\delta v/v$. The modeled seismic velocity changes ($\frac{\delta v}{v}_{syn}(t)$) can be estimated using a transfer function as follows :

$$\frac{\delta v}{v}_{syn}(t) = \langle \frac{\delta v}{v}(t) \rangle + \frac{cov\left(\frac{\delta v}{v}(t),\ P(t)\right)}{var\left(P(t)\right)} * \left(P(t) - \langle P(t) \rangle\right), \tag{4.3}$$

where $\langle\rangle$ is the average over time. The diffusion rate is estimated by minimizing squares residual σ^2 between the modeled $\frac{\delta v}{v}_{syn}$ and the measurement :

$$\sigma^2(c) = \frac{1}{n}\sum_{i=1}^{n}\left(\frac{\delta v}{v}(i) - \frac{\delta v}{v}_{syn}(i,c)\right)^2. \tag{4.4}$$

Here, n indicates the number of days. We find $c = 1m^2/s$ as an optimal diffusion rate for calculating changes of pore pressure in the following study. The mean pore pressure changes (Figure 4.4b, blue curve) can be transformed into the synthetic $\frac{\delta v}{v}_{syn}$ using equation 4.3. The synthesis (Figure 4.4, red curve) correlates well with the real seismic $\delta v/v$. We confirm that the pore pressure changes from the precipitation control of the seasonal seismic $\delta v/v$ in Kyushu.

4.4.3.2 Hokkaido Velocity Change Anomaly

Hokkaido is located in the northeast of Japan. Seismic $\delta v/v$ time series are plotted along the longitude in Figure 4.5b, for 2008 to 2012. The seasonal effects are much stronger in the northeastern corner (from $144°E$ to $145°E$) than in the other areas. The velocities increase from the beginning of each year, and reach their maximum in February, and then begin to decrease. In other areas in Hokkaido, the seismic velocities show annual variations with increases and decreases in summer and winter, respectively. These fluctuations are smaller than in the northeast. We can observe decreases of velocity that are coincident with the Tohoku-Oki earthquake for both sides of Hokkaido. In addition, we can observe velocity decreases following the 2008 Tokachi-Oki earthquake just for the stations in the east. This confirms that these observations are very sensitive to changes in the crust. The seasonal effects can interfere with the $\delta v/v$ related to earthquakes. The different features of the annual fluctuations reveal that the seasonal effects for the two sides of Hokkaido might be dominated by different external factors.

Figure 4.6b shows that the mean seismic $\delta v/v$ in eastern Hokkaido tends to increase at the beginning of each year, and then to decrease in summer. The amplitudes of fluctuations are more than 10^{-4}. The mean daily snow depth is about 50 cm, and this reaches its maximum in winter when the increasing rate of velocity is maximum. The mean daily precipitation is less than 50 mm and is concentrated in the summer, during which $\delta v/v$ decreases. From these observations, it can be seen that the mean seismic $\delta v/v$ in the east is negatively correlated with mean precipitation and positively correlated with mean snow depth. The changes in the diffused pore pressure P induced by precipitation can be computed using equation 4.2, as with Kyushu. It would thus appear that the seismic $\delta v/v$

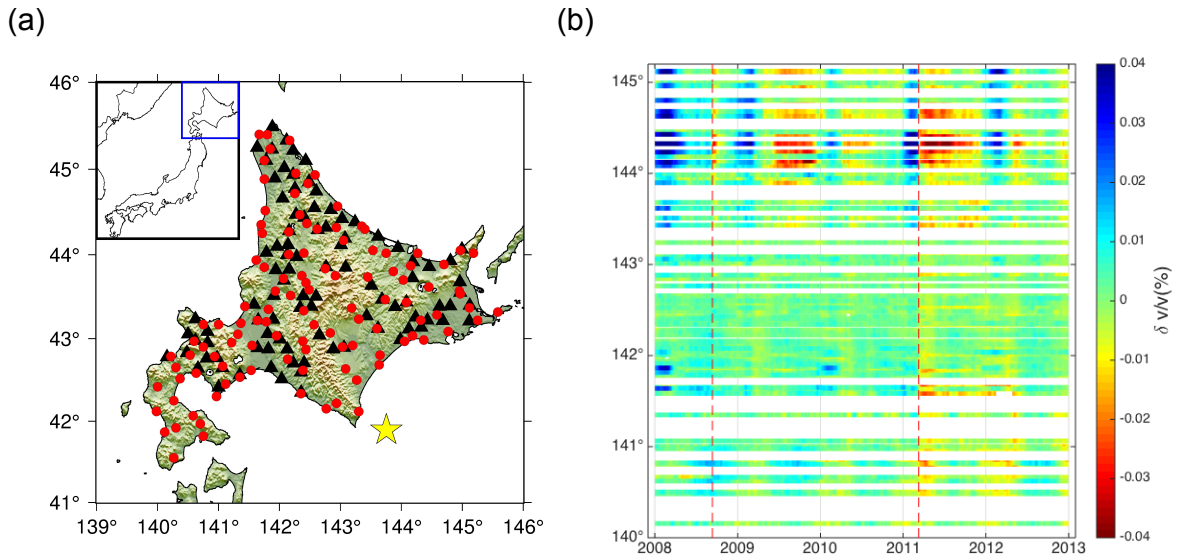

FIGURE 4.5 – (a) Map of the 95 Hi-net seismic stations (black triangles) and the 112 climate stations (red points) in Hokkaido. (b) Relative seismic $\delta v/v$ along the longitude from 140°E to 145°E. The dashed red lines indicate the days of Tokachi-Oki earthquake and Tohoku-Oki earthquake, from left to right.

is controlled by a combination of the changes in pore pressure and snow depth. Here, we consider two possible effects of the snow depth. The first is the direct elastic loading effect that has been observed by geodetic measurements (Heki, 2001; Grapenthin *et al.*, 2006). This is also observed in Mount St. Helens by seismic monitoring (Hotovec-Ellis *et al.*, 2014). The other effect is that the snow cover impedes infiltration and recharging of the groundwater (Seiler et Gat, 2007), thus decreasing pore pressure. We can summarize these effects by considering a linear relationship between seismic $\delta v/v$ and the combined effects of both the changes in pore pressure and snow depth, according to equation 4.5.

$$\frac{\delta v}{v}_{syn} = a \cdot P + b \cdot S + C, \tag{4.5}$$

where a and b are the coefficients of the daily mean precipitation P and the mean snow depth S, respectively, and C is a constant with offset parameters. The synthetic curve of $\frac{\delta v}{v}_{syn}$ in the northeastern corner of Hokkaido is then constructed, as shown in Figure 4.6b. This curve is consistent with the mean measurements in this area. The best fit for a and b are $-4.9 * 10^{-6} Pa^{-1}$ and $2.1 * 10^{-6} cm^{-1}$), respectively. According to the best fitting coefficients, both poroelasticity and snow depth have roles in the seasonal effects in northeastern Hokkaido. Daily precipitation and snow depth are negatively and

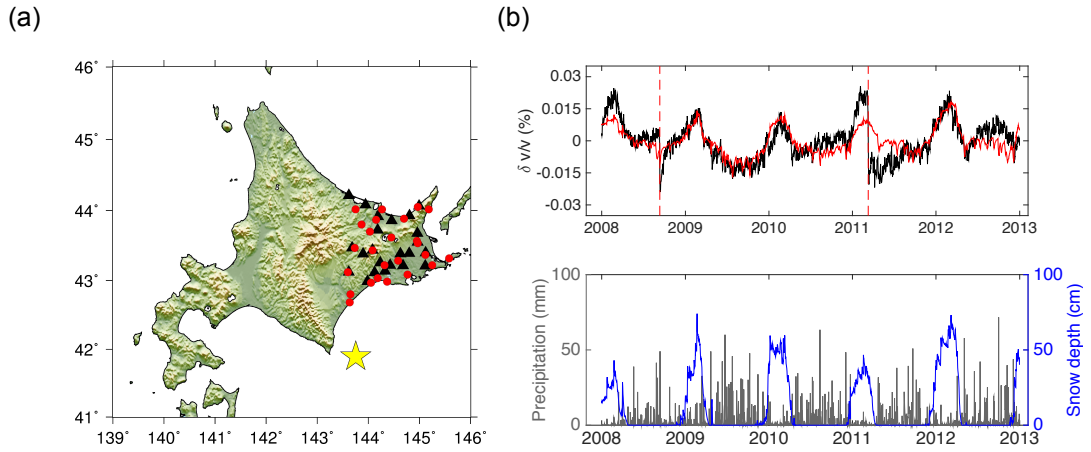

FIGURE 4.6 – (a) Map of the 23 Hi-net seismic stations (black triangles) and the 26 meteorological stations (red points) in Hokkaido. (b) Upper record : Mean seismic $\delta v/v$ over the 23 Hi-net stations (black curve), and the estimated velocity change time series (red curve) from the effects of pore pressure changes from both rainfall and snow depth. The dashed red lines indicate the days of Tokachi-Oki earthquake and Tohoku-Oki earthquake, from left to right. Lower record : Mean daily snow depth (cm), and mean daily precipitation (mm).

positively correlated, respectively, with the seismic $\delta v/v$, as we expected. A special geological condition in eastern Hokkaido which is covered by the Kushiro marsh, the largest marsh in Japan (Nakamura *et al.*, 2004), might enhance the response of seismic $\delta v/v$ by pore pressure changes.

4.4.3.3 Western Hokkaido and Honshu

The map of seasonality strength (Figure 4.2) indicates that the Sea of Japan side of Honshu and Hokkaido also shows significant seasonal effects. The seismic $\delta v/v$ time series of 92 Hi-net stations which show high (>0.6) seasonality strength (Figure 7a, b) show rapid velocity decreases due to the Tohoku-Oki earthquake. They also show relative velocity decreases in winter and increases in summer, except for some stations in the Japanese Alps in central Honshu and in the Kanto region (Figure 4.2a). These stations are at around $138°E$ and $140°E$, and they mainly show ephemeral decreases in velocity in summer.

Seasonal effects in the Japanese Alps can be explained well by precipitation-induced pore pressure changes. Figure 4.8a shows the mean precipitation and the mean pore pres-

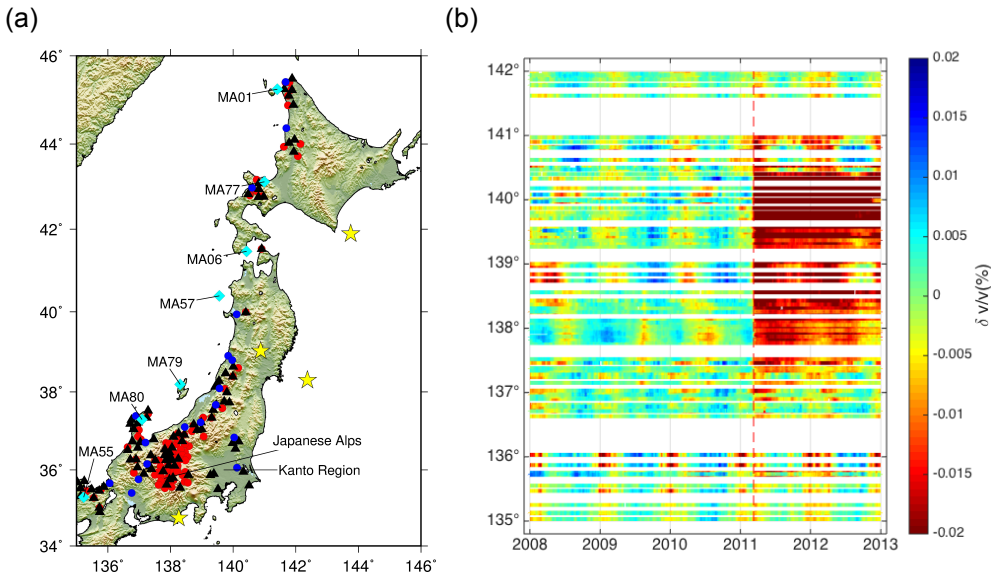

FIGURE 4.7 – (a) Map of the 92 Hi-net seismic stations (black triangles) with seasonality strength > 0.6. The red points indicate the meteorological stations that record the daily precipitation and daily maximum snow depth. The cyan diamonds indicate the seven tidal gauge stations. The 18 blue points indicate the meteorological stations that record the daily mean atmospheric temperatures.(b) Relative seismic $\delta v/v$ along the longitude from $135°E$ to $142°E$. The dashed red line indicates the day of the Tohoku-Oki earthquake.

sure changes calculated using equation 4.2. There is close correlation between the curves of the synthetic $\frac{\delta v}{v}_{syn}$ (Figure 4.8b, red) and the mean seismic measurement (Figure 4.8b, black).

The other areas except stations in the Japanese Alps or Kanto region (Figure 4.7a) also show repetitive but weak seasonal variations (Figure 4.9). In these areas, the mean daily snow depth is around 75 cm, and the mean daily precipitation is less than 25 mm. The overall tendency of the mean seismic $\delta v/v$ is to decrease in winter and increase in summer. This curve is out of phase with the mean seismic $\delta v/v$ in eastern Hokkaido, which is controlled by a combination of pore pressure changes and snow. Figure 4.9c shows that the precipitation-induced pore pressure changes do not correlate with the mean seismic $\delta v/v$. The seasonal effects in Hokkaido and Honshu along the Sea of Japan are almost independent of the pore pressure changes and the snow depth. Although the snowfall is much more intense on the western side, no clear associated velocity increases are observed ; instead velocities decrease during the period of intense snowfall. As the amplitudes (10^{-4}) of the seasonal effects in this area approaches the minimum detectable velocity changes that are theoretically expected with extreme changes in the noise

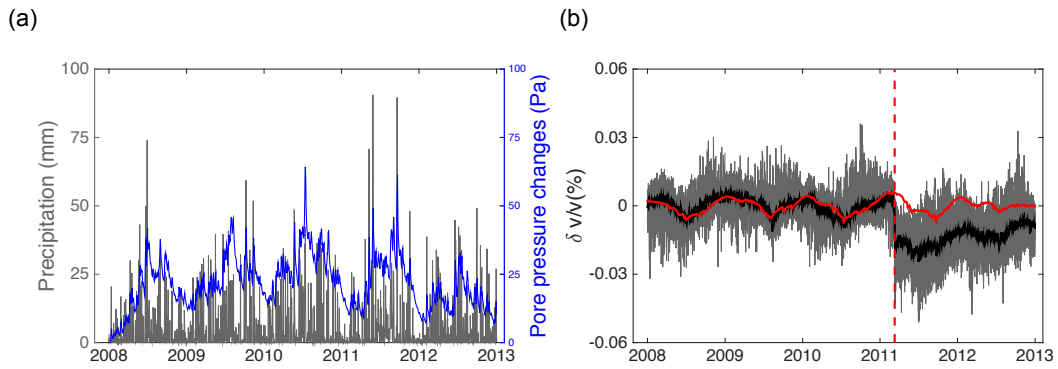

FIGURE 4.8 – (a) Mean daily precipitation (gray) in the Japanese Alps region and diffused pore pressure changes (blue). (b) Relative seismic $\delta v/v$ in the Japanese Alps region. The black curve represents the mean seismic $\delta v/v$. The red curve represents the synthetic $\frac{\delta v}{v}_{syn}$ from the pore pressure changes. The dashed red line indicates the day of the Tohoku-Oki earthquake.

wavefield (Colombi *et al.*, 2014), the observed $\delta v/v$ might be under the influence of noise source properties, also some other factors such as sea level fluctuation and thermoelastic stress changes might predominate the seasonal effects in this area.

The sea surface height is subjected to a variety of physical processes of meteorological (*e.g.*, atmospheric pressure, wind stress) and oceanographic (*e.g.*, surface currents) origins (Matsumoto *et al.*, 2006). It does not only provide information about the physical processes along the coast (Chelton et Enfield, 1986; Mitchum *et al.*, 2001), but it is also an important indicator of ocean mass variations (Matsumoto *et al.*, 2006). Ocean mass variations can change the ocean bottom pressure, as well as the stress acting on the seashore (**?**). The pressure can be different according to the types or directions of the pre-existing faults (Luttrell et Sandwell, 2010). Tide gauges measure the regional sea level changes, which are very consistent with the changes in sea surface height in Figure 4.9b. Altimetry data are provided by the National Oceanic and Atmospheric Administration Laboratory for Satellite Altimetry. Sea level data are usually used to improve the accuracy of altimetric data near the coasts (Morimoto *et al.*, 2000). Here, we consider the changes in sea level as the same as the changes in sea surface height. Figure 4.9b shows the mean $\delta v/v$ time series along the Sea of Japan compared to the mean changes in sea level from seven tidal gauge stations. The changes in seismic velocity and sea level correlate well with each other without any remarkable phase shift. Seismic velocity tends to increase when the sea level is high, and vice versa. Munekane (2009) also considered the seasonal load deformation due to ocean mass variations caused by nontidal factors

from the Sea of Japan for improved precision of GPS measurements. We thus assume here an instantaneous elastic ocean loading effect on the upper crust for Honshu and Hokkaido along the Sea of Japan.

Apart from the sea level, the nonuniform distribution of the air temperature in space and time, and the heterogeneity of the physical properties in the crust can generate thermoelastic stress (Berger, 1975; Ben-Zion et Leary, 1986). Given that the upper crust is characterized by both horizontal and vertical temperature gradients (Lubimova et Magnitzky, 1964), Meier *et al.* (2010), Tsai (2011), Richter *et al.* (2014), and Hillers *et al.* (2015a) attributed the seasonal seismic $\delta v/v$ mainly to the thermoelastic strain in some arid areas. Thus, we also compare the mean $\delta v/v$ with the mean temperature in the Sea of Japan side of Honshu and Hokkaido. There is a time delay of about 35 days between the time series of the atmospheric temperature changes and the seismic $\delta v/v$ before the Tohoku-Oki earthquake. The amount of delay is comparable with that inferred by Richter *et al.* (2014) for northern Chile, and a little smaller than the delay (around $40-45$ days) of Hillers *et al.* (2015a) for the San Jacinto fault, in an arid area. The time delay appears to be distorted by the earthquake, and the mean delay is about 64 days after the earthquake. The delay can be enhanced by the upper unconsolidated layer, which conducts heat but does not transfer stress (Berger, 1975; Ben-Zion et Leary, 1986). The strain changes at depth come from the temperature changes at the lower interface of the unconsolidated layer. Detailed comparison within time series of seismic $\delta v/v$, temperature and SL are in appendix B. Both temperature and SL have relatively high correlation with seismic δ v/v and all mutually correlated. We cannot exclude the effect from each of them. We choose in the following to use SL to reconstruct seasonal signals.

In western Hokkaido and Honshu, we studied the seasonal effects separately in the Japanese Alps and along the Sea of Japan. This confirms that the changes in the precipitation-induced pore pressure control the seasonal seismic $\delta v/v$ in the Japanese Alps. However, the seasonal effects are more complicated along the coast of the Sea of Japan. The time series of the mean seismic $\delta v/v$ does not correlate with the pore pressure changes or the snow depth. There is a good correlation between the seismic measurements and both the sea level and the atmospheric temperature recordings. As the atmospheric temperature does not differ in the two sides of the island, we do not consider that this factor is predominant in the Sea of Japan side, although there remain the potential effects from the thermoelasticity that is driven by the changes in tempe-

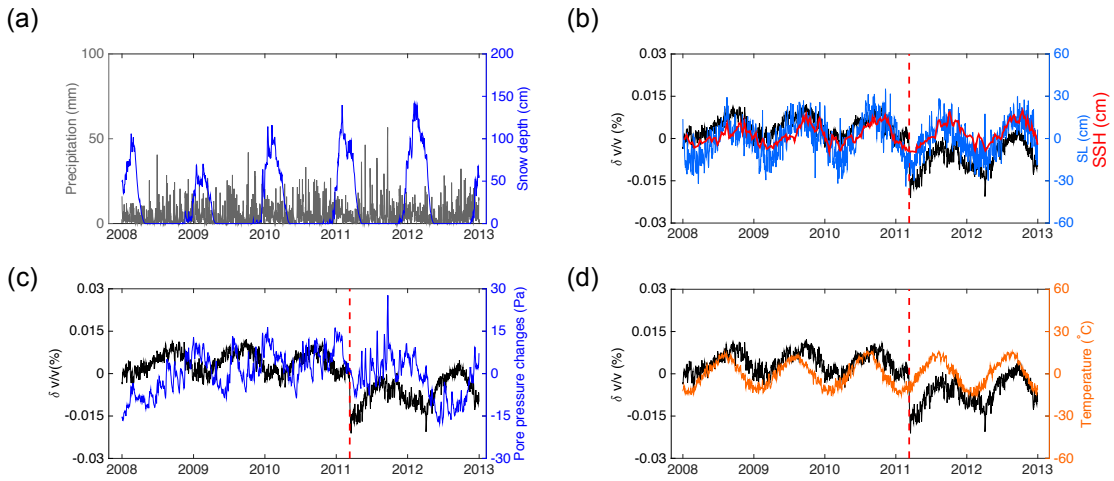

FIGURE 4.9 – (a) Mean daily precipitation and snow depth along the Sea of Japan. (b) Mean seismic $\delta v/v$ (black), mean sea level changes (light blue), and satellite altimetric heights (red). The mean seismic $\delta v/v$ is averaged over 58 Hi-net stations along the coast of the sea of Japan, without the central Japanese Alps. (c) Mean precipitation-induced pore pressure changes (blue) and the mean seismic $\delta v/v$ (black). (d) Mean seismic $\delta v/v$ (black) and the mean atmospheric temperature changes (orange). All of the dashed red lines indicate the day of the Tohoku-Oki earthquake.

rature. However, the changes in sea level can reflect the complicated physical processes in the coastal region, and these are consistent with the time series of the mean seismic $\delta v/v$.

4.5 Linear Model Correction

The previous paragraphs show that seasonal changes in the seismic velocities are controlled by rainfall-induced pore pressure changes, and in some regions by snow depth and sea surface height. Different regions of Japan show different sensitivities to these external perturbations. Thus we introduce a linear model of external perturbations, which is based on meteorological and oceanographic data, and used to create the synthetic seasonal velocity changes time series ($\frac{\delta v}{v}_{syn}$) for each Hi-net station.

$$\frac{\delta v}{v}_{syn} = a \cdot P + b \cdot S + d \cdot SL + C, \tag{4.6}$$

where a, b, and d are weighting coefficients for the time series of pore pressure changes

(P), snow depth (S), and sea-level changes (SL) from the closest meteorological and tide gauge stations of each Hi-net station, and C is a constant. The $\frac{\delta v}{v}_{syn}$ time series are obtained for each Hi-net station by fitting the time series of the observed $\delta v/v$ and adjusting a, b, d, and C.

The linear model is tested here by choosing three Hi-net stations with strong seasonality. Figure 4.10b-d shows the best fitting curves of $\frac{\delta v}{v}_{syn}$ and the residuals for these three stations. In the absence of a significant earthquake, the random fluctuations of the $\delta v/v$ time series after correction are reduced by about a factor of $1.5 - 2.5$, and down to the order of 10^{-5} (Table 4.1). The level of correction also depends on which station is chosen.

TABLE 4.1 – Standard deviations before and after correction

Station Name	Before	After
TREH	$1.21 * 10^{-4}$	$5.48 * 10^{-5}$
ARKH	$6.23 * 10^{-5}$	$3.99 * 10^{-5}$
UWEH	$4.91 * 10^{-5}$	$1.94 * 10^{-5}$

Figure 4.11 shows the quarterly seismic $\delta v/v$ before and after removing the $\delta v/v_{syn}$ time series for each Hi-net station from 2008 to 2010. The two anomalies in northeastern Hokkaido and Kyushu almost disappear. The spatially uniform coefficient of diffusivity, which is kept $1m^2/s$ in this study, might not be a good approximation, and might bring some instability. An anomaly remains in northeastern Honshu that is due to the co-seismic and post-seismic effects of the 2008 Iwate-Miyagi Nairiku earthquake. This thus shows that this correction procedure improves the extraction of the tectonic signal. In addition, some poor corrections might be due to some nonlinear relationships or changes in the characteristic coefficients of the crust before and after different earthquakes.

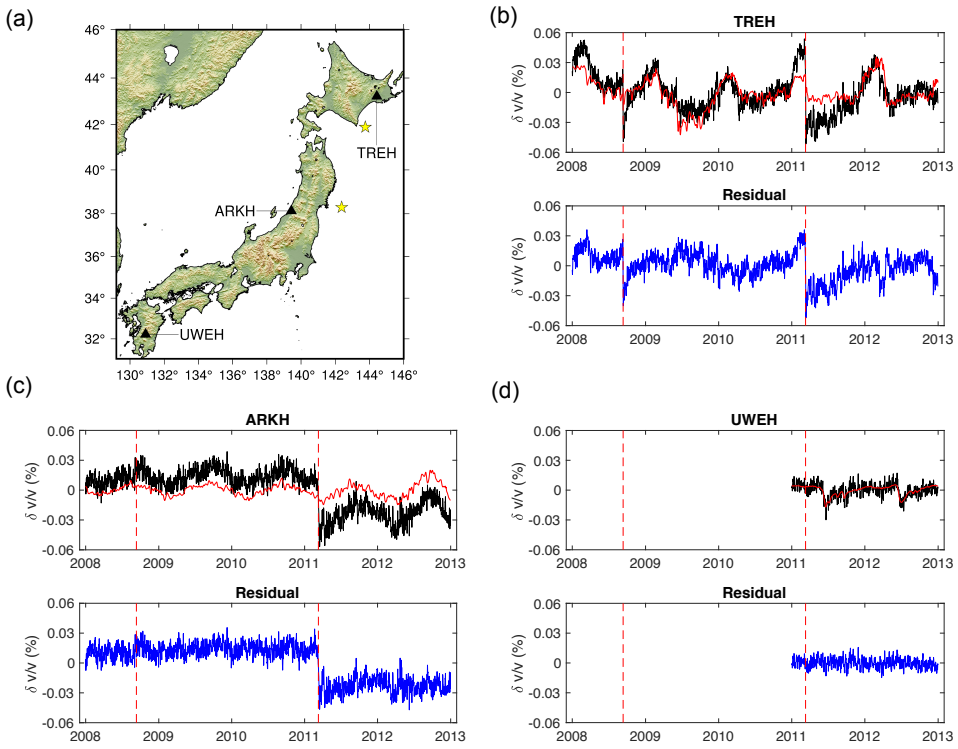

FIGURE 4.10 – (a) Locations of the three Hi-net stations (black triangles). (b-d) The black curve represents the seismic $\delta v/v$ at the different stations. The red curve represents the curve of the synthetic $\frac{\delta v}{v}_{syn}$ from the linear model, taking the meteorological and oceanographic data from the nearest weather and tide gauge stations. The blue curve represents the residual of the $\delta v/v$ after removing the red synthetic curve. The two dashed vertical lines indicate the day of the Tokachi-Oki earthquake (M_w 6.8) and the day of the Tohoku-Oki earthquake (M_w 9).

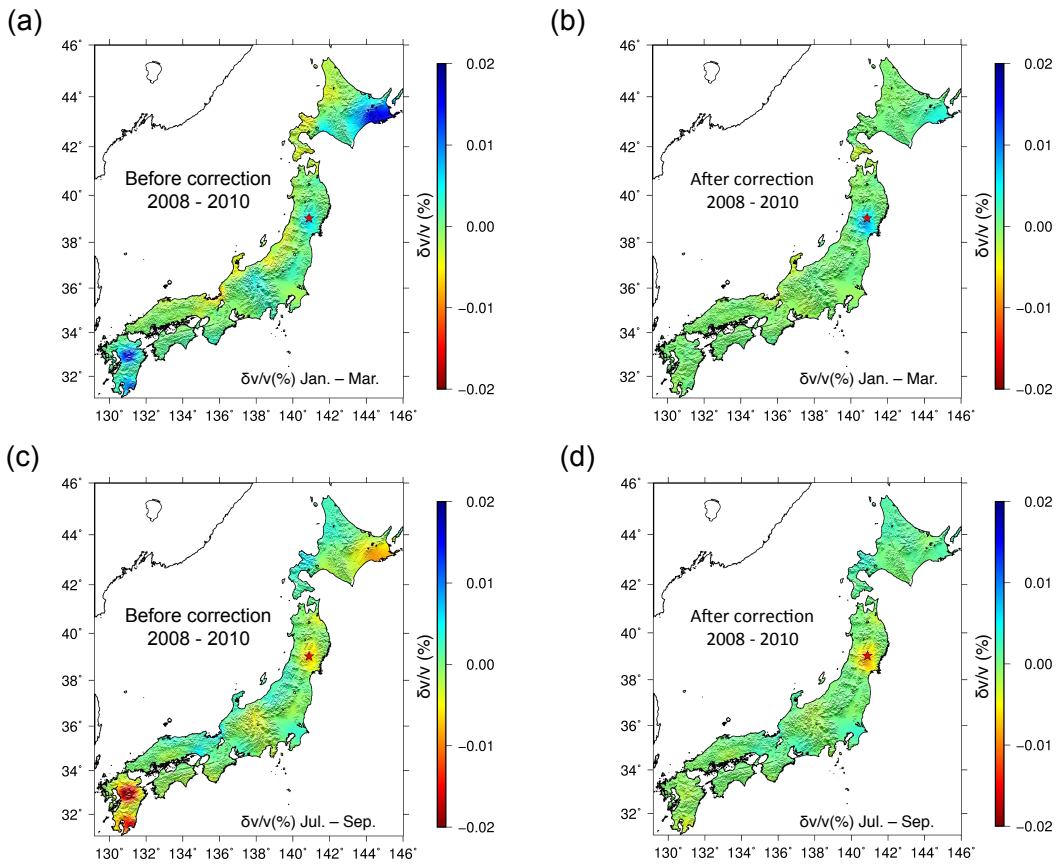

FIGURE 4.11 – Quarterly seismic $\delta v/v$ before and after the correction in Japan from 2008 to 2010. (a, b) Mean $\delta v/v$ before and after correction from January to March. (c-d) Mean $\delta v/v$ before and after correction from July to September. The red star indicates the epicenter of the Iwate-Miyagi Nairiku earthquake (M_w 6.9).

4.6 Discussion and Conclusion

Seismic velocity changes $\delta v/v$ over the whole Japan are measured using the doublet method applied to the coda wave part of the noise cross-correlation functions. They allow us to continuously track temporal changes of the mechanical properties of tectonic and nontectonic origin in the upper crust. In this study, we observe strong seasonal seismic $\delta v/v$ in addition to the sudden velocity drops that are coincident with different earthquakes. The seismic velocities show strong seasonality in Kyushu and Hokkaido, and along the Sea of Japan side of Honshu. Seasonal variations show complex and variable annual patterns in different areas. These differences depend mainly on the local geological conditions and external perturbations.

The quarterly seismic $\delta v/v$ show two large anomalies in Kyushu and in northeastern Hokkaido. The diffuse pore pressure changes induced by strong precipitation in monsoon seasons control the local seasonal effects in Kyushu. In addition, pronounced velocity decreases are identified in the volcanic regions, which are more sensitive to external stress changes due to the large amount of pre-existing microcracks and high fluid pressure. Both precipitation and snow depth affect velocity changes in eastern Hokkaido. Although the snow depth is positively correlated with seismic $\delta v/v$ in this area, the mechanisms that link $\delta v/v$ and snow depth are still unclear. Snow might increase the seismic velocity through a loading effect, by reducing the porosity and by enhancing the drainage in this special marsh area. However, neither pore pressure change nor snow depth can explain the seasonal seismic $\delta v/v$ in western Hokkaido, even though the snow depth is much greater along the western side of Japan.

Clear seasonal fluctuations also appear in western Honshu and Hokkaido. Yet, the seasonal changes of $\delta v/v$ are relatively weak. The Japanese Alps in central Honshu show strong seasonal effects that are explained by rainfall-induced pore pressure changes, as in Kyushu. Sea of Japan side of Honshu shows similar seasonal effects as in western Hokkaido, with velocity increases in summer and decreases in winter. The related mean seismic $\delta v/v$ time series have good correlation with changes in both sea level and atmospheric temperature. The changes in sea level can be linked to seismic velocity changes through a loading effect in the coastal regions.

Therefore, we propose a simple model to correct for the seasonal effects for each single station by taking the meteorological and oceanographic data from the nearby stations. The standard deviation of the $\delta v/v$ time series after correction is reduced to 10^{-5}. Time

series of seismic $\delta v/v$ after correction allow us to track small changes in the mechanical properties of the crust linked to tectonic effects. It should also be noted that these seasonal effects should be observed and verified using GPS deformation measurements. More analysis with dense GPS data needs to be carried out. We expect this comparative analysis to provide a better model of the correction of seasonal effects, leading to a more precise estimation of seismic $\delta v/v$ of tectonic origin.

4.7 Appendix

4.7.1 A1 : Comparison with GRACE

Gravity Recovery And Climate Experiment (GRACE) monitors the gravity field and is sensitive to detect the total water storage, which is represented as equivalent water heights (EWH, cm). In this study, we use the EWH 10-day and monthly solutions RL03-v3, courtesy of CNES/GRGS. The time-variable GRACE data after preprocessing mainly reflect the gravitational changes from hydrology, snow cover, baroclinic oceanic signals and post-glacial rebound. The reference field of EWH grids is a static mean field, which is close to the actual value of the Earth's gravity field on the first day of 2008.

Quarterly variations of EWH (Figure 4.12) are mapped using monthly solutions RL03-v3 with spatial resolution of 1 deg^2 in the same periods as Figure 4.3. In Kyushu, it is clear that EWH is dominated by the high rainfall in the third quarter as in Figure 4.3c. Besides, we can observe that the positive EWH in the eastern corner of Hokkaido in the first quarter is due to the snow fall in winter and corresponds to the increase of seismic velocity. There are more complicated process occurred in the central Japan, which may relate to the ocean in both sides.

In addition to the quarterly comparison of the spatial characteristics of EWH and seismic $\delta v/v$, we also use single point extraction to get 10-day time series of EWH in different locations. The single point data comes from barycentric computation from the values at the 4 surrounding grid points with surface area of 1 deg^2. All the time series are demeaned. There are 12 missing values during the period from 2008 to 2012. We observe in Figure 4.13 that EWH are positive or negative correlated with seismic $\delta v/v$ in different locations. The sensitivities of variations of EWH to $\delta v/v$ are all comparable.

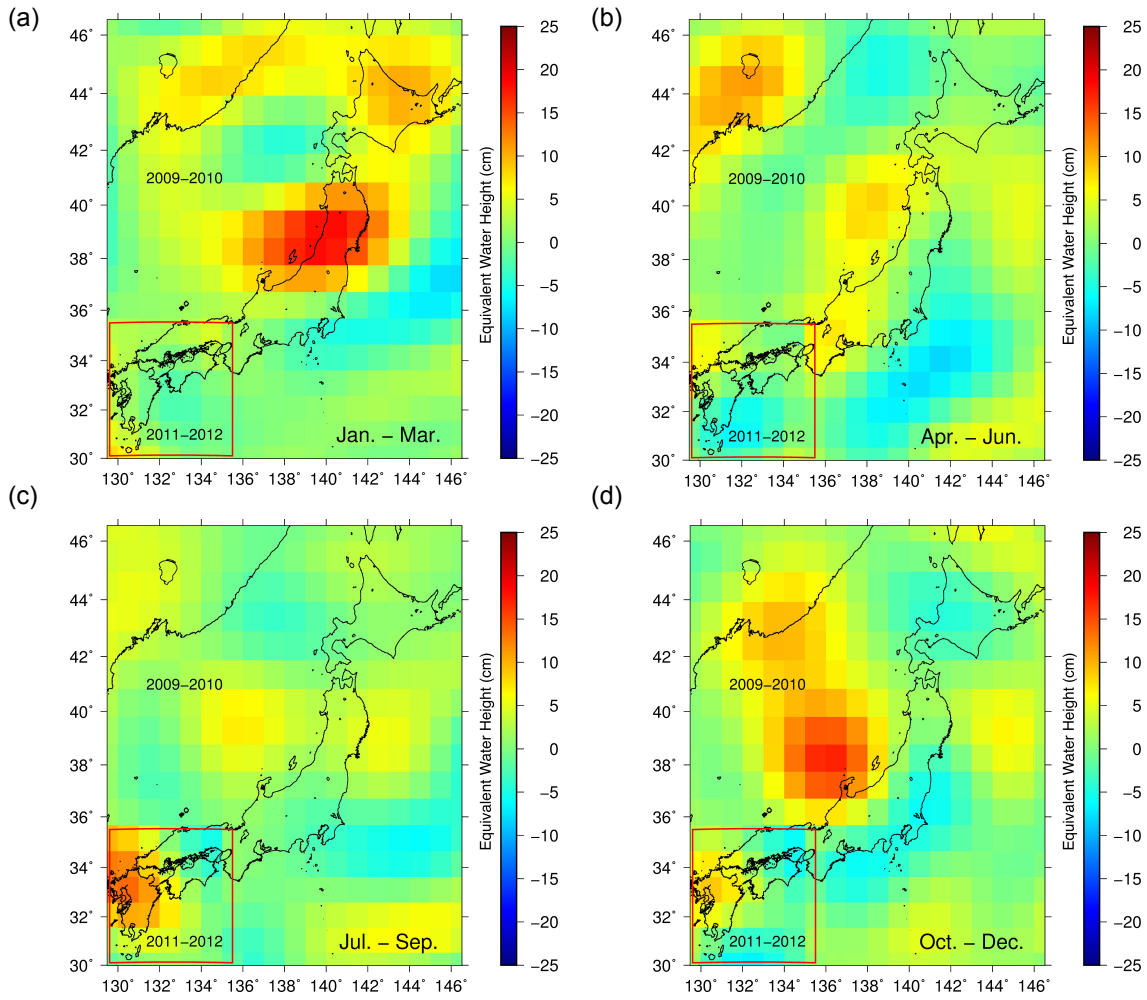

FIGURE 4.12 – Quarterly variation of EWH (cm) during the same period as seismic data (N : 2009-2010 ; S : 2011-2012). (a) Jan. - Mar. (b) Apr. - Jun. (c) Jul. - Sep. (d) Oct. - Dec.

4.7.2 A2 : Time shift measurement

We analyze the correlation of mean seismic $\delta v/v$ in the western Hokkaido and Honshu with mean variations of atmospheric temperature and SL. The three time series are shown in Figure 4.14a. Figure 4.14b is the correlation matrix within $\delta v/v$, temperature, and SL. Time shift between $\delta v/v$ and each other two time series is calculated using a one year moving window. The time shift results are shown in figure 4.14c. Seismic $\delta v/v$ is posterior to changes of atmospheric temperature. The mean delay is $\sim$ 35 days. However the time shift between SL and $\delta v/v$ is small and $\sim$ 8 days.

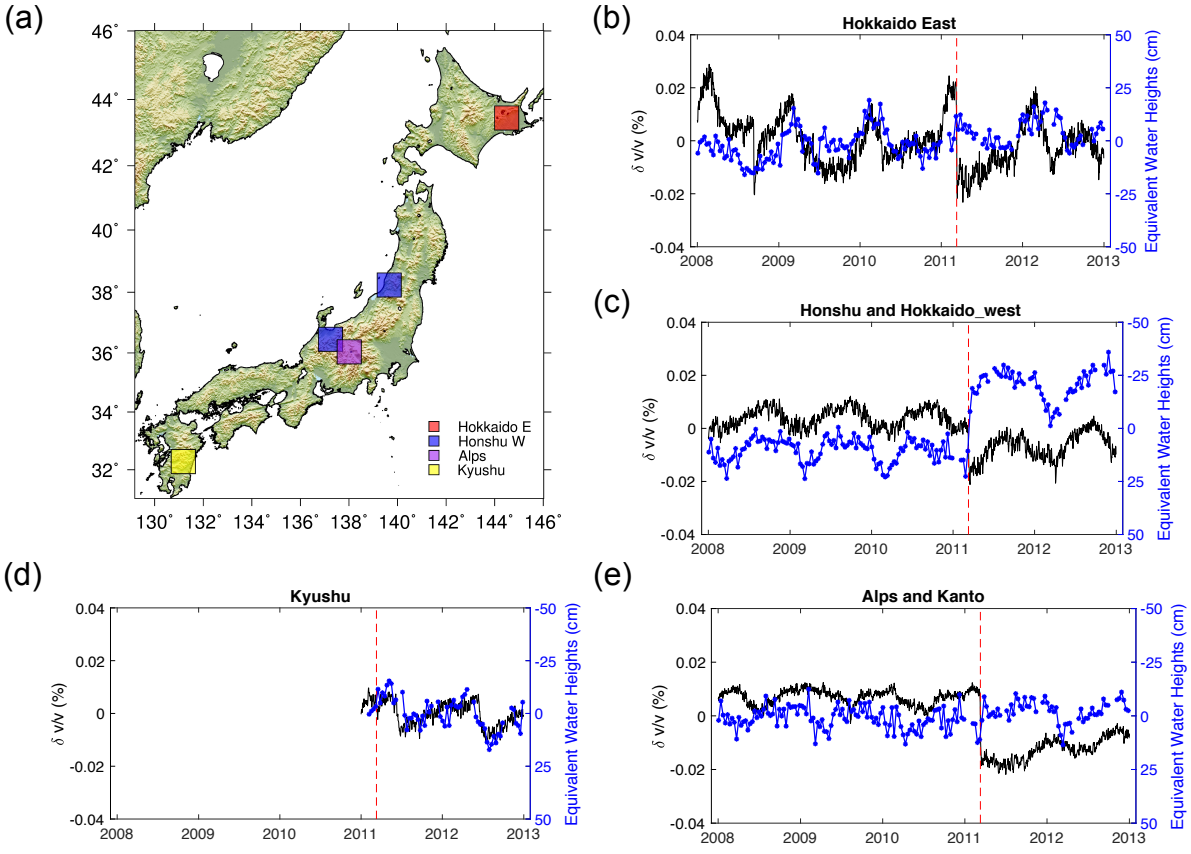

FIGURE 4.13 – The four different color indicates areas where the GRACE data is selected. (b)-(e) show the seismic $\delta v/v$ (black) and EWH (cm, blue) in different areas. (b) is positively correlated to the EWH. The positive EWH is upwards plotted. (c), (d) and (e) are negatively correlated to the EWH. The positive EWH is downwards plotted.

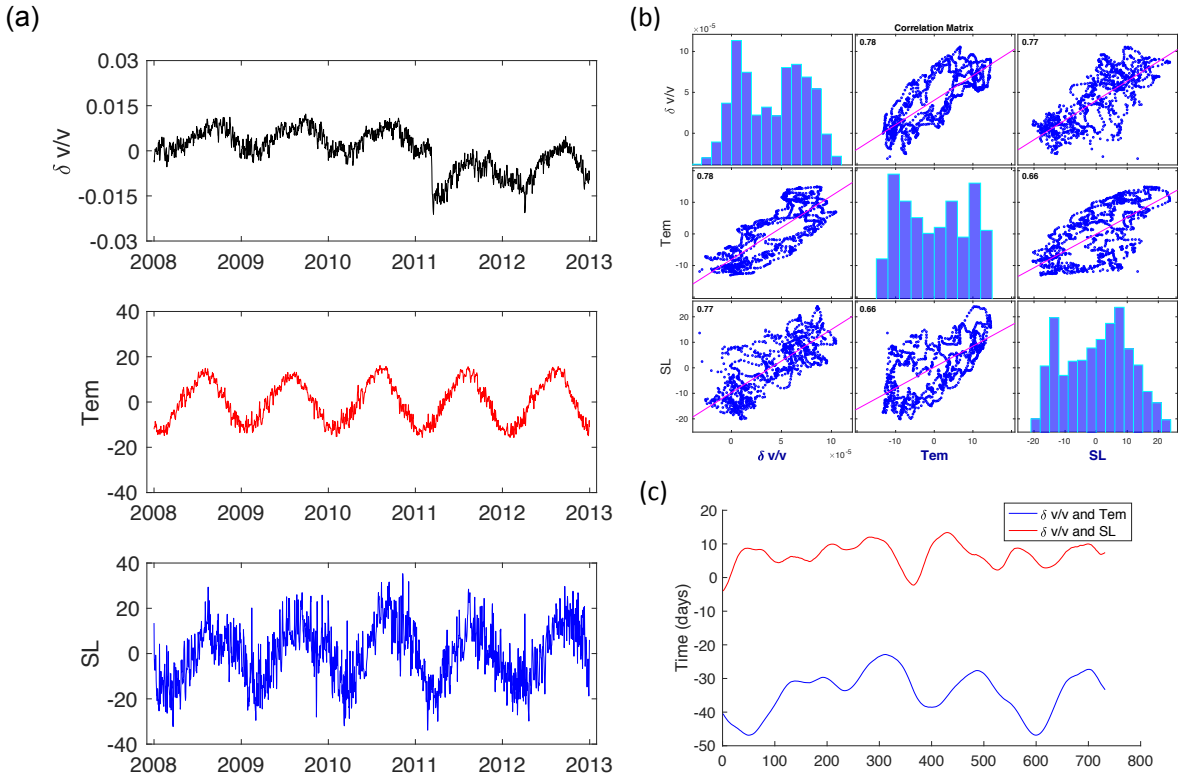

FIGURE 4.14 – (a) shows variations of $\delta v/v$, temperature, and SL (top to bottom). (b) is a correlation matrix within time series of $\delta v/v$, temperature, and SL. (c) is the time shift (days) between $\delta v/v$ and all other variations in (a).

4.8 Statistical Analysis of the Seismic Velocity Changes

In this section, we do some statistical analysis of the seismic velocity changes according to a procedure which was proposed by Hisashi Nakahara from Tohoku University. He suggested to analyze our data to investigate the underlying statistical probabilities of velocity changes in absence of big earthquake. We choose two time periods of two years from 2009 to 2010 in the north and from 2011 to 2012 in the south to run the statistical analysis. We selected four seismic stations BKEH, AAKH, MKOH, and UWEH (Fig. 4.15) in regions with strong seasonal variations to analyze their probability distributions and compare the statistical probabilities before and after correcting the seasonal signals.

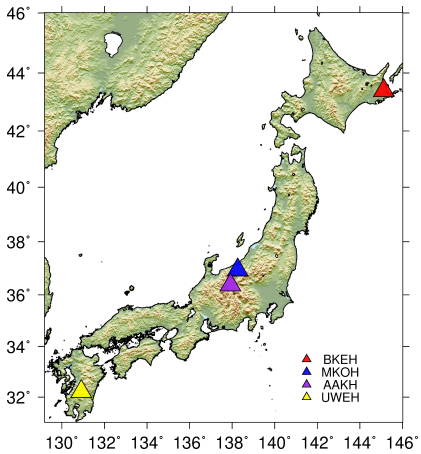

FIGURE 4.15 – Locations of stations BKEH, AAKH, MKOH, and UWEH.

Fig. 4.16 and Fig. 4.17 display the results of probability density and Q–Q (quantile-quantile) plot at four stations. The time series of seismic velocity changes have been centered to have a zero mean and rearranged in ascending order. Linearity of Q-Q plot is a mark of Gaussianity. For results before correction, we observe the probability density plots are showing deviations from the Gaussian distributions. Q–Q plots are only almost linear and are not symmetric. For results after correction, the probability density distributions are more consistent with Gaussian distribution and Q-Q plots produce some approximately straight line. Both evidences suggest that the seismic velocity changes during the period without big earthquake follow approximately a normal distribution. Besides, we can clearly observe that the corrected results are more consistent with the Gaussian distribution. This indicates that the deterministic signals due to external forcing have been effectively removed. The remaining fluctuations appear as random Gaussian noise and adhoc techniques, as averaging, are justified to weaken the short term fluctuations.

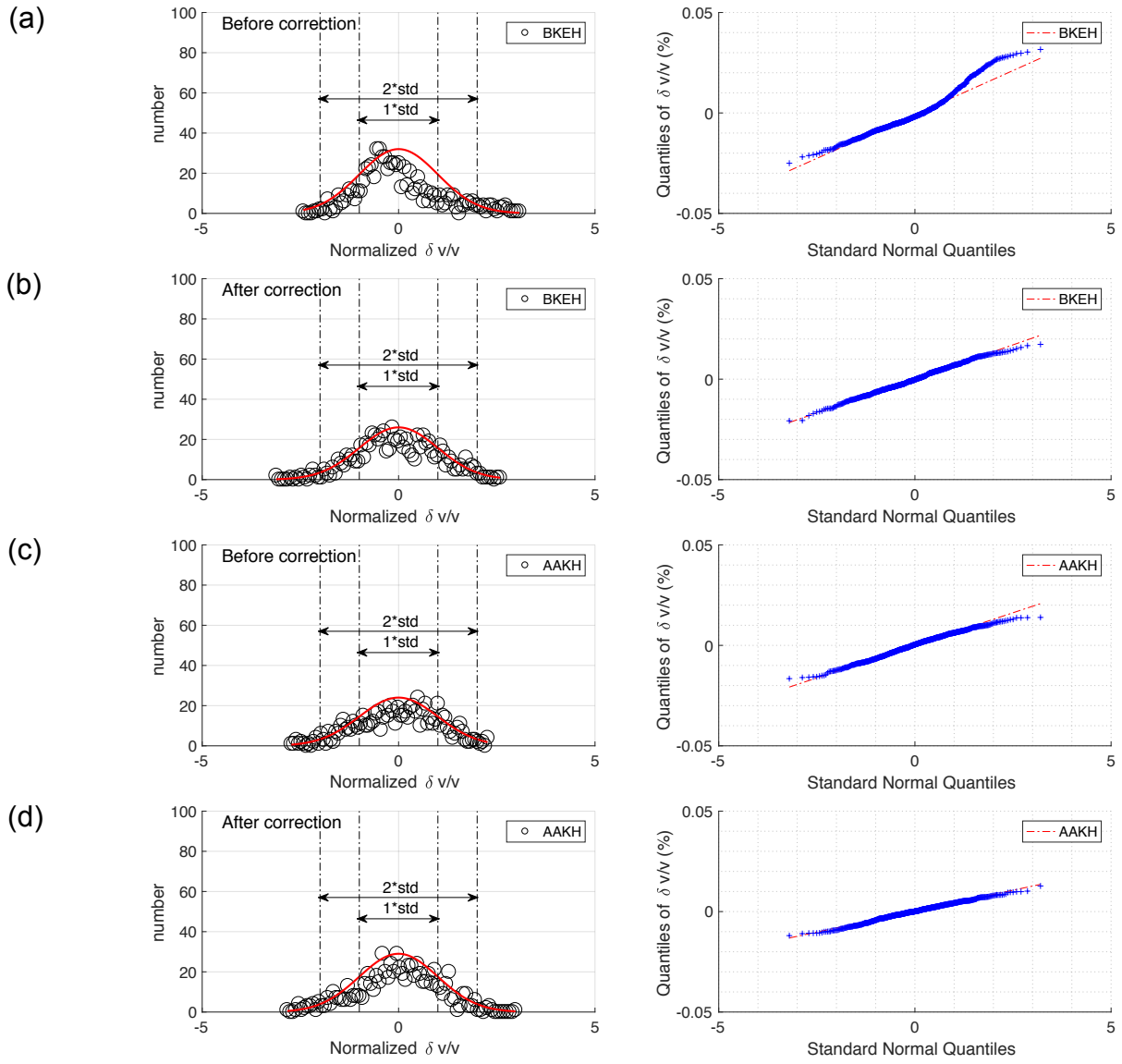

FIGURE 4.16 – (a) - (d) show the statistical analysis at station BKEH and AAKH using seismic velocity changes before and after correcting the seasonal effects (continued on next page).

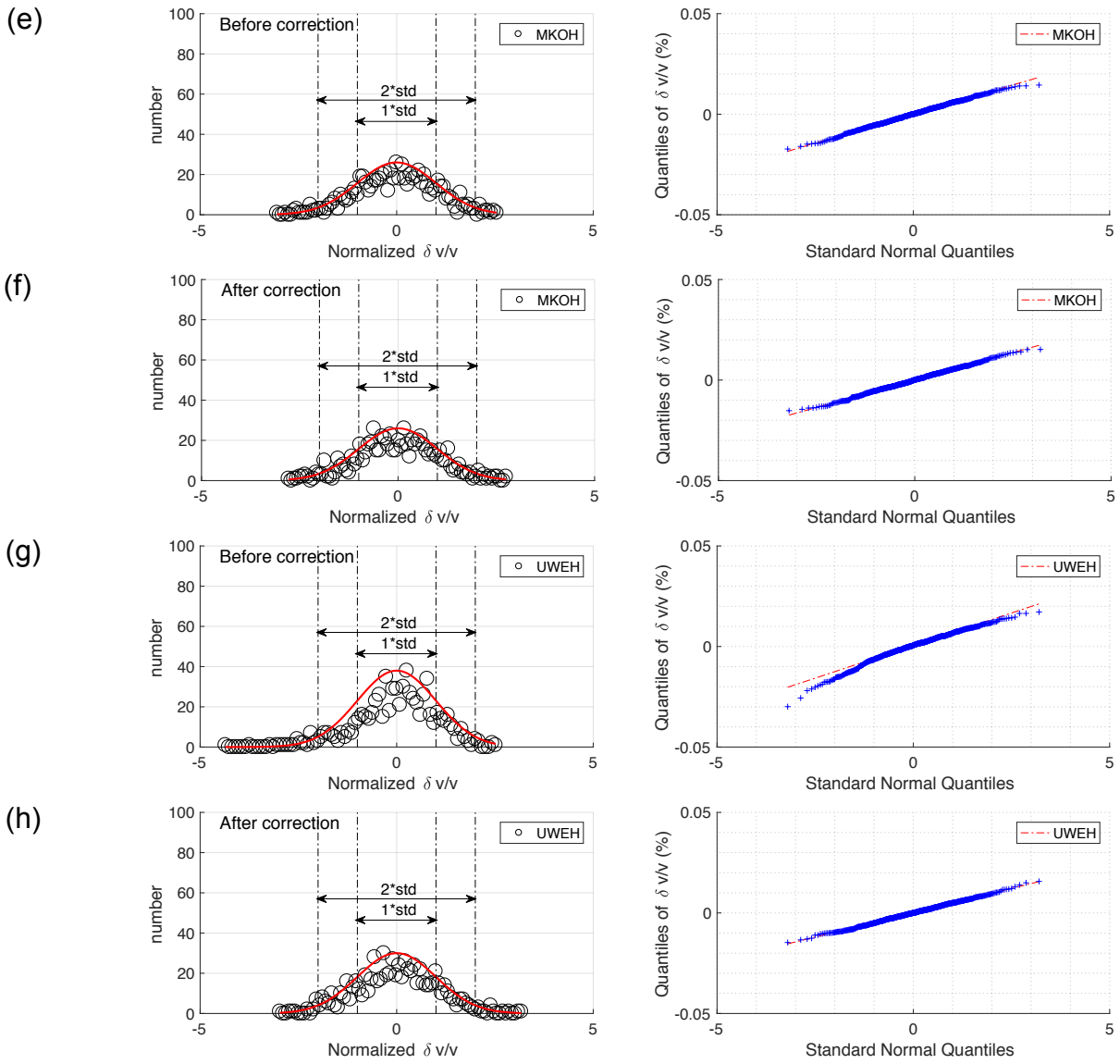

FIGURE 4.17 – (e) - (h) show the statistical analysis at station MKOH and UWEH using seismic velocity changes before and after correcting the seasonal effects (continued from previous page)

Chapitre 5

Comparison of Seasonal Velocity Changes with Geodetic Observations

Sommaire

5.1 Introduction of GPS Data 82

5.2 Comparison between GPS Vertical Displacement and Seismic Velocity Changes 83

5.2.1 Kyushu 84

5.2.2 Japanese Alps 85

5.2.3 Eastern Hokkaido 86

5.2.4 Western Coastal Side of Hokkaido and Honshu 87

5.3 Comparison with Observations by GRACE 88

5.4 Discussion and Conclusion 90

We systemically study the seasonal seismic velocity changes in the crust throughout Japan in the Chapter 4. The global comparison between seasonal seismic changes and GRACE satellite measured gravity field (equivalent water height, EWH) shows strong consistency. Besides, some local seasonal signals and the adjacent EWH are very correlated with each other. For the regions with strong seasonality, Except in Hokkaido seismic velocity changes and EWH are positively correlated. For other regions, such as Kyushu, central Alpes, western coastal side of Honshu are all negatively correlated with EWH. Especially in Kyushu, not only the seasonal seismic velocity changes are in agreement with the EWH, but also the long-term trend. However, as both spatial and temporal resolution of GRACE is low, we need GPS observations to make more accurate local

comparisons. In this Chapter, we compare the time series of seasonal seismic velocity changes with both GPS recorded vertical displacement and GRACE measured gravity field to further study the seasonal effects throughout Japan.

5.1 Introduction of GPS Data

Japan operates a dense continuous Global Positioning System (GPS) network, known as GEONET since 1994 for providing geodetic positioning to monitor crustal deformation in Japan. In this study, we make use of 1218 GEONET stations with three components recordings from 2008 to 2012 Fig. 5.1. The average inter-station distance is around 25 – 30 km. Data preprocessing corrects the effects from solid earth tide, pole tides, and ocean tidal loading using GAMIT software (Herring *et al.*, 2010) at ISTerre. In this chapter, we mainly discuss the time series of vertical displacements and their comparison with the measured crustal seismic velocity changes in the frequency band 0.15 – 0.90 Hz.

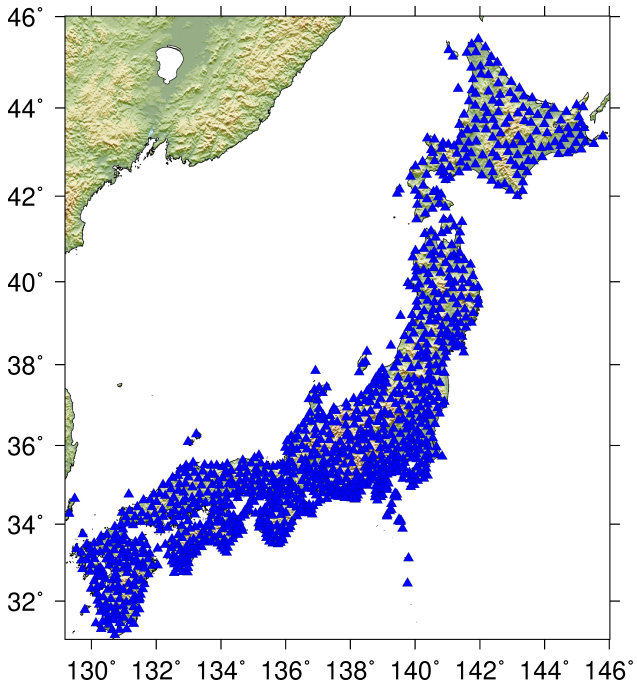

FIGURE 5.1 – Distribution of GPS stations (blue triangle) used in this study.

Daily displacements of three components yield abundant information about crustal deformation in Japan. Many complex processes do not relate to tectonic deformation and emerge from seasonal variations. These seasonal signals are affected by changes in

environmental factors also seen on seismic velocity changes. Many studies have been carried out on the topic of the origin of seasonal displacements measured from GPS. Most of the observed seasonal fluctuations on vertical motions are attributed to loading and poroelastic responses induced by changes of the ground water table (Bawden *et al.*, 2001; Watson *et al.*, 2002; Tiwari *et al.*, 2014; Khandelwal *et al.*, 2014). The large vertical displacement has been demonstrated to be well correlated to elastic deformation computed from hydrological data at a site in the central Amazon Basin by Bevis *et al.* (2005). Both hydrology and thermoelastic induced stresses and strains have also been confirmed by Tsai (2011) in southern California. In Japan, Heki (2003, 2004, 2007) analyzes different possible processes for seasonally varying environmental displacements, emphasize the important contribution of snow loads, and conclude that the spring thaw may enhance the seismic activities beneath the snow cover. The dense distributed GPS offer us the opportunity to understand regional-dependent seasonal crustal seismic velocity changes better.

5.2 Comparison between GPS Vertical Displacement and Seismic Velocity Changes

Firstly, we recall the map of the distribution of seasonal effects throughout Japan from the last chapter. The figure below (Fig. 5.2) shows the seasonality strength of which the value is the correlation coefficients between any two annual signals within different years. We see that the eastern corner of Hokkaido, the total Kyushu, the central Alps region, and the western coastal side of both Honshu and Hokkaido show strong seasonal effects (Wang *et al.*, 2017). So we will select several seismic stations in this regions and compare the time series of seismic velocity changes with the nearby GPS vertical displacement.

We select several Hi-net stations in different locations where there are strong seasonal effects as shown in Fig. 5.2. Centered on these seismic sites, we search for all the GPS vertical displacement measurements with a radius of 30 km. Then we compare the Hi-net seismic velocity changes with the averaged vertical displacements within this range. So we analyze the relevance between the seismic velocity changes and GPS vertical displacement by subregion.

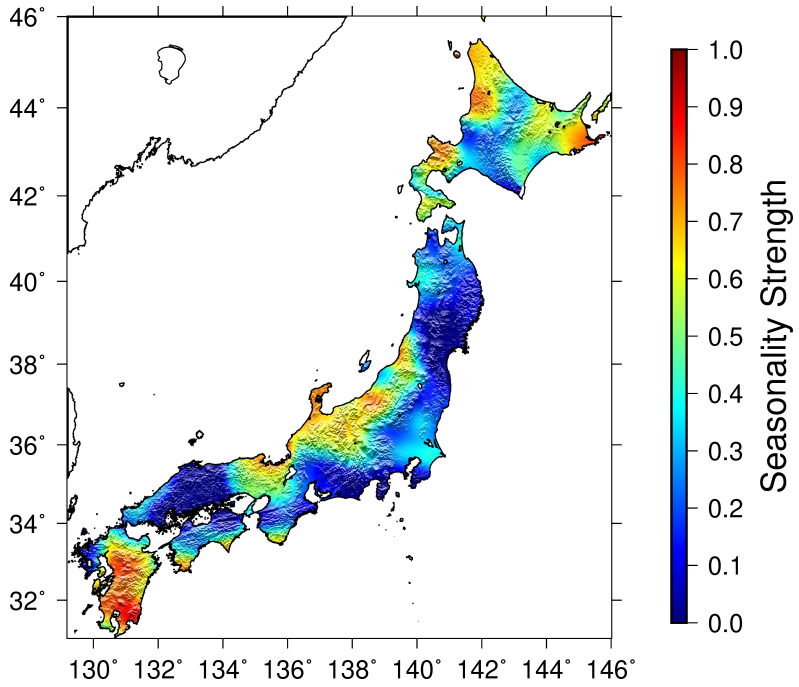

FIGURE 5.2 – Map of the seasonality strength of the annual seismic velocity changes in 0.15 - 0.9 Hz.(Wang *et al.*, 2017)

5.2.1 Kyushu

In Kyushu, seismic velocity changes are measured from 2011 to 2012. We identify the dominant environmental factor responsible for the seasonal seismic velocity changes is the intense precipitation induced pore pressure changes, especially in summer (Wang *et al.*, 2017). We choose two seismic stations and compare the seismic velocity changes with all GPS vertical displacements within a distance of 30 km. The amplitudes of seasonal seismic velocity changes are about $10^{-2}(\%)$. The sensitivity of seismic velocity changes to GPS height is $10^{-2}(m^{-1})$ for both stations.

The two stations are TAKH and UWEH (Fig. 5.3 (a)), and there are 8 and 6 GPS stations within 30 km, respectively. Both stations are located in the region where the seismic seasonal effect is substantial. By contrast, we can clearly see in Fig. 5.3 (b) and (c) that there is a positive correlation between the seismic velocity changes and GPS vertical motion for both stations and especially for the first year in 2011. When the seismic velocity decreases subjected to the precipitation induced pore pressure changes, the GPS height also decreases rapidly. Instead of this, GPS height decreases slowly with time. Especially for station UWEH, during the period when velocity decreases

suddenly in each July, the GPS height does not change as sharply as changes of seismic velocity. It shows when the precipitation is strong GPS vertical component tends to move downwards with a relatively slow response compared to the seismic response due to the precipitation. In this region, GPS height may be more sensitive to the water loading effect induced subsidence on the crust. However seismic velocity changes are more sensitive to the precipitation induced pore pressure changes. it is also worth noting that apart from the instantaneous response to precipitation, the two-year trend of both seismic velocity changes and GPS height are identical at the two stations.

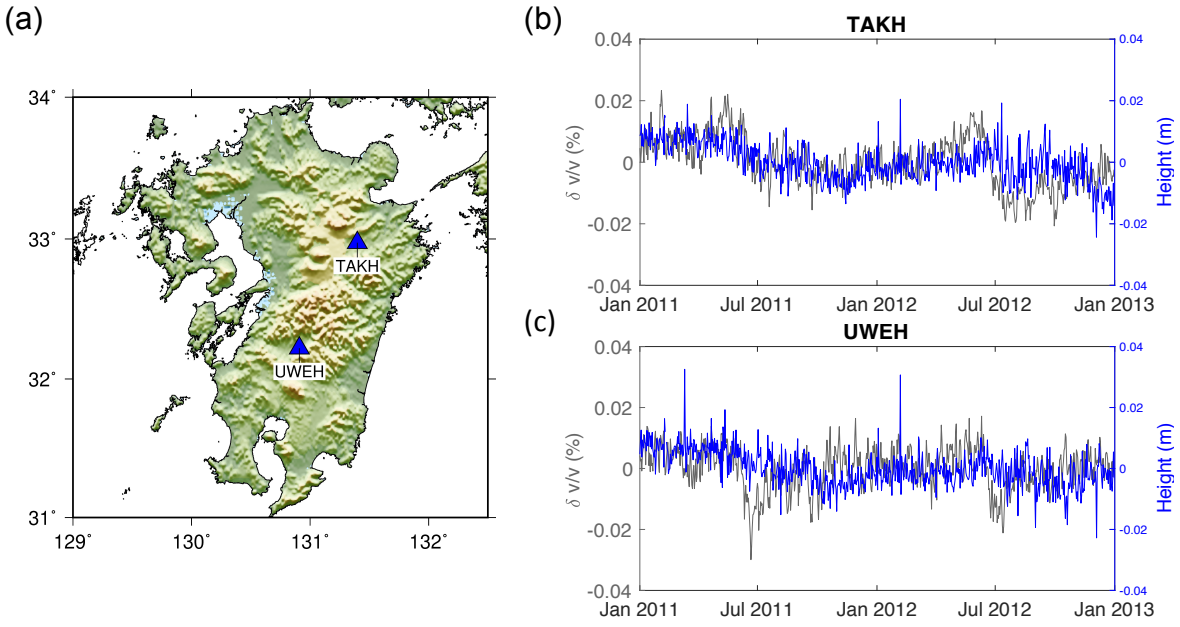

FIGURE 5.3 – (a) Locations of Hi-net seismic station TAKH and UWEH in Kyushu. (b) and (c) are the comparison between time series of seismic velocity changes (black curve) at TAKH and UWEH and the averaged nearby GPS vertical displacements (blue curve).

5.2.2 Japanese Alps

In the Japanese Alps region, seismic velocity changes are measured from 2008 to 2012. It has also been shown that the local seismic velocity changes are controlled mainly by the precipitation induced pore pressure changes as in Kyushu (Wang *et al.*, 2017). We show the seismic velocity changes at Hi-net station AAKH and around which there are 6 GPS stations within the distance of 30 km (Fig. 5.4). The sensitivity of seismic velocity changes to GPS height, which is the ratio of velocity changes to vertical displacement,

is $10^{-2}(m^{-1})$ the same as in Kyushu.

The contrast of seismic velocity changes and GPS height shows that they are negatively correlated, even for the two years after the Tohoku-oki earthquake. Except that the seismic response to the big earthquake is the decrease of velocity due to the instantaneous dynamic stress changes. However, GPS height increases along with the uplift of the crust and continues to rise in this area. In comparison to the Kyushu area case, GPS vertical component moves upwards when seismic velocity decreases due to the changes of pore pressure generated by precipitation. This difference may indicate that in this region the GPS vertical displacements are controlled by poroelasticity induced deformation as observed by Johnson *et al.* (2017).

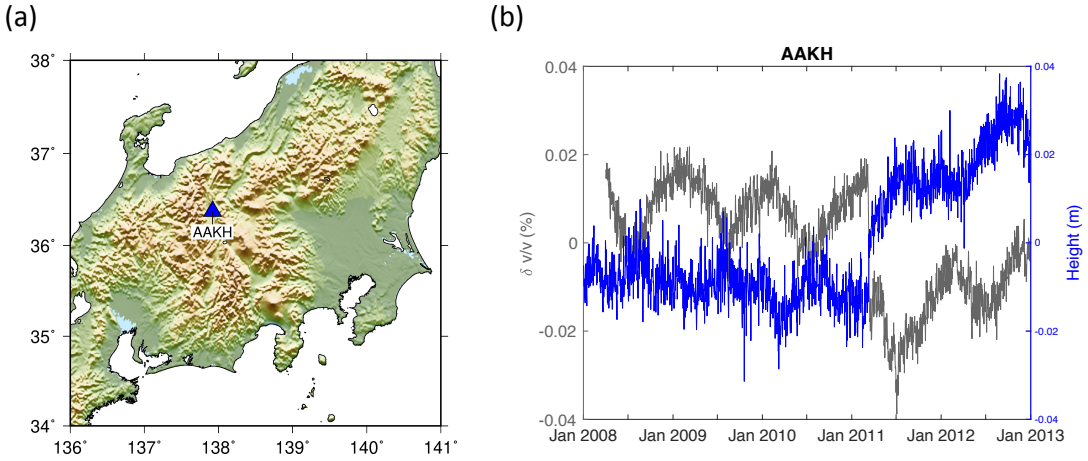

FIGURE 5.4 – (a) Locations of Hi-net seismic station AAKH in the Japanese Alps region. (b) is the comparison between time series of seismic velocity changes (black curve) at AAKH and the averaged nearby GPS vertical displacements (blue curve).

5.2.3 Eastern Hokkaido

In the eastern corner of Hokkaido, we observe seasonal seismic velocity changes with strong velocity increase in winter. We select the Hi-net seismic station BKEH (Fig. 5.5). The GPS height is averaged over 7 nearby stations. The seasonal signal in this region is controlled by both effects of increased pore pressure during precipitation in summer (velocity decrease) and of closure of crustal cracks in winter (velocity increase) affected by both snow loading and pore pressure decrease by water drainage (Wang *et al.*, 2017).

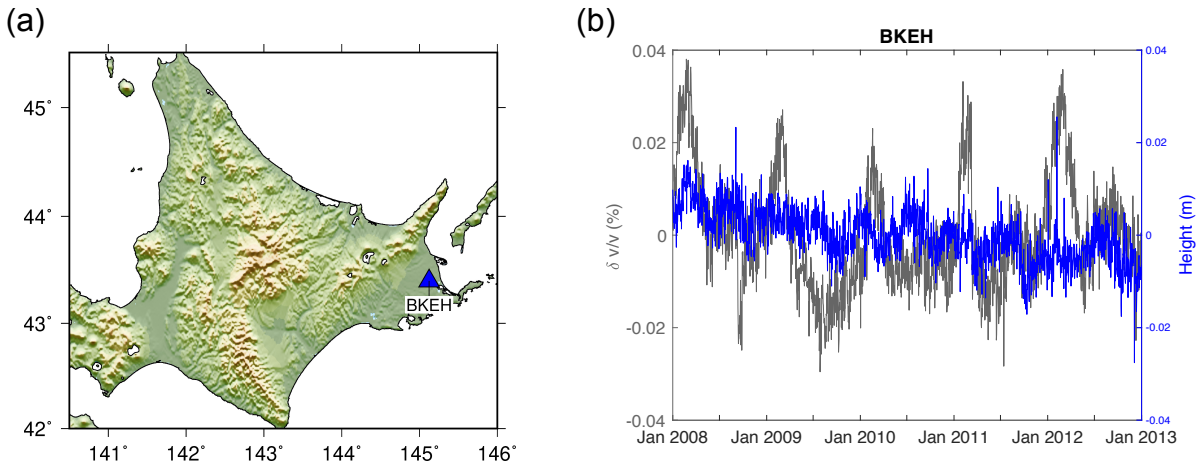

FIGURE 5.5 – (a) Locations of Hi-net seismic station BKEH in Hokkaido. (b) is the comparison between time series of seismic velocity changes (black curve) at BKEH and the averaged nearby 7 GPS vertical displacements (blue curve).

From the comparison with GPS height, we do not observe the clear seasonal pattern on GPS height. The snow effect is not clear from the GPS observation. Conversely, the five-years downward long-term changes in GPS height has an overall downward trend, which could be related to the positive changes in seismic velocity.

5.2.4 Western Coastal Side of Hokkaido and Honshu

Seismic velocity changes in the western coastal region of Hokkaido and Honshu show strong seasonal effects with annual harmonic changes, which are considered to be affected by the loading effect from the changes of sea surface height of the sea of Japan (Wang *et al.*, 2017). We select two stations (BFWH and MKOH in Hokkaido and Honshu, respectively) to compare with the nearby GPS vertical displacements. There are separately 7 and 6 GPS stations within the distance of 30 km. Likewise, the sensitivity of seismic velocity changes to GPS height is $10^{-2}(m^{-1})$ for both stations.

Time series of seismic velocity changes and GPS height are well in phase and positively correlated (Fig. 5.6 (b) and (c)). This appearance is identical with the conclusion by Williams et Penna (2011) that the non-tidal oceanic loading changes act on the GPS height time series in the coastal sites. The seasonality of vertical motion and δv/v along the coast is due to the elastic response of the upper crust under the effect of the variations

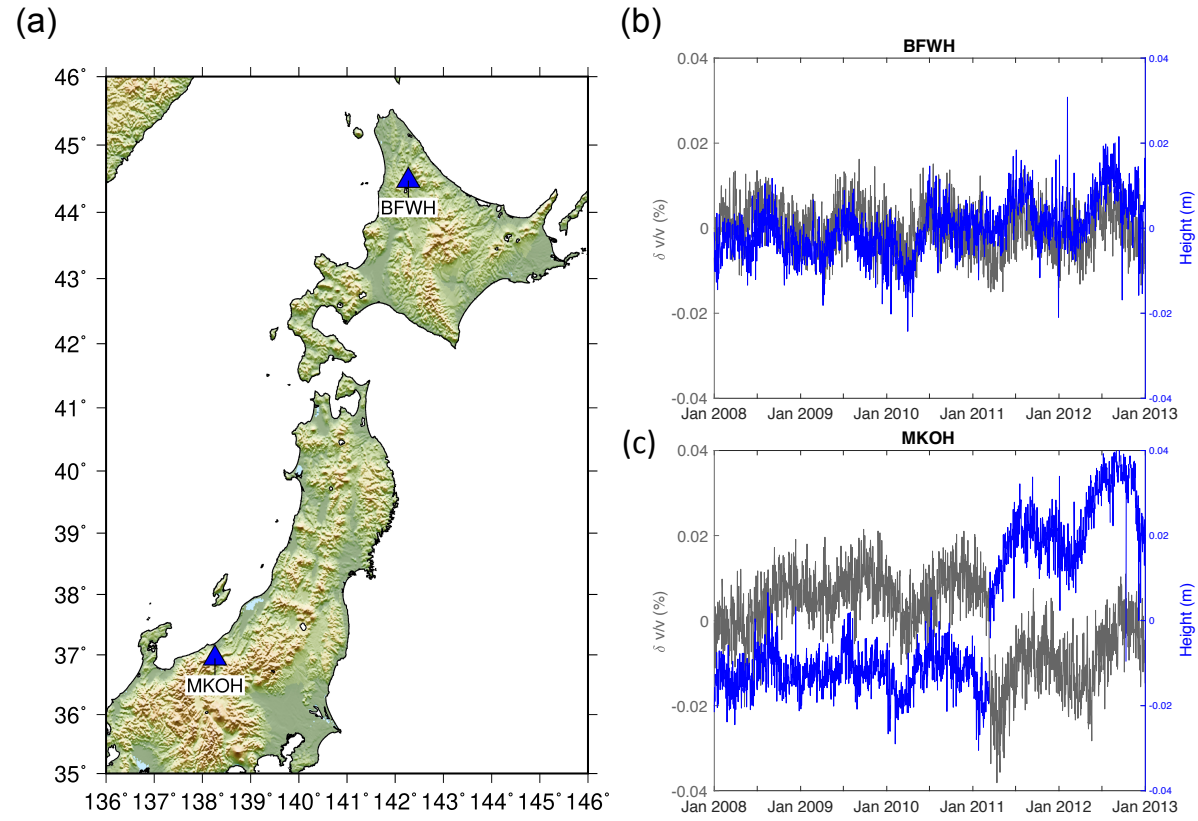

FIGURE 5.6 – (a) Locations of Hi-net seismic station BFWH and MKOH in Hokkaido and Honshu, respectively. (b) and (c) is the comparison between time series of seismic velocity changes (black curve) at BKEH and the averaged nearby GPS vertical displacements (blue curve).

of sea surface height. Munekane (2009) has also discussed the impacts of atmospheric delays, atmospheric loads and sea surface height on the GPS time series of height changes in Japan. They conclude that sea surface height is a key factor in charge of the seasonal GPS height variations along the Sea of Japan. Accordingly, these arguments confirm the analysis by **?** in this region.

5.3 Comparison with Observations by GRACE

Gravity Recovery And Climate Experiment (GRACE) monitors the gravity field and is sensitive to water stored in the Earth's crust, which is represented as equivalent water

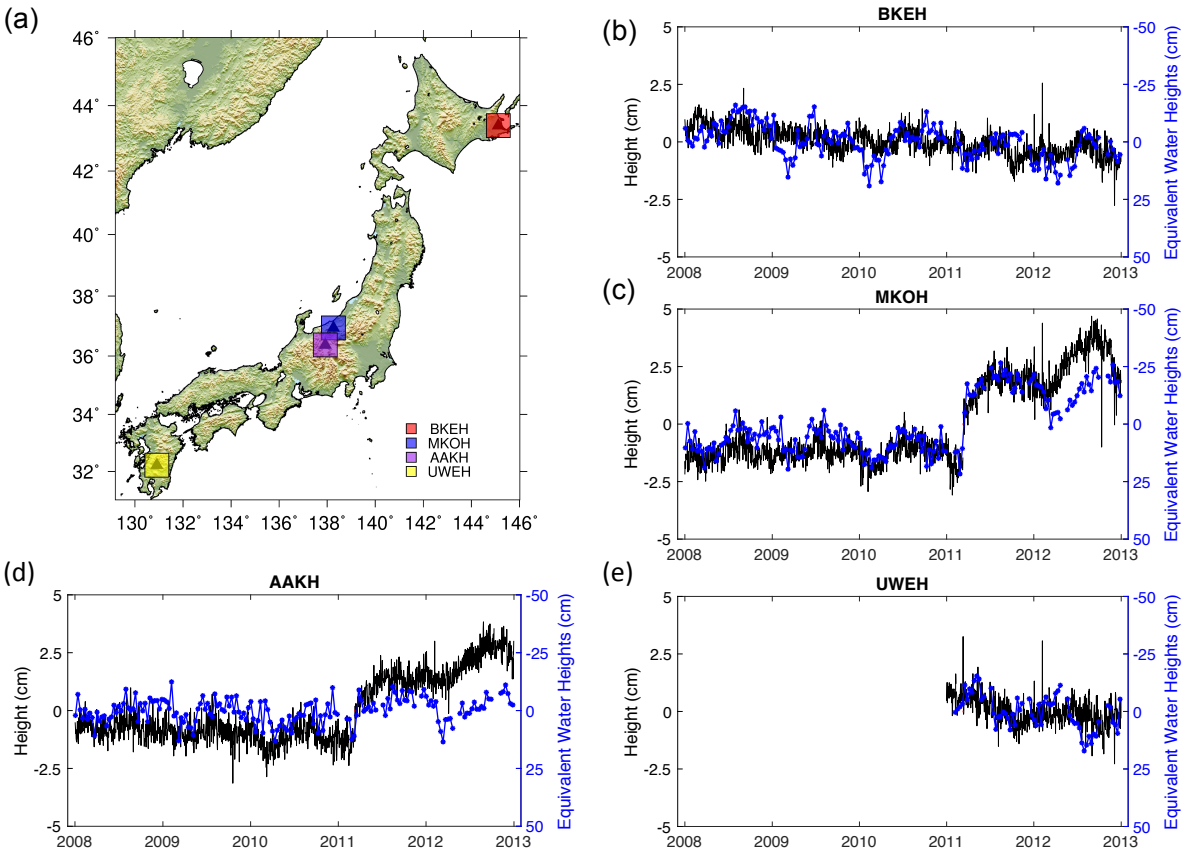

FIGURE 5.7 – The four different color indicates areas where the GRACE data is selected. (b)-(e) show the GPS heights (cm, black) and GRACE measured EWH (cm, blue) in different areas. The positive EWH is downwards plotted.

heights (EWH, cm). In this last chapter, we use the EWH $10-day$ solutions $RL03-v3$, courtesy of $CNES/GRGS$. The time-variable GRACE data after preprocessing mainly reflect the gravitational changes from hydrology, snow cover, baroclinic oceanic signals and post-glacial rebound.

We use single point extraction to get $10-day$ time series of EWH around the four seismic stations : BKEH, MKOH, AAKH, and UWEH in different locations. The single point data comes from barycentric computation from the values at the 4 surrounding grid points with a surface area of 1 deg2. There are 12 missing values during the period from 2008 to 2012. Then we extract GPS data within 30 km of these seismic stations and take the average over all related GPS heights. Both time series of GPS heights and GRACE measured EWH are demeaned.

We keep the ratio of height to EWH as -0.1 and plot the positive value of EWH downwards. Generally, the two time series at different locations show a strong negative correlation. Especially the long-term trends of five years at station BKEH (Fig. 5.7(b)) and of two years at station UWEH (Fig. 5.7(e)) outline that when the total water storage increase, the GPS height decrease due to the subsidence from the water storage. For the seasonal changes, there are some differences between the two. At station BKEH, we see clearly the increase of EWH during each winter. However, from GPS height, there is no legible seasonal change. For the other three locations, the seasonal variation of the two is basically negatively correlated. In addition to those transient responses and longterm trend, MKOH and AAKH in Honshu also exhibit rapid changes associated with the 2011 Tohoku-oki earthquake. The GPS heights increase at both locations in response to the earthquake, while the EWH decrease at both locations.

5.4 Discussion and Conclusion

By selecting several seismic stations and comparing with the nearby GPS observations, we find that the time series of seismic velocity changes show a clear positive or negative correlation with GPS vertical displacements in different regions. In both Kyushu and the western seaside of the Sea of Japan, the two positively correlate. In the central Japanese Alps region, the two negatively correlate. While in Hokkaido, we do not observe a clear correlation between the changes in seismic velocity changes and GPS height. In addition to seasonal effects, we find that the five-years long term trends of GPS height and velocity changes fit with each other in both Kyushu and eastern Hokkaido. The consistency from different observations of GPS and GRACE ensures that our seasonal changes of seismic velocity are derived from the real physical changes of the underground medium.

As the distribution of GPS stations is very dense and can be used to compare with seismic velocity measurement at each Hi-net station, we then analyze the correlation between time series of seismic wave velocity variations and GPS vertical displacements throughout Japan. Fig. 5.8 shows the maps of correlation coefficients between the two time series. In the north, we take the data in the years 2009 and 2010 to avoid the effects from the 2008 Iwate earthquake and the 2011 Tohoku-oki earthquake. In the south, we take the data from 2011 to 2012 to compare with the crustal seismic velocity changes within 8 km at depth.

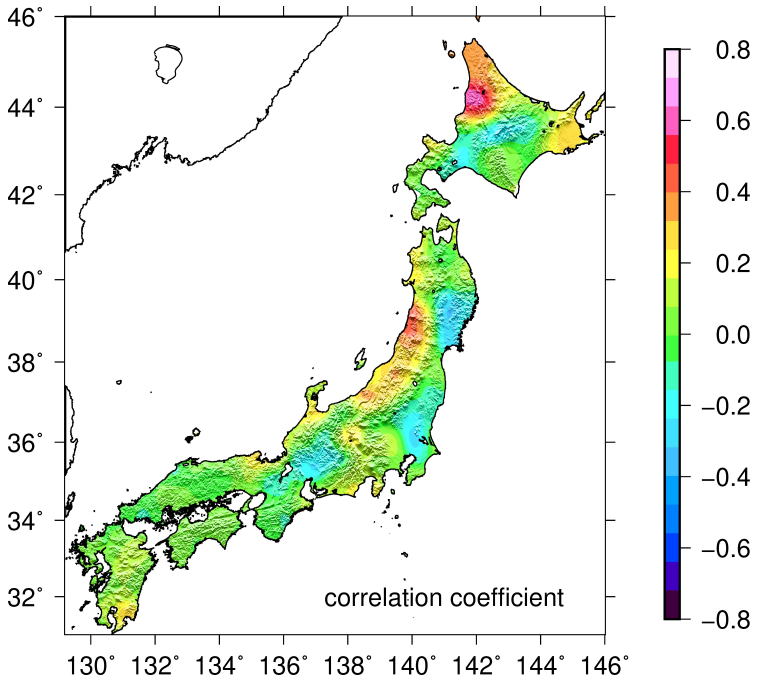

FIGURE 5.8 – Map of the correlation coefficients between the time series of seismic velocity changes and the averaged GPS height within distance of 30 km.

Overall, the two have a relatively positive correlation on the Japanese Sea side, Kyushu and the eastern corner of Hokkaido, where seasonal effects of seismic velocity changes are dominated by different environmental factors. An exception is in the central Alps region where the seismic seasonal effect is proved to be controlled by precipitation induced pore pressure changes and the two time series are negatively related. The good correlation indicates that there is a strong connection between seismic velocity changes and GPS vertical displacements, however, the responses to environmental perturbations of GPS vertical displacement and seismic velocity changes are different at different locations.

Through these comparisons above, we have summarized a few important conclusions. First, both GPS vertical displacement and GRACE-derived gravity field show strong annual patterns comparable to seismic velocity changes at the same site. The two independent geodetic observations are both useful to estimate the subsurface processes induced by seasonal changed environmental factors. Secondly, the sensitivities of seismic velocity changes to GPS heights in different areas are similar around $10^{-2}(m^{-1})$. The ratios of GPS height to GRACE measured gravity field are also constant -0.1 at different locations. Thirdly, the time series of heights and EWH are negatively correlated regarding all the long term trends, the seasonal effects, and the responses to the Tohoku-oki

earthquake. Finally, both GRACE and GPS show a strong correlation with seismic velocity changes on the western side of the Sea of Japan. This confirms the important role of sea surface height to the deformation of the crust in the adjacent coastal region. And the map of the overall correlation coefficient shows that the extent to which sea surface height may affect the crust at a seasonal time scale. The further detailed comparison needs to be done to confirm the different dominant mechanisms of seasonal effects on seismic velocity changes and GPS recorded displacements in regional scales.

With the development of noise-based monitoring, we can directly measure the change of seismic wave velocity at different depths to better and more accurately continuously monitor the real-time changes of physical properties in the crust. The three different observations can complement each other, help us better analyze the causes of seasonal changes, and more importantly, study the long-term tectonic-related changes of physical properties to understand the mechanisms of earthquake occurrence. The earthquake-related seismic velocity changes will be the focus in the following chapter.

Troisième partie

Earthquake-related Co- and Post-seismic Processes from Noise-based Monitoring

Chapitre 6

Seismic response of the M_w 9.0, 2011 Tohoku-oki earthquake beneath Japan from noise-based seismic velocity monitoring

Sommaire

6.1 Tiltmeter Data Introduction 96
6.2 Abstract 98
6.3 Introduction 99
6.4 Data and Methods 100
6.5 Spatial and Temporal evolution of seismic velocity changes 101
6.5.1 Spatial distribution of postseismic velocity changes 104
6.5.2 Temporal Variation of Seismic Velocity at Depth 107
6.6 Discussion 118
6.7 Conclusion 126

6.1 Tiltmeter Data Introduction

The previous part mainly introduced the seasonal changes of seismic wave velocity at a relatively high frequency that is expected to refer to the shallow crust. The emphases of this chapter will be shifting to study the M_w 9.0, 2011 Tohoku-oki earthquake-related seismic velocity changes. In addition to the short period Hi-net data that we have used for monitoring, the National Research Institute for Earth Science and Disaster Prevention (NIED) also deployed high sensitivity tiltmeters that are co-sited with short period sensors having burial depth of at least 100 m in the borehole (Okada *et al.*, 2004; Obara *et al.*, 2005) to monitor the deformations. They have also been used to disclose the structure of the upper mantle (Nishida *et al.*, 2008b). Fig. 6.1 shows the configuration of the Hi-net stations in the borehole and the distribution of these tiltmeter stations in the whole of Japan.

Tiltmeter recordings have two horizontal components and a flat acceleration response in the frequency band 0.002–0.5 Hz, that suggest to use them as broadband seismometers. Tonegawa *et al.* (2006) verify that tiltmeter recordings can be used in the frequency band between 0.02 and 0.16 Hz and show the comparison of the radial component recordings by the tiltmeter and a nearby broadband station. Both of them show quite similar velocity waveforms and amplitude spectra (Fig. 6.2). Nishida *et al.* (2008b) show the extraction of both Rayleigh and Love waves from the cross spectra of tiltmeter horizontal components noise recordings and build a three-dimensional crustal S wave velocity structure of Japan. Later Tonegawa *et al.* (2009) extract the body waves (direct P and S, and reflected waves) from cross-correlating the teleseismic wavefield recorded by Hi-net tiltmeters. This dense distributed broadband network provides us with the opportunity to investigate the seismic velocity changes in different frequency bands and to get the deeper temporal seismic response to the big earthquake. We start this chapter from the first successful application of tiltmeter recordings to seismic monitoring and concentrate on analyzing the depth-dependent earthquake-related seismic velocity changes in the vicinity zone of the earthquake.

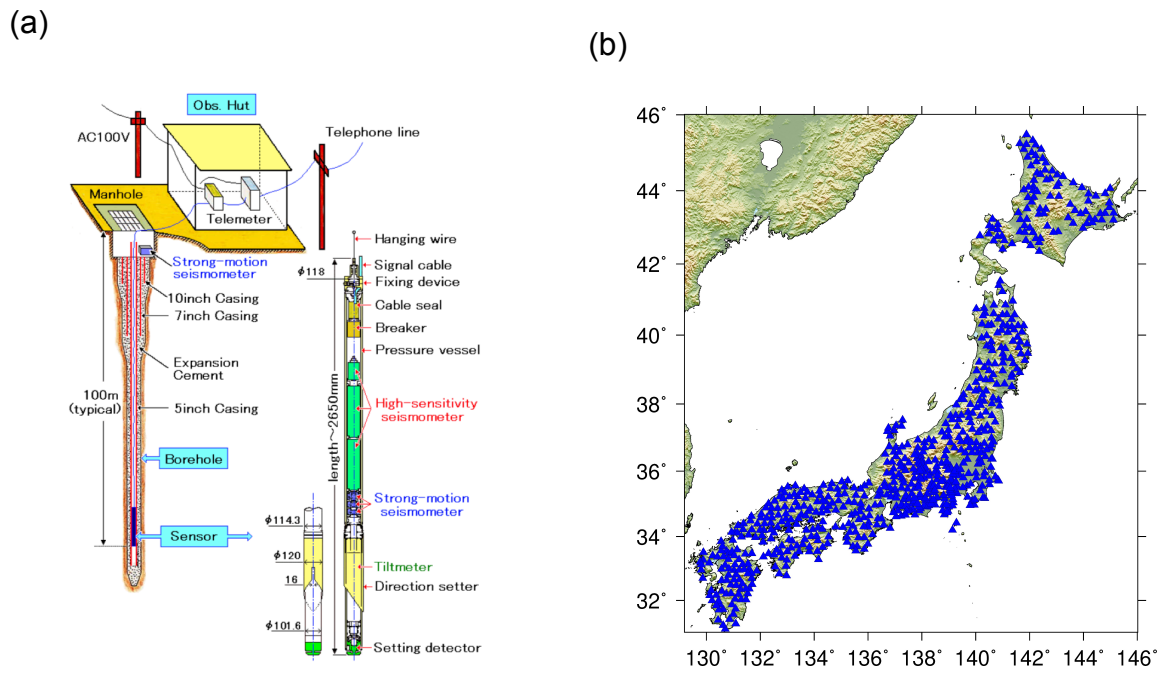

FIGURE 6.1 – (a) shows the configuration of the Hi-net stations by Okada *et al.* (2004). (b) shows the distribution of Hi-net stations (blue triangles).

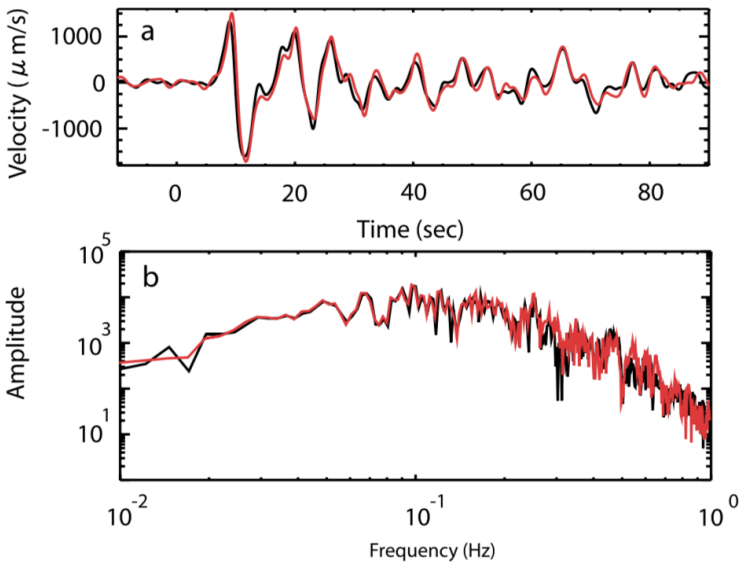

FIGURE 6.2 – Red curve indicates tiltmeter recordings and black curve indicates broadband seismogram. (a) Velocity waveform comparison (b) Amplitude spectra comparison. After Tonegawa *et al.* (2006)

SEISMIC RESPONSE OF THE M_W 9.0, 2011 TOHOKU-OKI EARTHQUAKE BENEATH JAPAN FROM NOISE-BASED SEISMIC VELOCITY MONITORING

Qing-Yu Wang[1], Michel Campillo[1], Florent Brenguier[1], Albanne Lecointre[1], Yosuke Aoki[2], Tetsuya Takeda[3,4], and Akinori Hashima[2]

1 Univ. Grenoble Alpes, CNRS, ISTerre, 38000 Grenoble, France.

2 Earthquake Research Institute, University of Tokyo, Tokyo, Japan.

3 National Research Institute for Earth Science and Disaster Prevention, Tsukuba Japan.

4 Ministry of Education, Culture, Sports, Science and Technology, Tokyo Japan.

6.2 Abstract

Studying the mechanical response of the crust to large earthquakes provides us unique insights into the processes of stress release and build up in preparation for future earthquakes. In complement to geodetic methods (GPS, InSAR) that derive crustal strain dynamics from surface observations, noise-based seismic velocity monitoring directly probes the mechanical state of the crust at depth continuously in time. In this work, we study the response of the crust to the M_w 9.0 Tohoku-oki earthquake. In addition to the Hi-net short period sensors, we employ here for the first time for the noise-based monitoring the very dense network of Hi-net tiltmeters as long period (8 – 50 s) seismometers to sample the crust below 5 km depth. The spatial distribution of strong velocity decreases at short periods appears be limited to the region of strong ground shaking induced by the 2011 Tohoku-oki earthquake, while the long period velocity changes correlate well with modelled static strain induced by fault slip. The amplitudes of coseismic velocity changes diminish with increasing period. The velocity change at longer period is delayed in time concerning the date of the earthquake. The inversion of seismic velocity changes at depth illustrates how S waves velocity changes temporally within five layers down to 50 km at regional scale after a major earthquake.

6.3 Introduction

Postseismic processes are produced by stress changes and relaxation following earthquakes. Studying postseismic processes is crucial to understand the local rheology of the crust and earthquake interactions Pollitz (1992, 2005); Freed *et al.* (2006, 2007); Fukushima *et al.* (2018). Over the past ten years, noise-based seismic monitoring started to be used for the observation of near-surface damage induced by large earthquakes (Wegler et Sens-Schönfelder, 2007; Brenguier *et al.*, 2008a; Wegler *et al.*, 2009; Taira *et al.*, 2015). The continuous monitoring of seismic velocities provides a new tool to capture the physical processes of lithospheric rheology after large earthquakes. It provides not only insight into tectonic and volcanic processes (Brenguier *et al.*, 2008a,b; Wegler *et al.*, 2009; Chen *et al.*, 2010; Obermann *et al.*, 2013; Froment *et al.*, 2013; Brenguier *et al.*, 2014; Taira et Brenguier, 2016) but also into some transient fluctuations derived from external environmental perturbations (Sens-Schönfelder et Wegler, 2006; Meier *et al.*, 2010; Tsai, 2011; Hillers *et al.*, 2014, 2015b; Wang *et al.*, 2017). The characteristic depth at which changes are monitored varies from meters (Sens-Schönfelder et Wegler, 2006; Hillers *et al.*, 2015c; Mao *et al.*, 2018) down to dozens of kilometers in the crust (Rivet *et al.*, 2013; Froment *et al.*, 2013; Obermann *et al.*, 2014) through measurements at various periods. Our goal here is to investigate the changes at depth up to 50 km at regional scale after a major earthquake.

Previous noise-based seismic monitoring studies of the M_w 9.0, 2011 Tohoku-oki earthquake, such as Brenguier *et al.* (2014); Sawazaki *et al.* (2015); Gassenmeier *et al.* (2016); Wang *et al.* (2017), rely on relatively short periods < 10 s and thus shallow depths. Brenguier *et al.* (2014); Wang *et al.* (2017) show that there is a fast coseismic decrease of velocity followed by a long-term exponential postseismic relaxation. Brenguier *et al.* (2014) point out that at shallow depth, coseismic velocity drops are mostly induced by shaking from seismic waves emitted by the M_w 9.0 mainshock. The depth of velocity changes can be estimated by considering the surface wave sensitivity kernels in the upper crust. Minato *et al.* (2012) consider that earthquake-related seismic velocity changes in the period range 2 – 10 s contain information from both stress release and strong ground motion at shallow depth. Those results show however that seismic velocity changes at relatively high frequencies are mostly sensitive to earthquake-related damage in the shallow layers (Brenguier *et al.*, 2014; Gassenmeier *et al.*, 2016).

At long period 12 – 30 s, Froment *et al.* (2013) show that seismic velocity changes reduced

by the M_w 8.0 Wenchuan earthquake are very different from the velocity changes at short period (Obermann *et al.*, 2018). The intent of this study is to investigate with long period signals the velocity variations induced by the Tohoku-oki earthquake at depth. We use both Hi-net short period and tiltmeter data (Obara *et al.*, 2005; Okada *et al.*, 2004) to measure the frequency-dependent velocity changes before, during and after the M_w 9.0, 2011 Tohoku-oki earthquake. We validate the feasibility of using tiltmeter recording to measure monthly seismic velocity changes in the period bands 8 – 30 s and 15 – 50 s and combine these observations with results from the Hi-net short period data corrected from seasonal effects in the period band 1 - 7 s.

We find that the spatial distribution of velocity changes shows high correlation with strong motion amplitude in the period band 1 – 7 s, and with coseismic dilatation for longer periods. At long period, the maximum of velocity drop is delayed from the time of the earthquake occurrence, with a time lag depending on the period that could be as large as six months. This suggests that the processes responsible for the velocity changes are different at the surface and at depth.

6.4 Data and Methods

In this study, we restrict the studied area close to the rupture zone in Honshu. We select 190 tiltmeter stations (Fig. 6.4(a)) with recording gaps less than 5% and spanning from 2008 to 2012. Tonegawa *et al.* (2006); Nishida *et al.* (2008b) have used tiltmeter data as broadband seismometers in Japan for tomography. The comparison of both velocity waveforms and amplitude spectra between recordings from tiltmeter recordings and nearby broadband stations show strong similarities between these two types of data (Tonegawa *et al.*, 2006).

The routine preprocessing of continuous signals consist of 1-bit normalization and spectral whitening from 0.02 Hz to 0.125 Hz. These operations aim at improving the temporal stability of the noise records and at decreasing the effects of temporal changes in the microseismic sources (Campillo et Paul, 2003; Shapiro et Campillo, 2004; Shapiro *et al.*, 2006). We stack daily cross-correlation functions over every 30 days starting from 28 Jan 2008 and smooth the stacked cross-correlation functions using a 30 days moving average window. Then we adopt the doublet and inversion methods by Brenguier *et al.* (2014) to retrieve accurate monthly velocity changes for all the 7636 horizontal component-pairs

up to 90 km apart. The doublet measurements are in two period bands 8 – 30 s and 15 – 50 s, for which the moving window lengths are 30 s and 50 s respectively, from -400 s to 400 s of the time lag with 60% overlap. For each station, we average all related pairs within 90 km and obtain time series of monthly seismic velocity changes lasting for five years.

6.5 Spatial and Temporal evolution of seismic velocity changes

In addition to measurements using tiltmeter signals at period 8 – 50 s, we also measure time series of seismic velocity changes corrected from seasonal effects in period band 1 – 7 s using both vertical and horizontal components of Hi-net short period data (Wang *et al.*, 2017) with the same procedure including the same time average of the cross-correlations. The smoothness of the response therefore affected in exactly the same way. The evolution of spatial and temporal seismic velocity changes at different periods enable revealing depth-dependent Tohoku-oki earthquake-related co- and post-seismic physical processes.

We select 7 seismic stations at different distances from the epicenter of the Tohoku-oki earthquake. The Fig. 6.3 shows the locations of the 7 sites (6.3(a)) and time series of seismic velocity changes in three different period ranges in order from north to south (6.3(b – h)).

Globally, we can observe that the amplitudes of seismic velocity changes decrease as the period increase. This means that the velocity changes greatly in the shallow layers, and as the depth increases, the velocity changes weaken. However, the ratios of amplitudes within three time series differ a lot at different locations. As well as the postseismic recovery procedures are very different in the three different period bands that we studied.

For short period in 1 - 7 s, large seismic velocity changes coincident with the 2011 Tohoku-oki earthquake can be observed at all the seven stations and then recovers gradually. We find that the velocity changes do not recover to the initial level at the end of 2012 for all Hi-net stations. The coseismic velocity drop is stronger near the earthquake and this drop decreases rapidly with the increase of the epicentral distance (6.3 (b) - (h)). The stations HMNH and KAKH also show the sudden seismic velocity drops coincident with the 2008

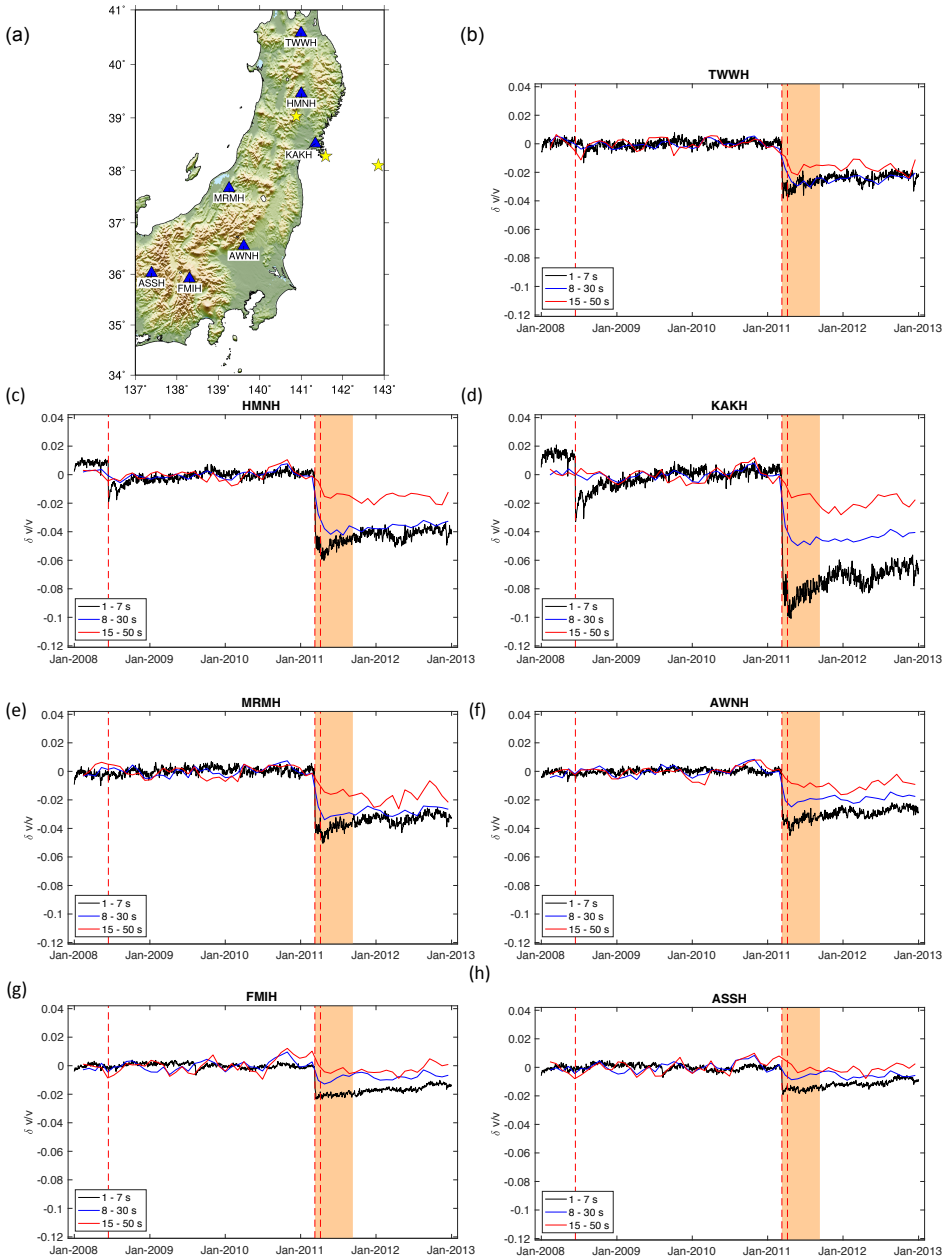

FIGURE 6.3 – (a) locations of selected Hi-net stations. (b) - (h) Time series of seismic velocity changes in different period ranges for Hi-net stations TWWH, HMNH, KAKH, MRMH, AWNH, FMIH, and ASSH. Yellow stars indicate separately the M_w 6.9, 2008 Iwate-Miyagi Nairiku earthquake (39.030°N 140.881°E) and M_w 9, 2011 Tohoku-Oki earthquake (38.297°N 142.373°E), and the aftershock of Tohoku-oki earthquake (38.1°N 141.86°E). The shaded area include six months after the Tohoku-oki earthquake. The three vertical red dashed lines indicated separately the days of Iwate-Miyagi Nairiku earthquake, Tohoku-oki earthquake, and the aftershock on the April 7^{th}, 2011.

Iwate-Miyagi Nairiku earthquake. Note that the velocity changes have not recovered to the level before the earthquake.

For seismic velocity changes in 8 - 30 s and 15 - 50 s relatively long period ranges, there is almost no coseismic velocity drop. We can only observe coseismic velocity drops coincident with the 2011 Tohoku-oki earthquake for stations nearby the epicenter, which are stations TWWH, HMNH, KAKH, MRMH, and AWNH. The amplitude of velocity drops are smaller than that in 1 - 8 s. However the co- and postseismic responses do not differ strongly at different sites. During first several months after the earthquake, seismic velocity continues to decrease. Especially in 15 - 50 s, velocity tends to be minimum till around the end of 2011. This delayed response in time may be controlled by some deep factors, about which we will discuss in detail.

For the ratios of amplitudes at different locations, we first define three ratios r_{12}, r_{13}, and r_{23} as separately the ratio between the amplitudes of curves in period band 1 - 7 s and of curves in period band 8 - 30 s, between the amplitudes of curves in period band 1 - 7 s and of curves in period band 15 - 50 s, and between the amplitudes of curves in period band 8 - 30 s and of curves in period band 15 - 50 s.

a) There is little seismic response regarding the velocity changes at FMIH and ASSH in period bands 8 - 30 s and 15 - 50 s. So we focus on how the ratios vary at the other five sites.

b) First, at KAKH, the site closest to the earthquake, we observe that seismic velocity changes are very distinguishable, and there are big r_{12}, r_{13}, and r_{23}.

c) At station AWNH, when the distance exceeds a specific value, the co- and post seismic velocity responses at long period 8 - 30 s and 15 - 50 s tend to decrease too. There are also distinguished seismic velocity changes in different period bands.

d) At station TWWH, seismic velocity changes in three period bands are quite similar. The three ratios are approximately equal to 1.

e) Then for the other two stations HMNH and MRMH, r_{12} is almost 1. This implies that amplitudes of velocity changes decrease faster with distance in short period band 1 - 7 s than in long period band 8 - 30 s. The amplitudes of seismic velocity changes in 15 - 50 s period band are smaller compared in other period bands. r_{13} and r_{23} are similar.

6.5.1 Spatial distribution of postseismic velocity changes

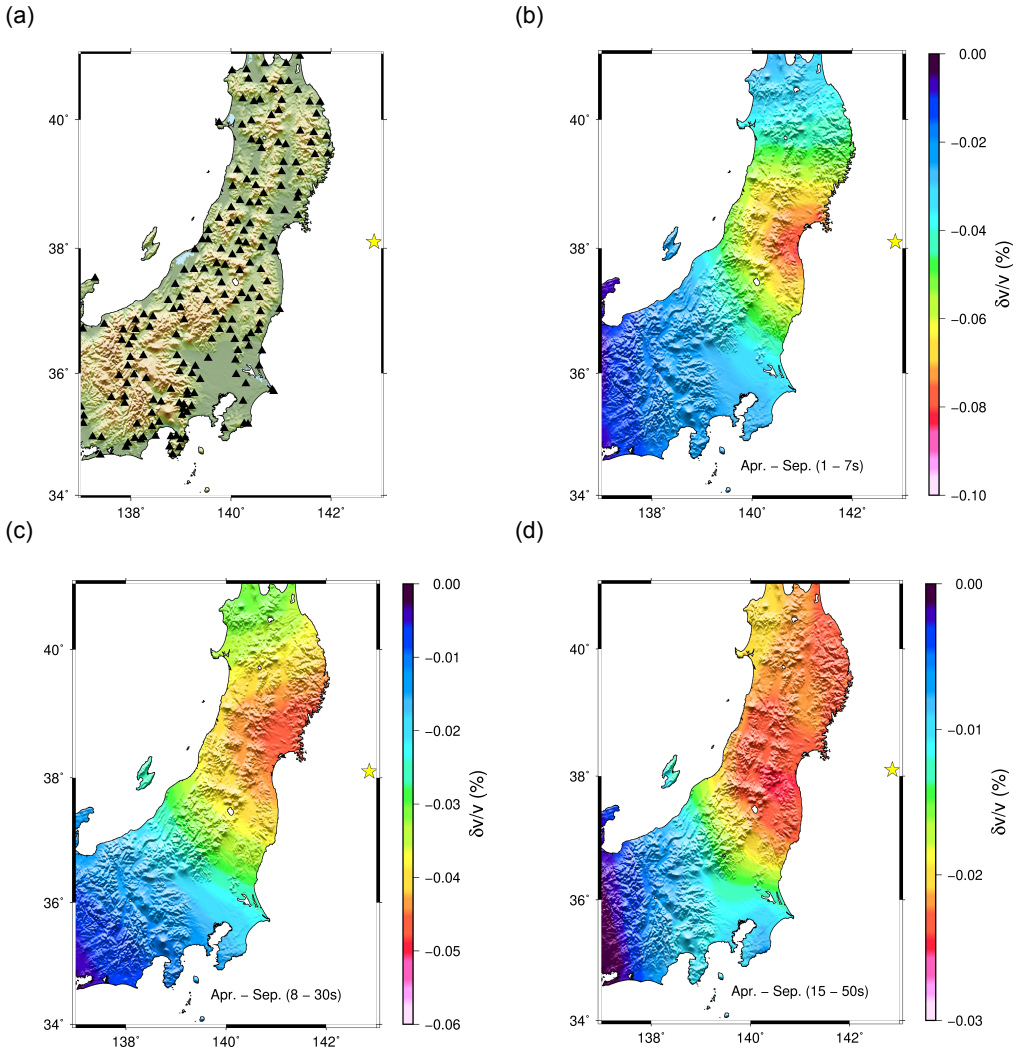

FIGURE 6.4 – (a) distribution of 190 tiltmeter stations; (b) – (d) Mapping of the mean co- and post-seismic velocity changes over months from April to September in 2011, for 1 – 7s, 8 – 30s, and 15 – 50s, respectively.

Assuming the preseismic velocities fluctuate around 0, we first remove the mean seismic velocity changes before the Tohoku-oki earthquake and compute mean velocity changes over six months following the Tohoku-oki earthquake from April to September in 2011. We map the spatial distribution of mean values using linear interpolation with the resolution of 1 arc-minute ($\sim$ 2 km) after averaging over all stations spacing less than or equal to 100 km for all the 190 stations in three period ranges (Fig.6.4 (b - c)).

Fig.6.4 (b, c, and d) illustrate that seismic responses at different periods are very distinct.

In 1 – 7 s period band (Fig.6.4 (b)), velocity decreases strongly down to −0.08% in the surrounding region of Miyagi, which is not adjacent to the epicenter of 2011 M_w 9.0 Tohoku-oki earthquake. The amplitude of maximum drop decreases outwards from the center area around Sendai. Different from velocity changes in 1 – 7 s period band, the location with most substantial velocity changes for 8 – 30 s period range is shifted northeast to the coastlines of southern Iwate and northern Miyagi (Fig.6.4 (c)). The most significant velocity drop reaches 0.05%, which is smaller than that at short periods. For period band 15 – 50 s (Fig.6.4 (d)), this value reduced to 0.025%. The co-seismic velocity changes for 15 – 50 s period band show a much smaller amplitude compared with other periods. The area with strong velocity changes spreads mostly to the north and south Honshu. Both geographic limits of spatial distribution of seismic velocity changes in 8 – 30 s and 15 – 50 s period ranges is to the volcanic front associated with the subduction of Pacific Plate. The difference features of distribution of velocity variations in different period bands may suggest that the origins of the seismic velocity changes are disparate.

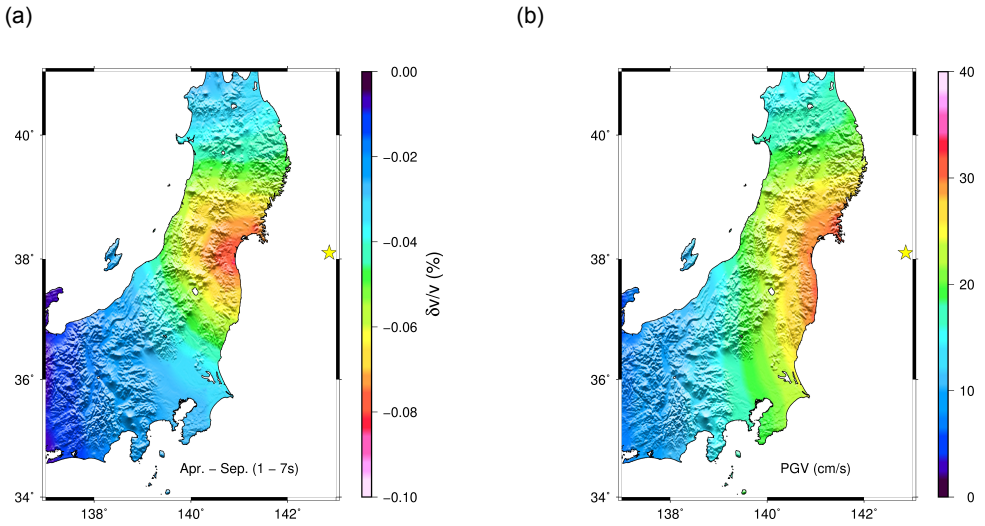

FIGURE 6.5 – (a) Mean postseismic velocity changes over months from April to September in 2011 in 8–30s. (b) Map of PGV (cm/s).

In order to clarify the main origins of velocity changes in different period ranges, we compare the maps of seismic velocity changes with map of pgv and deformation in the crust, respectively. Fig.6.5 shows the velocity changes in short period range 1–7 s and the root summed squares of peak ground velocity (PGV) measured from three downhole components. Both of them are smoothed over 100 km before mapping. The spatial distribution of postseismic velocity changes shows similarities with the regions

of strong shaking. This similarity suggests that seismic velocity changes at short period are sensitive to changes of the medium due to shaking, lightly related with the non-linear behavior of superficial unconsolidated shallow layers. This is consistent with the conclusions about the seismic velocity susceptibility by Brenguier *et al.* (2014) that is the ratio between the changes of seismic velocity ($\delta v/v$) and dynamic stress $\dot{\epsilon}$, which is $\frac{\delta v/v}{\dot{\epsilon}}$, where $\dot{\epsilon} \sim \dot{u}(t)$ (PGV). The authors point out that the crustal seismic velocity reduction is related to the mechanical weakening of the crust by the dynamic stress associated with the seismic waves. And also Sawazaki *et al.* (2015) prove that shallow damage is the predominant factor for short period seismic velocity changes.

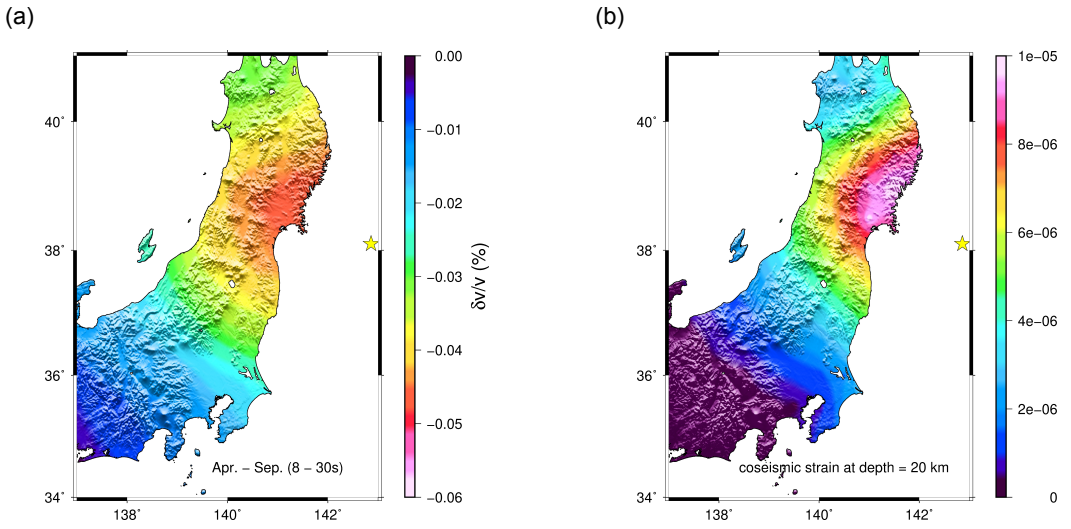

FIGURE 6.6 – (a) Mean postseismic velocity changes over months from April to September in 2011 in 8–30s. (b) Modelled coseismic static strain at the depth of 20 km.

Fig.6.6 shows map of seismic velocity changes in 8 – 30 s and map of coseismic dilatation at 20 km at depth. Coseismic dilatation is calculated using a 3-D depth-dependent viscoelastic finite element model based on the GPS displacements (Freed *et al.*, 2017). Both of maps are smoothed over 100 km before mapping. We observe that the area of maximum velocity drop is shifted to the northeast and is in agreement with the spatial distribution of coseismic static strain. The different temporal evolution and different spatial distribution of seismic velocity changes indicate the existence of differences of behaviors at the different depths probed by our measurements. A first order conclusion is the existence of specific changes at depth, different from the ones in the shallow layers, the latter is likely dominated by strong shaking. In the following, we investigate quantitatively the depth dependence of the seismic velocity changes.

6.5.2 Temporal Variation of Seismic Velocity at Depth

6.5.2.1 Averaged Seismic Velocity Changes

74 Hi-net stations in the most affected area (the red trapezoidal shaded zone, Fig.6.7 (a)) are selected to measure the averaged temporal evolution in four period ranges 1 – 7 s, 8 – 16 s, 15 – 30 s, and 20 – 50 s. Fig.6.7 (b) shows the monthly averaged time series of seismic velocity changes in four different period bands. Overall, seismic velocity decreases resulted from the Tohoku-oki earthquake. Coseismic responses are of the same order of magnitude (10^{-4}) in four different period ranges and tend to be smaller with increasing periods.

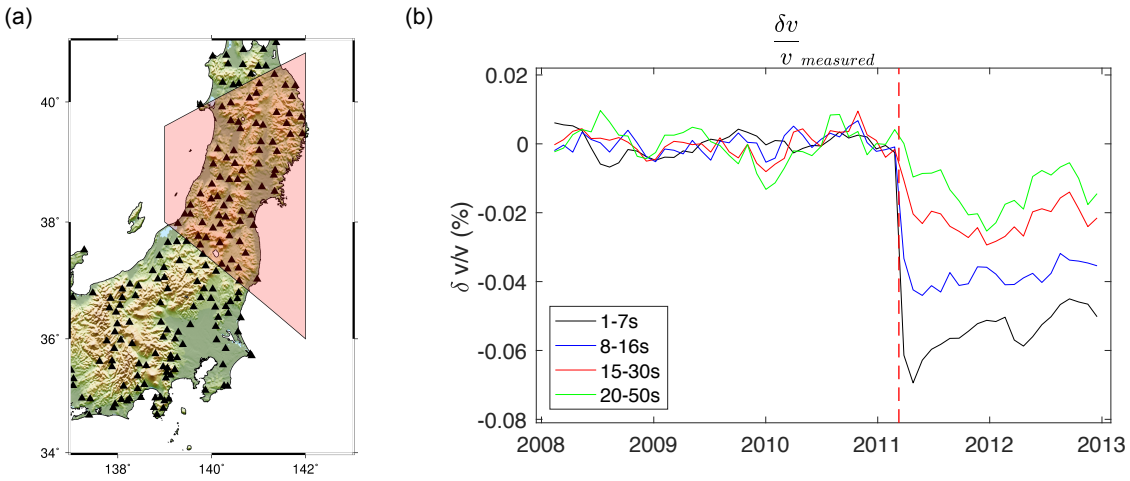

FIGURE 6.7 – (a) is the map of tiltmeter stations with red shaded area, where seismic velocity changes are selected to see the temporal evolution. (b) Time series of seismic velocity changes averaged over stations in the red shaded area in four different period ranges.

For postseismic velocity changes in 1 – 7 s period band, velocities decrease instantaneously when the earthquake occurred and recovered relatively fast within the first few months. In the 10 – 20 s period range, the coseismic velocity decrease down to -0.04% and recover slowly. For long period ranges 15 – 30 s and 20 – 50 s, it is important to highlight a delayed response. The maximum velocity drop is delayed from the time of the earthquake occurrence, with a time lag depending on the period ranges that could

be as large as six months. The two shapes of these curves are different means that there are different behaviors at different depths. If the changes of physical properties happened only at the surface, the curves at different frequencies would have different amplitudes but the same shape. Therefore, this difference suggests a depth-dependent rheology with non-elastic behavior extended into the lower crust. This is another evidence in addition to the different spatial distribution of changes in different period ranges.

A similar delayed minimum is also observed by Froment *et al.* (2013) for the case of the 2008 Wenchuan earthquake (May 12, M_w 8.0). They find the delay of $\sim$ 3 months after the main shock in 12 – 20 s period band. Velocities tend to decrease gradually during the first three months after the mainshock and reach the minimum around July. By contrast with our results, seismic velocity changes in Wenchuan are more significant at long period compared to the short period. This may result from the low velocity zone in the Earth's crust at depths of 20 – 40 km as reported by Chen *et al.* (2018), where velocity perturbations could be stronger than in shallow layers. The delayed seismic velocity changes in Wenchuan is argued to be due to the non-linear viscoelastic seismic response from the lower crust. Nevertheless, the precise physical meaning of this delay remains unclear.

6.5.2.2 Inversion of Seismic Velocity Changes

To better understand the period-dependent seismic velocity changes, we firstly invert our measurements into four different period bands for a five layer model reaching a depth of 50 km. In this study, we measure the seismic velocity changes for each 30 days (monthly) in four different frequency bands. Assuming coda waves are predominated by surface waves, the inversion is based on the frequency-dependent Rayleigh waves sensitivity kernels $K_{dc/d\beta}(f)$ (Fig.6.8 (c)). We use the velocity model by Matsubara *et al.* (2017) and take the mean value (Fig. 6.8 (b)) for calculating $K_{dc/d\beta}(f)$ in the red shaded area shown in Fig. 6.8 (a). The inversion problem is expressed as :

$$\underset{M\times 1}{d} = \underset{M\times N}{G}\ \underset{N\times 1}{m}, \tag{6.1}$$

where d is the observation vector consisting of $\delta v/v$ in four different period ranges. $\delta v/v_{f_i,t_M}$ represents velocity changes in frequency band i and in month t. m is the model of velocity changes in each layer at depth. So for velocity changes in each month, if we invert the seismic velocity changes into five layers, the relationship 6.1 turns into :

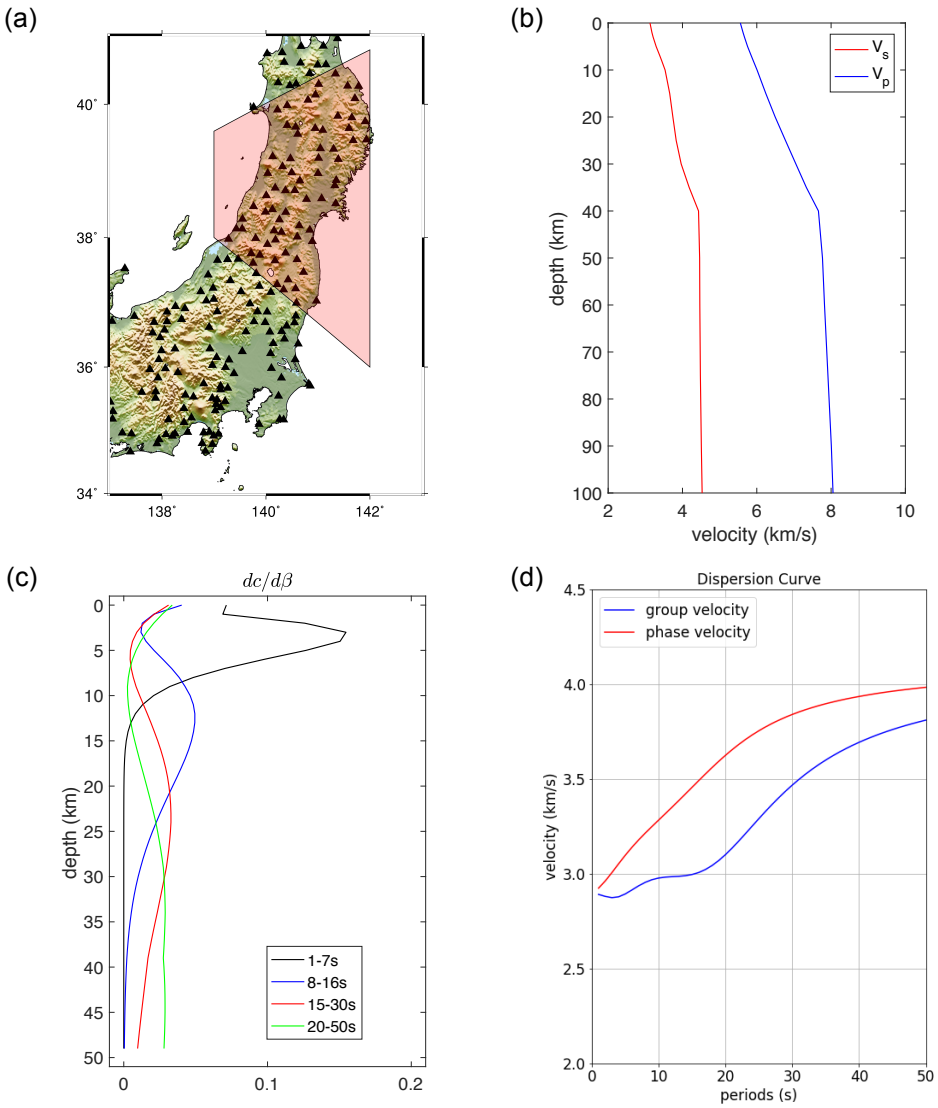

FIGURE 6.8 – (a) gives the red shaded area for averaging the velocity model ; (b) shows the averaged velocity model after interpolating at 1 km resolution ; (c) are normalized sensitivity kernels of the median period in different period ranges ; (d) Dispersion curves of the fundamental mode of Rayleigh waves from the averaged velocity model.

$$\begin{bmatrix} \delta v/v_{f_1,t} \\ \delta v/v_{f_2,t} \\ \delta v/v_{f_3,t} \\ \delta v/v_{f_4,t} \end{bmatrix} = \begin{bmatrix} K'_{f_1,d_1} & K'_{f_1,d_2} & K'_{f_1,d_3} & K'_{f_1,d_4} & K'_{f_1,d_5} \\ K'_{f_2,d_1} & K'_{f_2,d_2} & K'_{f_2,d_3} & K'_{f_2,d_4} & K'_{f_2,d_5} \\ K'_{f_3,d_1} & K'_{f_3,d_2} & K'_{f_3,d_3} & K'_{f_3,d_4} & K'_{f_3,d_5} \\ K'_{f_4,d_1} & K'_{f_4,d_2} & K'_{f_4,d_3} & K'_{f_4,d_4} & K'_{f_4,d_5} \end{bmatrix} \begin{bmatrix} \delta v_s/v_{sd_1,t} \\ \delta v_s/v_{sd_2,t} \\ \delta v_s/v_{sd_3,t} \\ \delta v_s/v_{sd_4,t} \\ \delta v_s/v_{sd_5,t} \end{bmatrix}, \tag{6.2}$$

where $K'_{f_i,d_j} = K_{f_i,d_j} * \dfrac{\beta_{d_j}}{c_{f_i}}$ and is deduced from :

$$\begin{aligned} dc_{f_i} &= K_{f_i,d_j} * d\beta_{d_j} \\ \frac{dc}{c}_{f_i} &= K_{f_i,d_j} * \frac{\beta_{d_j}}{c_{f_i}} * \frac{d\beta}{\beta}_{d_j} \\ \frac{dc}{c}_{f_i} &= K'_{f_i,d_j} * \frac{d\beta}{\beta}_{d_j} \\ \Rightarrow K'_{f_i,d_j} &= K_{f_i,d_j} * \frac{\beta_{d_j}}{c_{f_i}} \end{aligned} \tag{6.3}$$

β_{d_j} and c_{f_i} are defined as the mean value within the j^{th} layer and in the i^{th} period band, respectively. K_{f_i,d_j} indicates the surface waves sensitivity kernels in frequency band i and at a certain depth j for each layer. We compute the dispersion curves of the fundamental mode of Rayleigh waves (Fig. 6.8 (d)) from the averaged velocity model.

The Eq. 6.2 is an under-determined system without prior information. We adopt the damped least-squares (DLS) method, also known as Levenberg-Marquardt method to solve the problem. This method minimizes :

$$\|Gm - d\|^2 + \epsilon^2 \|m\|^2, \tag{6.4}$$

where ϵ indicates a norm damping. And the solution m without considering the smoothing term is :

$$m = \left(G^T G + \epsilon^2 I\right)^{-1} G^T d. \tag{6.5}$$

The term $\left(G^T G + \epsilon^2 I\right)^{-1} G^T$ is often referred to as G^{-g}, the generalized inverse. The resolution operator R, which is referred to as the model resolution matrix or resolving

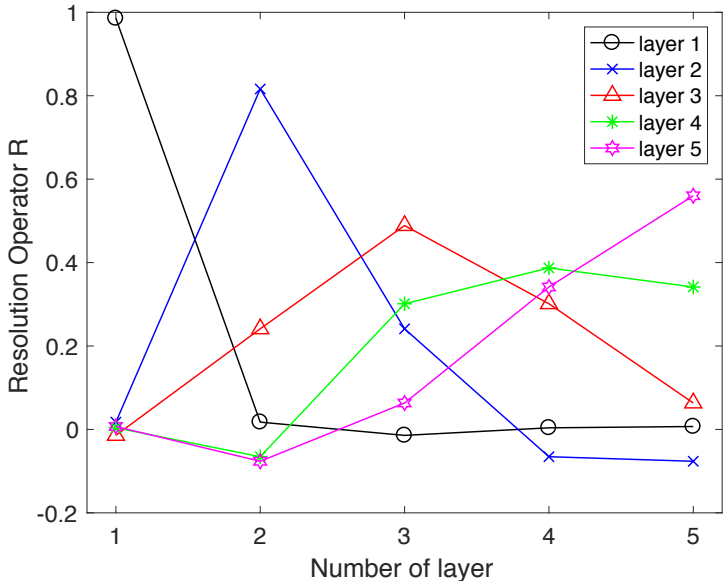

FIGURE 6.9 – the resolution operators R for the $\delta v_s/v_s$ within five layers.

kernel, describes the relationship between the true m_{true} and m from inversion, where $m = Rm_{true}$. The perfect R should equal to I the identity matrix. R takes the form as :

$$R = G^{-g}G \tag{6.6}$$

The damping coefficient for this inversion is fixed as $\epsilon = 0.15$ according to the Fig. **??** by searching the inflection point. Velocity changes in different months are independent and share the same sensitivity kernels K. Thus, R is a 5-by-5 matrix and the same for seismic velocity changes at different time points. The resolution kernel in each layer for each time t is shown in Fig. 6.9. The diagonal values of R are the biggest for each layer. According to Fig. 6.9, the first three layers can be better inverted than the last two deep layers. The first layer has the best resolution. The process is repeated for each time step of one month between 2008 and 2012.

Depth localization of S waves velocity changes $\frac{\delta v_s}{v_s}(t, z)$ is shown in (Fig.6.11 (c) and (d)). We can observe that the amplitudes of changes weaken when depth increases. At the end of 2012, velocity changes at different depths have not recovered to the initial state before the earthquake. The time delay of the maximum velocity drop becomes larger at depth. The recovery appears to be faster at depth compared in the upper layer. Strong changes are mainly located in shallow layer within 5 km in the crust, and it's hard to

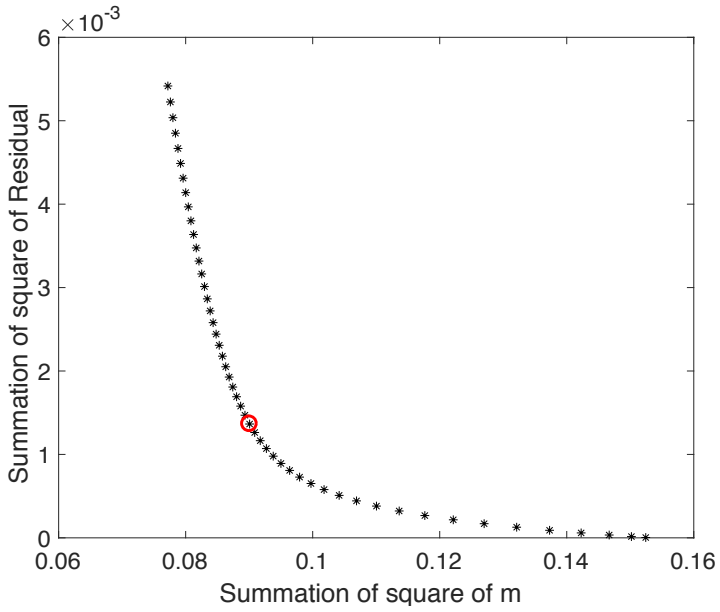

FIGURE 6.10 – Summed residual versus summed m for searching the best-fitting norm damping coefficient ϵ. The red circle indicates $\epsilon = 0.115$, which is used for inversion.

confirm if there is any physical change below 30 km, as $\delta v_s/v_s$ is not obvious enough and the amplitudes of changes are comparable with the fluctuations before the earthquake happened.

6.5.2.3 Inversion with Random Perturbation

For the sake of verifying the impact of random perturbations on the inversion results. We separately add 0.01% random noise to the measured results of different period bands, and then use the same inversion steps and coefficients to invert seismic velocity changes from different period bands into different layers in depth based on the normalized Rayleigh waves sensitivity kernels in order to study the contribution of each period band on the inversion results.

Fig.s 6.12, 6.13, 6.14, 6.15 show the original measured seismic velocity changes in four period ranges (Fig.s 6.12, 6.13, 6.14, 6.15 (a)) and how they change after adding 0.01% random noise (Fig.s 6.12, 6.13, 6.14, 6.15 (b)). (Fig.s 6.12, 6.13, 6.14, 6.15 (c) and (e)) give results of inverted s wave velocity changes plotted versus depths.

By contrast, we can summarize how the 0.01% random perturbation affect the inversion

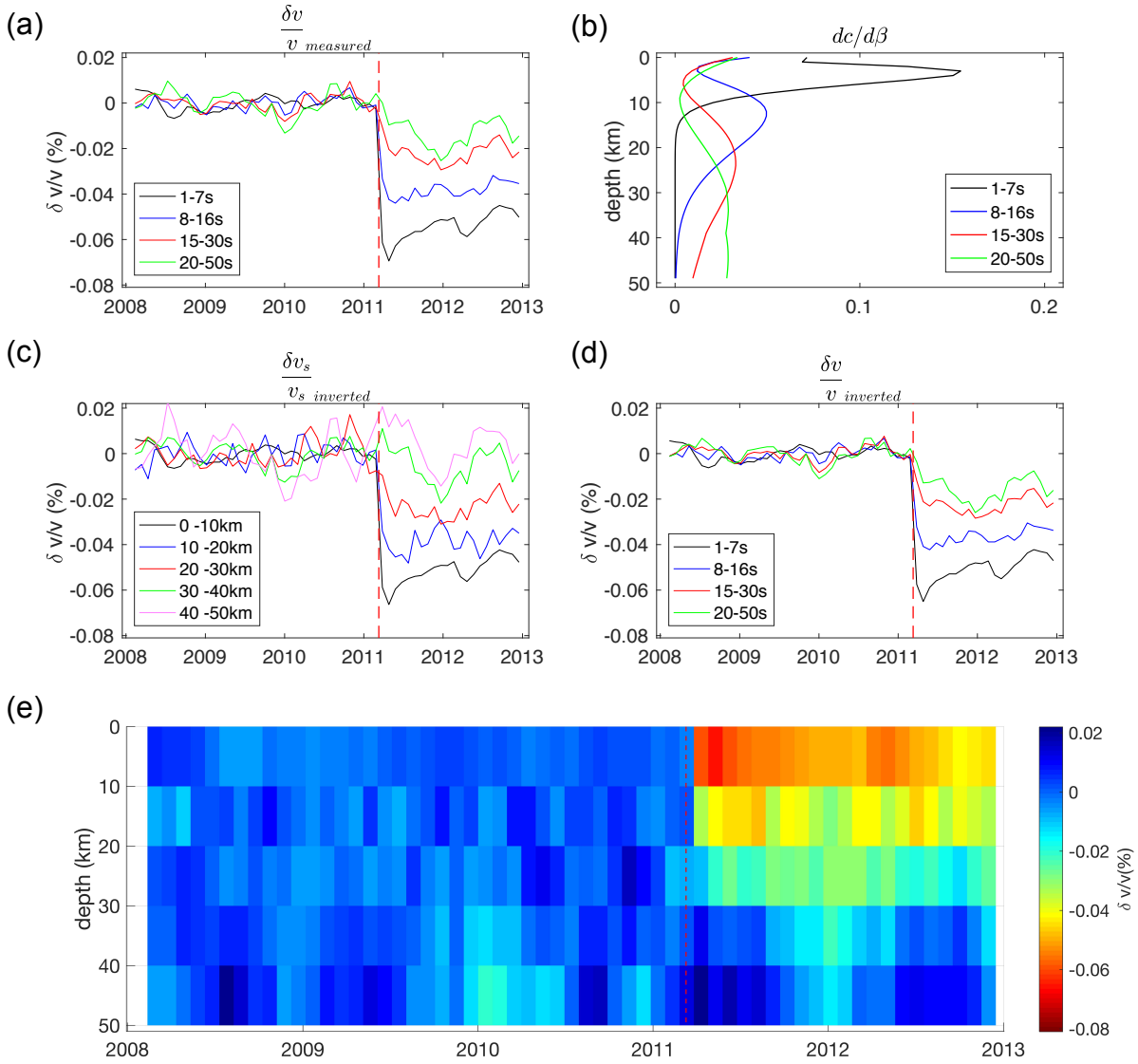

FIGURE 6.11 – (a) Measured monthly seismic velocity changes in four period ranges. (b) Normalized sensitivity kernels of Rayleigh waves to shear waves. (c) Inverted monthly S waves velocity changes versus depth from 2008 to 2012. (d) Summation of the inverted seismic velocity changes (e) Inverted monthly S waves velocity changes from 2008 to 2012 down to 50 km at depth.

results. Separately, the short-period (1 – 7s) interference only has a large impact on the inversion results of the first layer, and the deep results hardly change. The change in other period ranges show same features as in 1 – 7 s. Perturbations in 8 – 16 s period range has a big impact on the second layer, 15 – 30 s has a big impact on the third

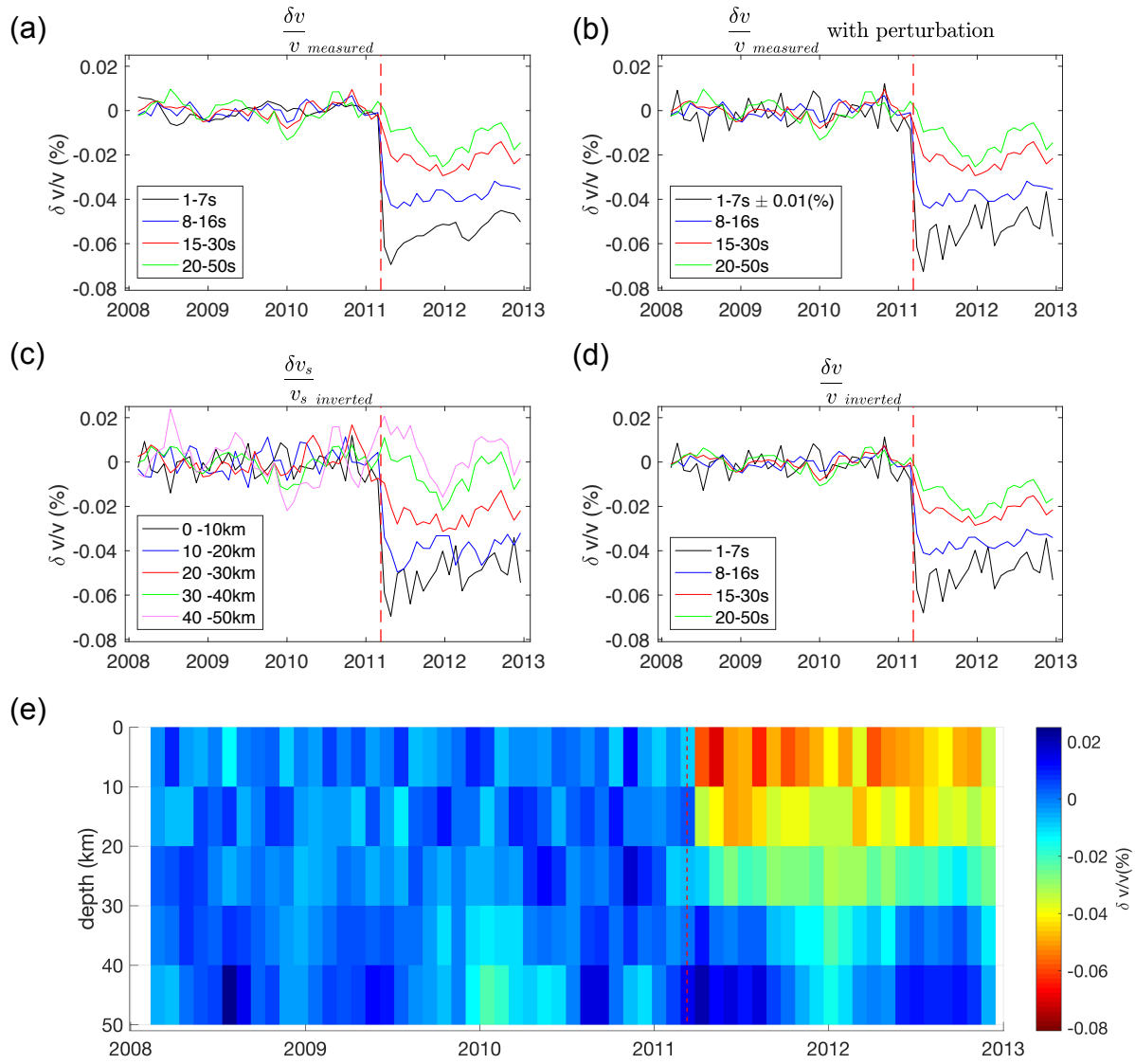

FIGURE 6.12 – (a) Measured monthly seismic velocity changes in four period ranges. (b) Measured monthly seismic velocity changes in four period ranges after adding 0.01% random perturbation in 1–7 s period range. (c) Inverted monthly S waves velocity changes versus depth from 2008 to 2012. (d) Summation of the inverted seismic velocity changes (e) Inverted monthly S waves velocity changes from 2008 to 2012 down to 50 km at depth.

layer, and 20 – 50 s has impact on both the forth and fifth layers. The addition of noise in 15 – 30 s period range generates the greatest interference with the inversion results. Overall, each inversion result after noising can basically re-obtain the characteristics of

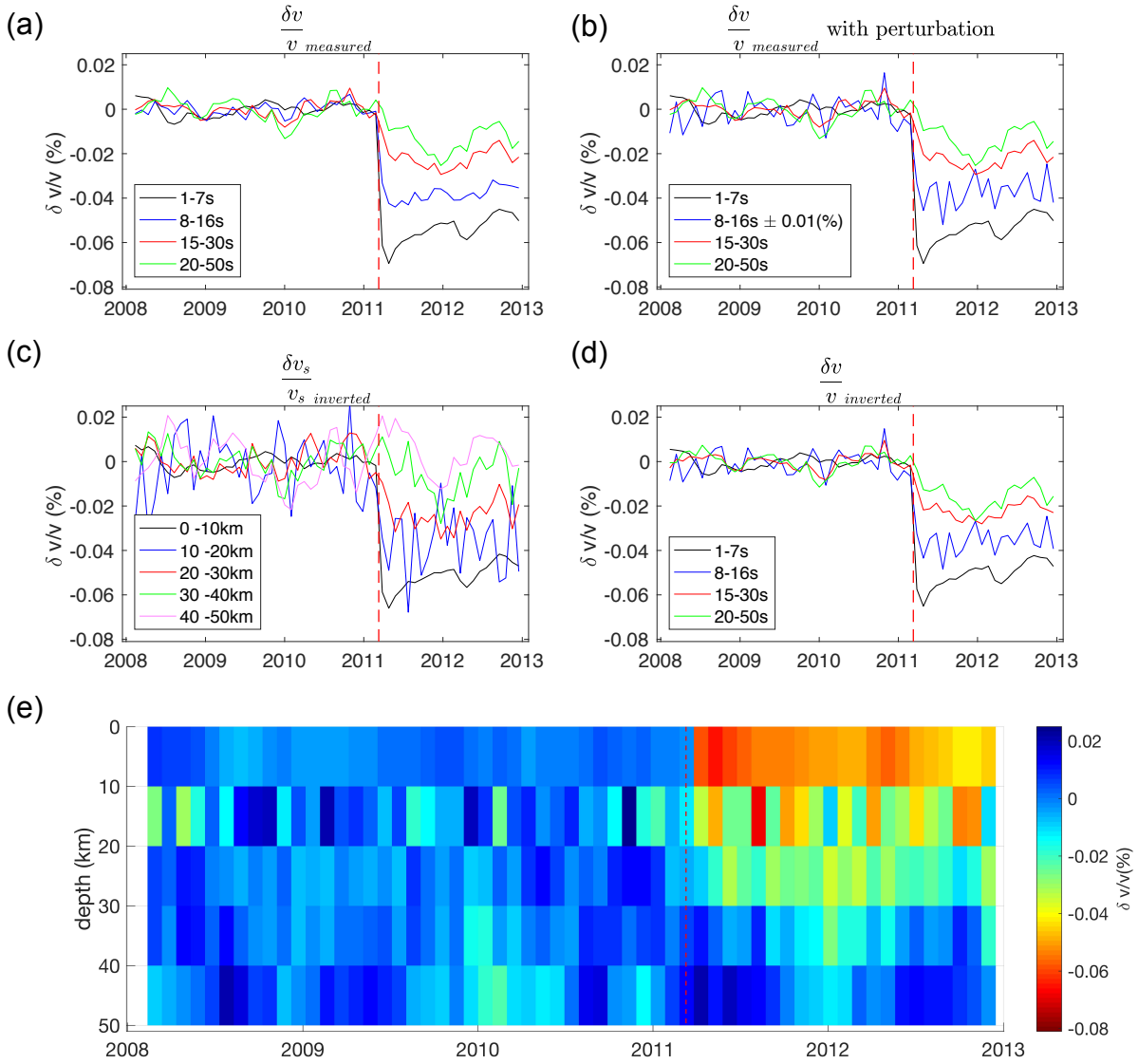

FIGURE 6.13 – (a) Measured monthly seismic velocity changes in four period ranges. (b) Measured monthly seismic velocity changes in four period ranges after adding 0.01% random perturbation in 8–16 s period range. (c) Inverted monthly S waves velocity changes versus depth from 2008 to 2012. (d) Summation of the inverted seismic velocity changes (e) Inverted monthly S waves velocity changes from 2008 to 2012 down to 50 km at depth.

the s-wave velocity variations with depth similar to the previous one shown in Fig. 6.11 (e).

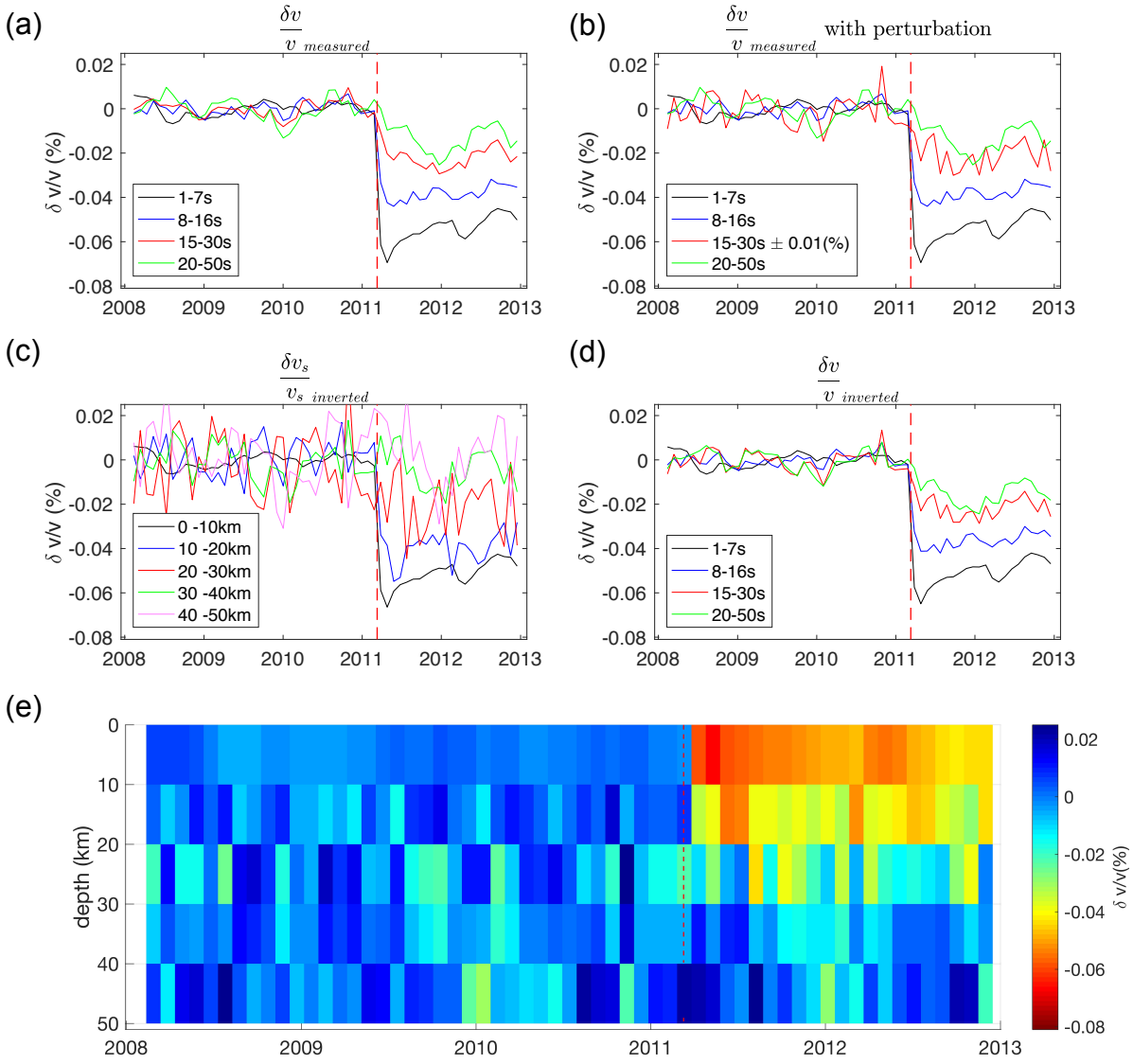

FIGURE 6.14 – (a) Measured monthly seismic velocity changes in four period ranges. (b) Measured monthly seismic velocity changes in four period ranges after adding 0.01% random perturbation in 15–30 s period range. (c) Inverted monthly S waves velocity changes versus depth from 2008 to 2012. (d) Summation of the inverted seismic velocity changes (e) Inverted monthly S waves velocity changes from 2008 to 2012 down to 50 km at depth.

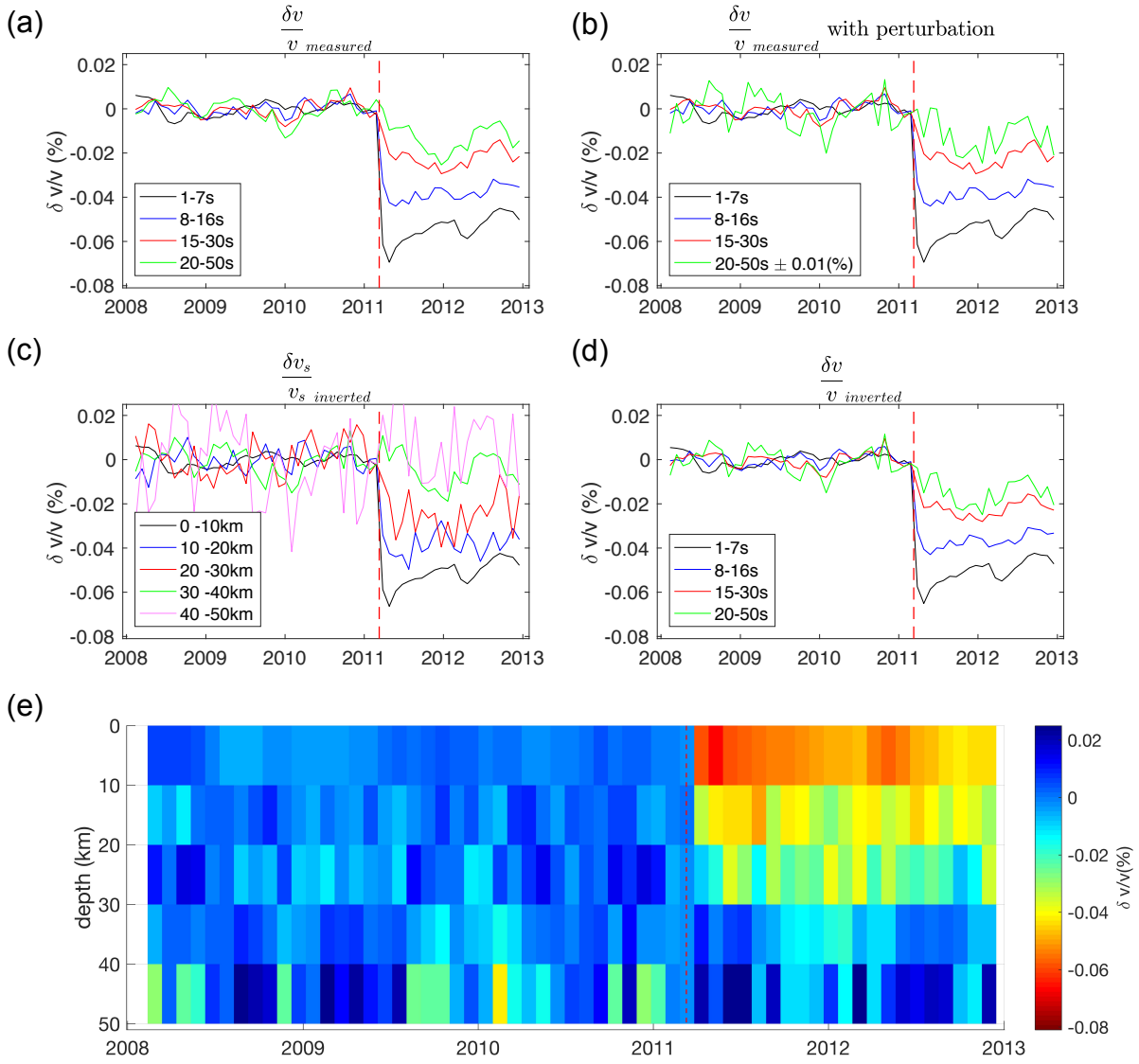

FIGURE 6.15 – (a) Measured monthly seismic velocity changes in four period ranges. (b) Measured monthly seismic velocity changes in four period ranges after adding 0.01% random perturbation in 20–50 s period range. (c) Inverted monthly S waves velocity changes versus depth from 2008 to 2012. (d) Summation of the inverted seismic velocity changes (e) Inverted monthly S waves velocity changes from 2008 to 2012 down to 50 km at depth.

6.6 Discussion

We focus on the Tohoku-oki earthquake related seismic velocity changes at different periods using Hi-net short period and tiltmeter data. Depth localization of velocity changes based on the Rayleigh waves sensitivity kernels helps better tracking both time- and depth-dependent crustal stress evolution. Because we use horizontal components with tiltmeter, we also check the inversion results based on the Love waves sensitivity kernels. The results in Fig. 6.16 show similar characteristics of S waves velocity changes versus depth. Coseismic velocity changes decrease with increasing depth. Delay of the maximum velocity drop increases with depth. However, seismic velocity changes in relatively long period ranges (15 – 30 s and 20 – 50 s) are not well recovered (Fig. 6.16 (e)) after inverted. As Love waves are more sensitive and concentrated to shallow depth in the crust. The located S waves velocity changes appear relatively shallow compared to that using Rayleigh waves sensitivity kernels, which usually have a maximum sampling depth of about one third of their wavelength.

It is important to note that all the inversion in this study is based on the assumption that the depth sensitivity of seismic velocity changes is dominated by surface waves sensitivity. But actually, we measure velocity changes of coda waves, which is considered to be multiple scattered waves that are caused by numerous heterogeneities distributed uniformly in the earth's crust. Coda waves consist at each time of a superposition of complex paths mixing P, S, and surface waves. Due to the scattering nature of coda waves, the wave paths are random and indeterminate. We are not able to assign trajectories to each arrival time, and it is difficult to locate the velocity changes.

The sensitivity of coda waves to a velocity change have been studied numerically by Obermann *et al.* (2013, 2016) to evaluate the roles played by body and surface waves. The authors report that the sensitivity of coda waves ($\mathbf{K}_c$) is the combination of the sensitivities of both surface waves ($\mathbf{K}_{sw}$) and bulk waves ($\mathbf{K}_{bw}$). $\mathbf{K}_{sw}$ is more important in the early coda, and bulk waves have an increasing importance in later coda. For long period, the transport mean free time $t^\star$ is large (100 s). Since we measure the velocity changes at around lapse time of 400 s at long periods. We are in the case of the early coda, where the sensitivity is dominated by the one of Rayleigh waves. With this proviso, $\mathbf{K}_c$ is controlled by $\mathbf{K}_{sw}$ in long period ranges. To be more precise, Obermann *et al.* (2013, 2016) prove that the sensitivities obey a relationship :

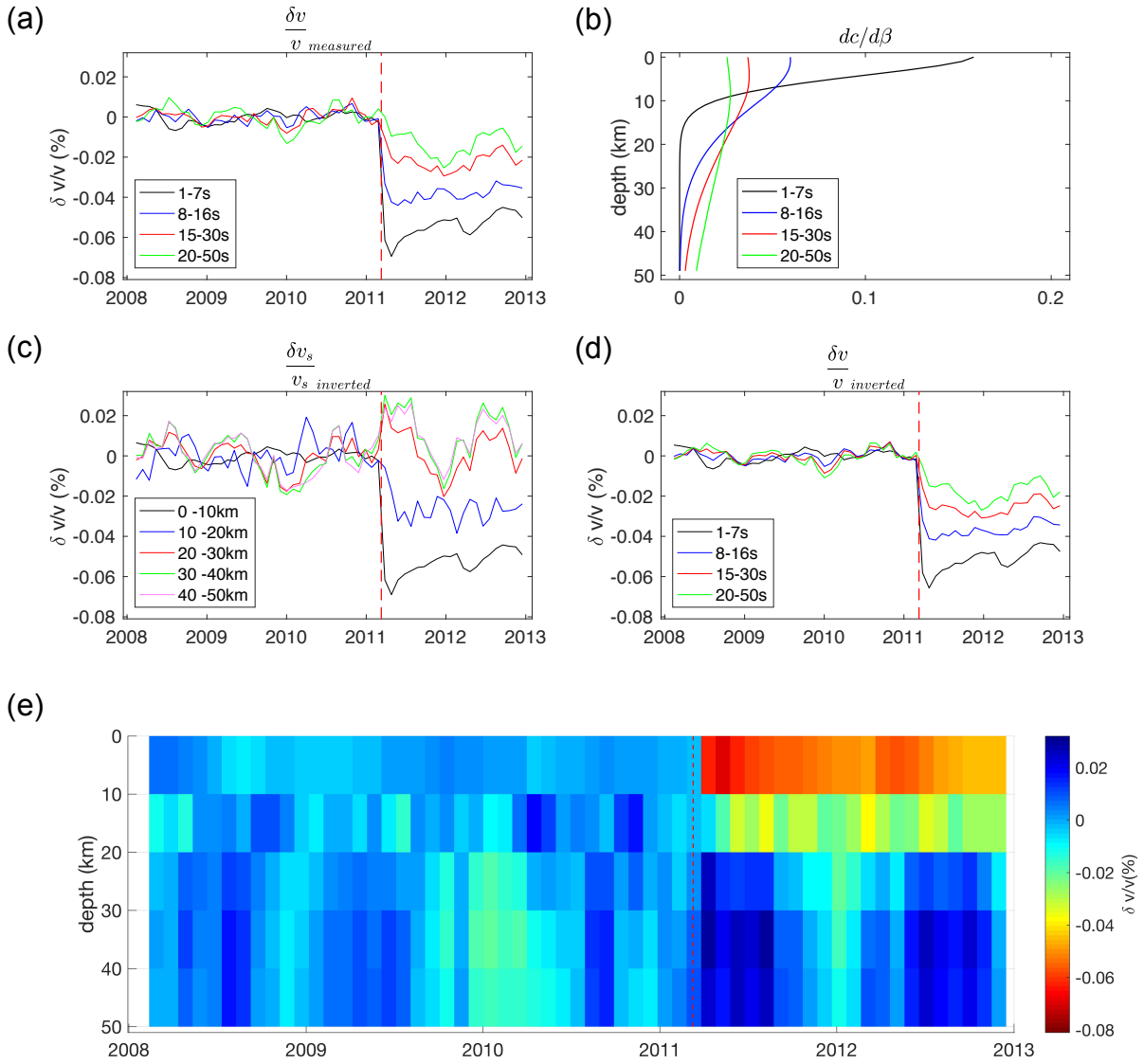

FIGURE 6.16 – (a) Measured monthly seismic velocity changes in four period ranges. (b) Normalized sensitivity kernels of Love waves to shear waves. (c) Inverted monthly S waves velocity changes versus depth from 2008 to 2012. (d) Summation of the inverted seismic velocity changes (e) Inverted monthly S waves velocity changes from 2008 to 2012 down to 50 km at depth.

$$\mathbf{K}_c = \alpha \mathbf{K}_{sw} + (1-\alpha)\mathbf{K}_{bw}, \tag{6.7}$$

where α is the partition coefficient. The estimation of the partition coefficients requires

numerical simulation. Fig. 6.17 shows the result of how partition coefficients change with normalized lapse time (normalized by mean free time $t^\star$). We can see the importance of $\mathbf{K}_{sw}$ for the first six mean free times and the increased importance of $\mathbf{K}_{bw}$ with growing time. This figure is confirming our choice of using surface waves sensitivities.

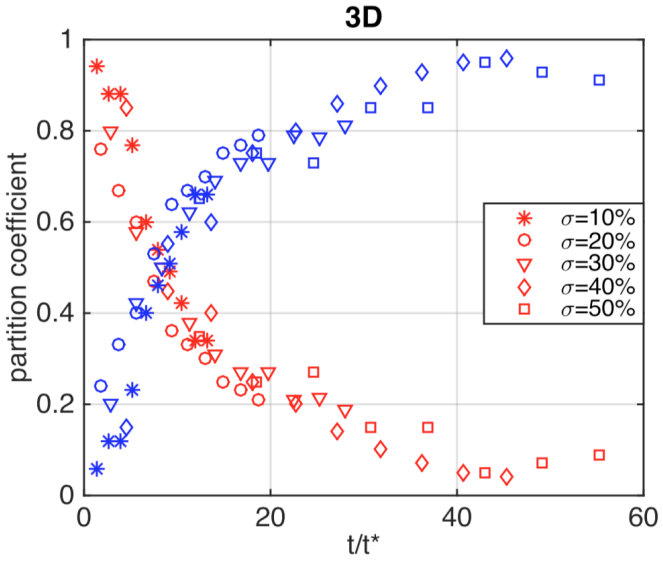

FIGURE 6.17 – Evolution of the partition coefficients for different degrees of heterogeneity ranging from 10% to 50% in the 3-D medium. The time axis has been normalized by the transport mean free time $t^\star = l^\star/\mathrm{c}$ ($l^\star$ is the transport mean free path). Displayed in red the partition coefficients α for the surface-wave sensitivity, and in blue $1-\alpha$ for the bulk-wave sensitivity. after Obermann *et al.* (2016)

Indeed $\alpha = 1$ in Eq. 6.7 is an extreme case. It means our measurement is made at very short normalized time, when $\mathbf{K}_c$ depends totally on the surface waves sensitivity kernels $\mathbf{K}_{sw}$.

It would be more precise to consider that for the coda waves that we use, the depth sensitivities depend on both sensitivities of surface and bulk waves. Since the precise values for $t^\star$ and α are not available, we will evaluate the implication of our hypothesis by considering the case of scattered body waves. We will see that with our hypothesis of surface waves is actually underestimating the depth of seismic velocity changes at relatively short periods.

In order to accurately evaluate the sensitivity of coda bulk waves, we need to calculate $\mathbf{K}_{bw}$ in terms of the probability of intensity P. We follow the 3-D $\mathbf{K}_{bw}$ sensitivity method by Obermann *et al.* (2013); Planès *et al.* (2014); Obermann *et al.* (2016) and start with

the definition of kernel $\mathbf{K}_{bw}$ by Pacheco et Snieder (2005) (Eq. 6.8) to calculate 3-D bulk sensitivity.

$$\mathbf{K}_{bw}\left(\mathbf{r}', \mathbf{r}, \mathbf{s}, t\right) = \frac{1}{P\left(\mathbf{r}, \mathbf{s}, t\right)} \int_0^t P\left(\mathbf{r}, \mathbf{r}', t - t'\right) P\left(\mathbf{r}', \mathbf{s}, t'\right) dt', \tag{6.8}$$

where P describes the probability of intensity of a pulse of energy that propagates through the medium at the distance $\mathbf{r}'$ ($\mathbf{r}' = \mathbf{r}$ at the receiver) and at time t. The approximate solution of intensity propagator to a diffusion equation solution in 3D can be expressed as Eq. 6.9.

$$P\left(\mathbf{s}, \mathbf{r}, t\right) = \frac{1}{\left(4\pi D t\right)^{d/2}} \exp\left(\frac{-|\mathbf{r} - \mathbf{s}|^2}{4Dt}\right), \tag{6.9}$$

where D represents the diffusion constant and equal to $\frac{cl^\star}{d}$. d is dimension, which is equal to 3 when in 3-D. This is an analytical solution that can be used for calculating the Kernel sensitivity. The intensity propagator can be also represented as the solution of radiative transfer equation. (Paasschens, 1997) as an interpolation of the 2-D and 4-D analytic solution (Planès *et al.*, 2014). Unlike the diffusion propagator, which is valid only when time t is much larger than the transport mean free time $t^\star$, which is equal to $l^\star/c$, where $l^\star$ is the transport mean free path, the radiative transfer solution has a general validity at all lapse times Planès *et al.* (2014); Obermann *et al.* (2016).

c is energy velocity and is determined by the equipartition state. As lapse time increases, the total energy of P- and S- wave modes reach stable so-called equipartition state. The energy ratio between S- and P-waves is $\frac{E_s}{E_p}$ and is represented by x. The total energy can be express as :

$$\begin{aligned} E &= E_p + E_s = E_p + xE_p \\ E &= \frac{E}{1+x} + \frac{x}{1+x}E. \end{aligned} \tag{6.10}$$

For elastic wave scattering, the energy ratio x is $2\gamma_0^3$, where γ_0 is the velocity ratio and $\equiv \alpha_0/\beta_0$. The velocity c is finally determined by a weighted average according to equation 6.11 by taking the theoritical equipartition ratio as 10.4, when $\gamma_0 = \sqrt{3}$ for a Poisson solid (Weaver, 1982; Margerin *et al.*, 2000) for further calculation.

$$\frac{1}{c} = \frac{1}{\beta_0}\frac{1}{(1+x)} + \frac{1}{\alpha_0}\frac{x}{(1+x)}. \tag{6.11}$$

The total travel time in 3-D over the volume V can be expresses as (Pacheco et Snieder, 2005) :

$$t = \int_V \mathbf{K}_{bw}\left(\mathbf{r}', \mathbf{r}, \mathbf{s}, t\right) dV\left(\mathbf{r}'\right) \tag{6.12}$$

The perturbation of travel time δt can be expressed as :

$$\delta t = \int_V \mathbf{K}_{bw}\left(\mathbf{r}', \mathbf{r}, \mathbf{s}, t\right) \frac{\delta s_l}{s_l}\left(\mathbf{r}'\right) dV\left(\mathbf{r}'\right), \tag{6.13}$$

where s_l is slowness. We can replace the left side of Eq. 6.13 by $\delta t = -\frac{\delta v}{v}_{bw} t$. As the slowness perturbation $\frac{\delta s_l}{s_l}(\mathbf{r}') = -\frac{\delta v}{v}(\mathbf{r}')$, so the equation can be written like :

$$-\frac{\delta v}{v}_{bw} t = -\int_V \mathbf{K}_{bw}\left(\mathbf{r}', \mathbf{r}, \mathbf{s}, t\right) \frac{\delta v}{v}\left(\mathbf{r}'\right) dV\left(\mathbf{r}'\right), \tag{6.14}$$

In case of homogeneous velocity changes $\frac{\delta v}{v}$ in each layer of volume V_i from surface to deep, then the measured bulk waves velocity changes $\frac{\delta v}{v}_{bw}$ can be expressed as the sum of the integral of velocity perturbation over all (i) elementary volume $dV(z_i)$ in depth. We assume that in each layer of volume V_i, the velocity perturbation $\frac{\delta v}{v}(z_i)$ is a constant. In each layer, there is an integral over dV_i

$$\frac{\delta v}{v}_{bw} = \sum_i \int_{V_i} \frac{\mathbf{K}_{bw}(z_i)}{t} \frac{\delta v}{v}(z_i) dV_i, \tag{6.15}$$

Thus, the bulk seismic velocity changes velocity is the summation of perturbation $\frac{\delta v}{v}(z_i)$ multiplied by the weight that is given by the sensitivity kernel in each layer over the total travel time.

We use the 3-D sensitivity equation by Planès *et al.* (2014); Obermann *et al.* (2016) based on the approximate analytic solution (Paasschens, 1997) of radiative transfer equation to evaluate the theoretical depth sensitivity of bulk waves velocity changes $\frac{\delta v}{v}_{bulk}$. We take

the energy velocity c (mixed P and S waves) as 3.89 km/s according to the formula 6.9 and the inter-distance of source and receiver as 50 km. Assuming the velocity perturbation $\frac{\delta v}{v}(z_i)$ is 1 in 1 km layer ($dV(z_i)$) down to 100 km at depth, we compute the sensitivity $\mathbf{K}$ by testing different scattering mean free paths l (km) and lapse time t (s) in the coda diffusion. Fig. 6.18 gives normalized depth sensitivity of bulk waves velocity changes $\frac{\delta v}{v}_{bulk}$ with various combinations of l and t. We take the mean free path similar to the orders of magnitude estimated by Sato (1978) and Aki et Chouet (1975) at different frequencies in Japan.

From the result, we can observe that when taking mean free path as 10 km for short period measurement, bulk waves are more sensitive to the upper crust. However the penetrating depth is already deeper than surface waves sensitivity kernels. And the sensitivity gets deeper with increasing lapse time in the coda. This illustrates the conclusion that bulk waves are more important in later coda. When using longer and more realistic mean free paths equal to 100 km and 1000 km considered for long period measurement, the depth sensitivities of bulk waves are more sensitive to the deep part than using 10 km mean free path. All sensitivities are quite similar and have a non-negligible important portion at more than 40 km at depth. This is very different from the surface wave sensitivity kernels, of which the sensitivity decreases rapidly with depth.

Therefore, for the bulk waves, the depth sensitivities have more weight at greater depth than considering solely surface waves. The inverted results in the deep should take more proportion. We measure the seismic velocity changes till 400 s for tiltmeter data at relatively long period. Thus, the inverted velocity changes would be deeper if we had considered bulk sensitivity than the current depth. Therefore, our measurements in 1 – 50 s period ranges should reflect the velocity changes at larger depth if bulk waves were considered. It should be pointed out that the assumption of surface waves sensitivity is actually underestimating the depth of the temporal changes in physical properties.

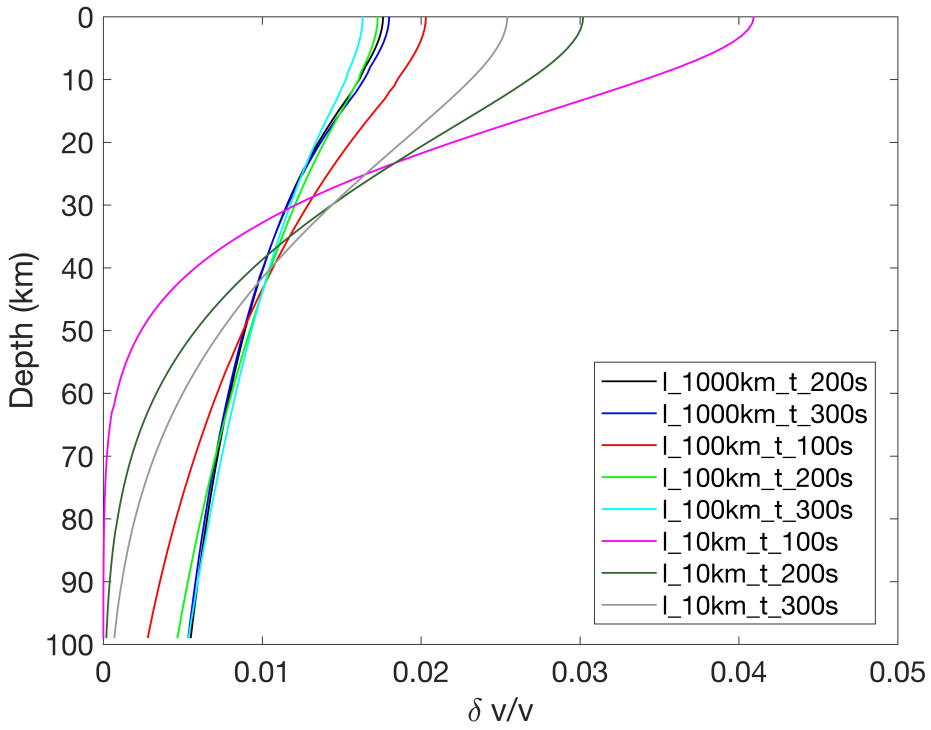

FIGURE 6.18 – Depth sensitivity of body waves with different lapse time t and scattering mean free path l for an area with length, width, and depth are respectively 1000 km, 1000 km and 100 km and for a total velocity changes = 1.

We want to understand the physical processes that control the depth-dependent seismic velocity changes, especially for the delayed postseismic response at depth.

For seismic velocity changes at shallow depth, seismic velocity changes are controlled by the dynamic perturbations from the earthquake. The instantaneous coseismic drop followed by a long-term postseismic relaxation can be explained by the processes referred to as fast and slow dynamics in laboratory experiments. A physical model is proposed by Sens-Schönfelder *et al.* (2018). The model consists of a material having structures which are broken by shear deformation and closed by some chemo-physical process with a series of characteristics time scales.

Explanation of the delayed seismic response should be referred to geodetic observations. Postseismic deformation of Tohoku-oki earthquake has been widely studied based on both onland and offshore GPS observations and numerical modeling. Sun *et al.* (2014); Watanabe *et al.* (2014) consider postseismic deformation is controlled by viscoelastic relaxation in the lower crust. Ozawa *et al.* (2011); Uchida et Matsuzawa (2013) propose that the deformation is dominated by afterslip which occurred deeper than the coseismic slip, while (Yamagiwa *et al.*, 2015; Hu *et al.*, 2016; Freed *et al.*, 2017) suggest the combined effects from both viscoelastic relaxation and afterslip. Freed *et al.* (2017) explain the postseismic displacements, vertical and horizontal, on-land and offshore, using the combined model of afterslip and viscoelasticity with depth-dependent layered viscosity. All these studies show extension beneath the continental crust following the big earthquake. The extension itself may lead up to the weakening of the crust, thus decreasing of the seismic velocity. Also, extension enables the rise of fluid under the lithostatic pressure at depth. The fluid diffusion process can also conduct to the continuing seismic velocity changes after the earthquake. Nakajima et Uchida (2018) point out that there is repeated fluid transfer from megathrusts. The fluid induced pore pressure may reduce the frictional strength of the megathrust and may be an additionally crucial part enhancing weakening of the megathrust during the slow slip episodes. The transfer of fluid arising from the hydrated slab can reduce seismic velocity from the lower crust to the subsurface. It could be an important factor that in charge of the delayed response at great depth. Similar to GPS observations, the seismic response is also subject to combined effects of viscoelastic deformation from lower crust, afterslips that occur in the following months after the mainshock in the deeper crust than coseismic deformation, as well as fluid drainage during the slow slip events. Even though, an absence of obvious evidence does not allow for determining uniquely the primary cause of the depth-dependent seismic

velocity changes and delayed response.

6.7 Conclusion

We verify for the first time that tiltmeter recordings can be regarded as broad band seismometers and can be used to monitor the seismic velocity changes at different periods. This is also the first time for a monitoring at long period up to 50 s. The results of different frequency bands provide us with a good opportunity to study the temporal evolution of depth-dependent seismic velocity changes in the whole crust. A comprehensive analysis in spatio-temporal scale helps us to better unveil the 2011 Tohoku-oki earthquake-related co- and post-earthquake stress recovery processes.

Distribution of strong velocity decreases at short periods are limited to the areas with strong ground shaking induced by the M_w 9.0 Tohoku-oki earthquake, while the long period velocity changes correlate well with modeled static strain induced by both viscoelastic deformation and fault slip.

Temporal evolution of velocities changes in different period ranges shows very different seismic responses. The amplitudes of coseismic velocity changes decrease with increasing periods. The velocity changes at greater periods are delayed in time with respect to the date of the earthquake. Using the sensitivity kernels of different period bands of the Rayleigh surface wave, we localize the S waves velocity changes down to 50 km at depth into five layers. Strong velocity changes are mainly concentrated within 10 km. The intensity of the velocity change decreases with increasing depth. Delayed response increases with depth.

Seismic velocity changes at depth are very different from the changes in shallow layers. Seismic velocity changes in shallow layers are dominated by the dynamic perturbations from the earthquake. Based on some current geodesic studies, we suggest that the delayed seismic velocity decrease could find its origins in both the visco-elastic response of the crust to large strain changes or a complex response of crustal seismic velocities to transient deformation like fluid transfer through the crust. But the exact physical meaning of this delay should be further explained. This may help to unravel this megathrust earthquake related physical processes.

Conclusions et perspectives

With the development of noise cross-correlation, traditional seismic methods need no longer to rely on earthquake events. We can construct the Green's function through noise cross-correlations. The reconstruction of Green's function not only covers any location but also has temporal continuity. The property of temporal continuity makes possible a new noise monitoring technology, which has rapidly developed and has been increasingly used in the past decade. Noise monitoring can track the evolution of physical properties of underground media by measuring changes in seismic wave velocity. This has been especially done for the changes in the subsurface medium before and after some large earthquakes.

In this thesis, we mainly focus on the study of seismic wave velocity changes throughout Japan and the physical processes responsible for these changes. The choice of Japan is justified by the density and the quality of the seismometers and tilt meters network, Besides, we eventually focus on the 2011 M_w 9.0 Tohoku-oki Earthquake to explore the characteristics of velocity changes before and after one of the largest earthquake ever recorded, and the evolution of the postseismic recovery process.

This thesis consists of three main parts :

The first part is devoted to the theoretical demonstration of the feasibility of reconstructing the Green's function from ambient seismic noise. We start from the elastic wave equation and show the full solution of the Green's function. Then, we review the reconstruction of the Green's function under different conditions, including acoustic waves and elastic waves from 1D to 3D. We try a numerical simulation using an accurate velocity model in Hokkaido. The simulated results show the equivalence between the Green's function and the derivatives of cross-correlation functions. We also discuss the possible dependence of noise monitoring on the assumption that the distribution of noise sources

is not ideally isotropic.

We introduced the main applications of noise cross-correlation, including the origins of noise, body wave extraction, noise-based tomography, and noise-based monitoring. We emphasized the last application, the noise-based monitoring, which is also the substance of this thesis. In this application, we introduce the origins of seismic velocity changes and three monitoring basic methods differed in time and frequency domains. In the whole research, we adopt the third one : doublet + inversion method, which is proved to be the most precise method so far. We show in detail how to use this method and some monitoring results in single stations. We also mention some possible improvements, including stacking, filtering, and C3, etc., which can optimize the noise-based monitoring, but require more computational time.

In **the second part**, we start to apply noise-based monitoring to the Hi-net data throughout Japan. We study the transient changes of seismic wave velocity in the crust caused by environmental perturbations. The emphasis of this part of the thesis is to analyze the annual signals in different regions and identify the related environmental factors. The impacts of environmental seasonal perturbations to crustal deformation are usually tracked and discussed based on geodetic observations. Recently, ambient seismic noise-based monitoring provides new insights into the continuous deformation in the crust as revealed by the temporal seismic velocity changes. In this study, we perform massive data analysis of the continuous seismic records of the very dense Hi-net short-period network (718 stations) in an active tectonic region. We measure the seismic velocity changes in the frequency range of 0.15 - 0.9 Hz from 2008 to 2012 throughout Japan. Strong seasonal effects are identified in the whole Kyushu, northeastern Hokkaido, and the west coast side along the Sea of Japan. Transient seasonal crustal drops of seismic velocity in Kyushu are well explained by a model of pore pressure increase induced by heavy precipitation in summer during typhoon period. In the Northeastern Hokkaido, seasonal signals are controlled by both effects of increased pore pressure during precipitation in summer (velocity decrease) and of closure of crustal cracks in winter (velocity increase) affected by both snow loading and pore pressure decrease by water drainage. The response of the crust in western coastal side is more enigmatic as it shows a very small sensitivity to either precipitation or snow loads effects but correlates well to the changes of sea surface height along the Sea of Japan. Finally, we show how better understanding these environmentally induced crustal perturbations improves the observations of

tectonic-induced seismic property changes. We build a linear relationship based on snow depth, pore pressure changes, and sea level changes to reconstruct the annual pattern and correct the seasonal effects. The minimum detectable seismic velocity relative change is down to 10^{-5} after correction and the corrected time series are more legible for long-term changes tracking. This is favorable for studying earthquakes related seismic velocity changes and the postseismic relaxation.

We compare the seismic velocity changes and GRACE measured gravity field (represented by equivalent water height, EWH) with the same spatial scale. The comparison between the two series of velocity changes and GRACE shows that the velocity variations at regional scale has an origin into physical process in the Earth. Further comparison with GPS measured vertical displacement for each station show that GPS vertical component is however more sensible to the subsidence from precipitation than to pore pressure changes. For the stations along the western side of Honshu and Hokkaido, both GPS and seismic velocity show a positive correlation with sea level changes.

The third part consists of the study of the mechanical response of the crust to large earthquakes. This provides unique insight into the processes of deformation in preparation for future earthquakes. Noise-based seismic velocity monitoring can directly probe continuously in time the mechanical state of the crust at depth. In this work, we study the response of the crust to the M_w 9.0, 2011 Tohoku-oki earthquake. In addition to the Hi-net short period sensors, we employ here for the first time for the noise-based monitoring with the very dense network of Hi-net tilt meters as long period (8 – 50 s) seismometers to sample the crust below 5 km and down to 50 km at depth in different period bands. Velocity changes at different periods show great differences. Spatial distribution of strong velocity decreases at short periods resamples the map of strong ground shaking produced by the 2011 Tohoku-oki earthquake, while the long period velocity changes correlate well with the static strain computed in a model including viscoelastic relaxation and afterslip at depth, and constrained by GPS observations. These observations indicate that the variations at depth are not a spurious effect of changes in the shallow layers.

We invert the seismic velocity changes in different period bands into depth-dependent velocity changes based on the surface waves sensitivity kernels, which may underestimate the actual depth of changes. This underestimation has been discussed based on the 3-D bulk waves sensitivity which is another contributor of coda waves sensitivity, that is

expected to be small in our condition of measurement at long periods. We therefore invert our measurements for a depth dependent velocity changes with surface wave kernels. The inverted results show that coseismic velocity drops diminish with increasing depth. Strong seismic velocity changes are observed in shallow layers and recover immediately after the main shock. The temporal evolution of velocity changes at different depths shows that the maximum drops of velocity at greater depth are delayed with respect to the date of the earthquake. This delayed response could have implications for constraining the response of the crust in terms of both the visco-elastic response of the crust to large strain changes or a complex response of crustal seismic velocities to transient fluid flow.

There are some important conclusions that can be drawn from this study :

Noise-based seismic monitoring offers the possibility of continuous monitoring of underground physical properties with high temporal resolution (from hourly to monthly). This helps understanding the evolution of physical properties under the impacts of different forcing and transient disturbances, and of tectonics processes.

Seismic velocity changes in shallow layers are affected by some surrounding environmental factors, such as precipitation-induced pore pressure changes, and loading effects from both snow depth and sea level. The transient seasonal changes show strong regional differences and can be well correlated with the local geodetic observations such as GPS vertical displacement and GRACE gravity field measurement. The combination of these observations can provide a better explanation of leading causes for the regional-dependent seasonal seismic velocity changes.

Tohoku-oki earthquake-related seismic velocity changes are depth-dependent, which illuminates that the responsible physical processes vary with depth. Seismic velocity changes in shallow layers can be explained by the dynamic perturbation waves from the earthquake. The delayed changes at long periods may imply some nonelastic response at depth or deep fluid. In particular, the postseismic transient decreases of seismic velocity observed in all period ranges at the beginning of 2012 may result from the transfer of fluid arising from the hydrated slab to the subsurface due to the permeability-altering by extension following the mainshock.

Perspectives

The progress of ambient seismic noise cross-correlation has promoted the development of 3D surface and body waves imaging in both regional and global scales. In the field of noise-based monitoring, the ballistic waves monitoring will improve the spatial resolution of monitoring compared to coda waves and will be expected to become an important aspect of monitoring. In addition, the study of crustal and upper mantle anisotropy and the scattering properties in the earth will be further developed.

For noise-based monitoring, we will achieve in the future 4D imaging of the earth at depth and continuously in time. This will greatly enhance our understanding of the evolution of the earth's crust with daily/monthly time resolution. The big earthquake-related co- and post- seismic velocity changes can help building physical models to simulate the evolution of the crust around seismic faults. The systematic analysis of seismic velocity changes combined with other geodetic methods will lead us to better monitor and locate the seismicity.

Bibliographie

Aki, K. (1957). Space and time spectra of stationary stochastic waves, with special reference to microtremors. *Bull. Earthq. Res. Inst.*, 35:415–456.

Aki, K. et Chouet, B. (1975). Origin of coda waves : Source, attenuation, and scattering effects. *Journal of Geophysical Research*.

Aki, K. et Richards, P. G. (2002). *Quantitative seismology*.

Bawden, G. W., Thatcher, W., Stein, R. S., Hudnut, K. W. et Peltzer, G. (2001). Tectonic contraction across Los Angeles after removal of groundwater pumping effects. *Nature*.

Ben-Zion, Y. et Leary, P. (1986). Thermoelastic strain in a half-space covered by unconsolidated material. *Bulletin of the Seismological Society of America*, 76(5):1447–1460.

Bensen, G. D., Ritzwoller, M. H., Barmin, M. P., Levshin, A. L., Lin, F., Moschetti, M. P., Shapiro, N. M. et Yang, Y. (2007). Processing seismic ambient noise data to obtain reliable broad-band surface wave dispersion measurements. *Geophysical Journal International*, 169(3):1239–1260.

Berger, J. (1975). A note on thermoelastic strains and tilts. *Journal of Geophysical Research*.

Bevis, M., Alsdorf, D., Kendrick, E., Fortes, L. P., Forsberg, B., Smalley, R. et Becker, J. (2005). Seasonal fluctuations in the mass of the Amazon River system and Earth's elastic response. *Geophysical Research Letters*.

Birch, F. (1961). The velocity of compressional waves in rocks to 10 kilobars : 2. *Journal of Geophysical Research*.

Bodin, T., Sambridge, M., Rawlinson, N. et Arroucau, P. (2012a). Transdimensional tomography with unknown data noise. *Geophysical Journal International*.

Bodin, T., Sambridge, M., Tkalćić, H., Arroucau, P., Gallagher, K. et Rawlinson, N. (2012b). Transdimensional inversion of receiver functions and surface wave dispersion. *Journal of Geophysical Research : Solid Earth*.

Bonnefoy-Claudet, S., Cotton, F. et Bard, P. Y. (2006). The nature of noise wavefield and its applications for site effects studies. A literature review. *Earth-Science Reviews*.

Boué, P., Poli, P., Campillo, M., Pedersen, H., Briand, X. et Roux, P. (2013). Teleseismic correlations of ambient seismic noise for deep global imaging of the Earth. *Geophysical Journal International*.

Brenguier, F., Campillo, M., Hadziioannou, C., Shapiro, N. M., Nadeau, R. M. et Larose, E. (2008a). Postseismic relaxation along the San Andreas fault at Parkfield from continuous seismological observations. *Science*, 321(5895):1478–1481.

Brenguier, F., Campillo, M., Takeda, T., Aoki, Y., Shapiro, N. M., Briand, X., Emoto, K. et Miyake, H. (2014). Mapping pressurized volcanic fluids from induced crustal seismic velocity drops. *Science*, 345(6192).

Brenguier, F., Clarke, D., Aoki, Y., Shapiro, N. M., Campillo, M. et Ferrazzini, V. (2011). Monitoring volcanoes using seismic noise correlations. *Comptes Rendus - Geoscience*, 343(8-9):633–638.

Brenguier, F., Shapiro, N. M., Campillo, M., Ferrazzini, V., Duputel, Z., Coutant, O. et Nercessian, A. (2008b). Towards forecasting volcanic eruptions using seismic noise. *Nature Geoscience*, 1(2):126–130.

Brenguier, F., Shapiro, N. M., Campillo, M., Nercessian, A. et Ferrazzini, V. (2007). 3-D surface wave tomography of the Piton de la Fournaise volcano using seismic noise correlations. *Geophysical Research Letters*.

Campillo, M. (2006). Phase and correlation in 'random' seismic fields and the reconstruction of the green function. *Pure and Applied Geophysics*, 163(2-3):475–502.

Campillo, M. et Paul, A. (2003). Long-Range Correlations in the Diffuse Seismic Coda. *Science*, 299(5606):547–549.

Chávez-García, F. J. et Luzón, F. (2005). On the correlation of seismic microtremors. *Journal of Geophysical Research : Solid Earth*.

Chelton, D. B. et Enfield, D. B. (1986). Ocean signals in tide gauge records. *Journal of Geophysical Research*, 91:9081–9099.

Chen, J. H., Froment, B., Liu, Q. Y. et Campillo, M. (2010). Distribution of seismic wave speed changes associated with the 12 May 2008 Mw 7.9 Wenchuan earthquake. *Geophysical Research Letters*.

Chen, M., Huang, H., Yao, H., Van Der Hilst, R. et Niu, F. (2014). Low wave speed zones in the crust beneath SE Tibet revealed by ambient noise adjoint tomography. *Geophysical Research Letters*.

Chen, Y., Hu, J. et Peng, F. (2018). Seismological challenges in earthquake hazard reductions : reflections on the 2008 Wenchuan earthquake. *Science Bulletin*.

Claerbout, J. F. (1968). Synthesis of a layered medium from its acoustic transmission response. *GEOPHYSICS*.

Clarke, D., Zaccarelli, L., Shapiro, N. M. et Brenguier, F. (2011). Assessment of resolution and accuracy of the Moving Window Cross Spectral technique for monitoring crustal temporal variations using ambient seismic noise. *Geophysical Journal International*.

Colombi, A., Chaput, J., Brenguier, F., Hillers, G., Roux, P. et Campillo, M. (2014). On the temporal stability of the coda of ambient noise correlations. *Comptes Rendus - Geoscience*, 346(11-12):307–316.

Daskalakis, E., Evangelidis, C. P., Garnier, J., Melis, N. S., Papanicolaou, G. et Tsogka, C. (2016). Robust seismic velocity change estimation using ambient noise recordings. *Geophysical Journal International*.

Denolle, M. A., Dunham, E. M., Prieto, G. A. et Beroza, G. C. (2013). Ground motion prediction of realistic earthquake sources using the ambient seismic field. *Journal of Geophysical Research : Solid Earth*.

Donn, W. L. (1966). Microseisms. *Earth-Science Reviews*, 1(2-3):213–230.

Draganov, D. S., Wapenaar, K., Mulder, W., Singer, J. et Verdel, A. (2007). Retrieval of reflections from seismic background-noise measurements. *Geophysical Research Letters*.

Duvall, T. L., Jefffries, S. M., Harvey, J. W. et Pomerantz, M. A. (1993). Time-distance helioseismology. *Nature*.

Fang, H., Yao, H., Zhang, H., Huang, Y. C. et Van Der Hilst, R. D. (2015). Direct inversion of surface wave dispersion for three-dimensional shallow crustal structure based on ray tracing : Methodology and application. *Geophysical Journal International*.

Fichtner, A. (2014). Source and processing effects on noise correlations.

Fichtner, A. (2015). Source-structure trade-offs in ambient noise correlations. *Geophysical Journal International*.

Freed, A. M., Ali, S. T. et Bürgmann, R. (2007). Evolution of stress in Southern California for the past 200 years from coseismic, postseismic and interseismic stress changes. *Geophysical Journal International*, 169(3):1164–1179.

Freed, A. M., Bürgmann, R., Calais, E., Freymueller, J. et Hreinsdóttir, S. (2006). Implications of deformation following the 2002 Denali, Alaska, earthquake for postseismic relaxation processes and lithospheric rheology. *Journal of Geophysical Research : Solid Earth*, 111(1):1–23.

Freed, A. M., Hashima, A., Becker, T. W., Okaya, D. A., Sato, H. et Hatanaka, Y. (2017). Resolving depth-dependent subduction zone viscosity and afterslip from postseismic displacements following the 2011 Tohoku-oki, Japan earthquake. *Earth and Planetary Science Letters*, 459:279–290.

Friedrich, A., Krüger, F. et Klinge, K. (1998). Ocean-generated microseismic noise located with the Gräfenberg array. *Journal of Seismology*.

Froment, B., Campillo, M., Chen, J. H. et Liu, Q. Y. (2013). Deformation at depth associated with the 12 May 2008 MW 7.9 Wenchuan earthquake from seismic ambient noise monitoring. *Geophysical Research Letters*.

Froment, B., Campillo, M., Roux, P., Gouédard, P., Verdel, A. et Weaver, R. L. (2010). Estimation of the effect of nonisotropically distributed energy on the apparent arrival time in correlations. *Geophysics*.

Fukushima, Y., Toda, S., Miura, S., Ishimura, D., Fukuda, J., Demachi, T. et Tachibana, K. (2018). Extremely early recurrence of intraplate fault rupture following the Tohoku-Oki earthquake. *Nature Geoscience*.

Gao, H. et Shen, Y. (2014). Upper mantle structure of the Cascades from full-wave ambient noise tomography : Evidence for 3D mantle upwelling in the back-arc. *Earth and Planetary Science Letters*.

Gassenmeier, M., Sens-Schönfelder, C., Eulenfeld, T., Bartsch, M., Victor, P., Tilmann, F. et Korn, M. (2016). Field observations of seismic velocity changes caused by shaking-induced damage and healing due to mesoscopic nonlinearity. *Geophysical Journal International*, 204(3):1490–1502.

Gómez-García, C., Brenguier, F., Boué, P., Shapiro, N. M., Droznin, D. V., Droznina, S. Y., Senyukov, S. L. et Gordeev, E. I. (2018). Retrieving robust noise-based seismic velocity changes from sparse data sets : synthetic tests and application to Klyuchevskoy volcanic group (Kamchatka). *Geophysical Journal International*, 214(2): 1218–1236.

Grapenthin, R., Sigmundsson, F., Geirsson, H., Árnadóttir, T. et Pinel, V. (2006). Icelandic rhythmics : Annual modulation of land elevation and plate spreading by snow load. *Geophysical Research Letters*, 33(24).

Gutenberg, B. (1958). Microseisms. *Advances in Geophysics*, 5:53–92.

Hadziioannou, C., Larose, E., Baig, A., Roux, P. et Campillo, M. (2011). Improving temporal resolution in ambient noise monitoring of seismic wave speed. *Journal of Geophysical Research : Solid Earth*, 116(7).

Hadziioannou, C., Larose, E., Coutant, O., Roux, P. et Campillo, M. (2009). Stability of Monitoring Weak Changes in Multiply Scattering Media with Ambient Noise Correlation : Laboratory Experiments.

Haned, A., Stutzmann, E., Schimmel, M., Kiselev, S., Davaille, A. et Yelles-Chaouche, A. (2016). Global tomography using seismic hum. *Geophysical Journal International*.

Haubrich, R. A., Munk, W. H. et Snodgrass, F. E. (1963). Comparative spectra of microseisms and swell. *Bulletin of the Seismological Society of America*.

Heki, K. (2001). Seasonal modulation of interseismic strain buildup in northeastern Japan driven by snow loads. *Science (New York, N.Y.)*, 293(5527):89–92.

Heki, K. (2003). Snow load and seasonal variation of earthquake occurrence in Japan. *Earth and Planetary Science Letters*.

Heki, K. (2004). Dense GPS array as a new sensor of seasonal changes of surface loads. *In Geophysical Monograph Series*.

Heki, K. (2007). 16. Secular, Transient, and Seasonal Crustal Movements in Japan from a Dense GPS Array Implication for Plate Dynamics in Convergent Boundaries. *In The Seismogenic Zone of Subduction Thrust Faults*.

Herring, T., King, R., Mcclusky, S. et Sciences, P. (2010). Introduction to GAMIT/GLOBK. *October*.

Hillers, G., Ben-Zion, Y., Campillo, M. et Zigone, D. (2015a). Seasonal variations of seismic velocities in the San Jacinto fault area observed with ambient seismic noise. *Geophysical Journal International Geophys. J. Int*, 202(2):920–932.

Hillers, G., Campillo, M. et Ma, K. F. (2014). Seismic velocity variations at TCDP are controlled by MJO driven precipitation pattern and high fluid discharge properties. *Earth and Planetary Science Letters*, 391:121–127.

Hillers, G., Graham, N., Campillo, M., Kedar, S., Landés, M. et Shapiro, N. (2012). Global oceanic microseism sources as seen by seismic arrays and predicted by wave action models. *Geochemistry, Geophysics, Geosystems*.

Hillers, G., Retailleau, L., Campillo, M., Inbal, A., Ampuero, J. P. et Nishimura, T. (2015b). In situ observations of velocity changes in response to tidal deformation from analysis of the high-frequency ambient wavefield. *Journal of Geophysical Research B : Solid Earth*, 120(1):210–225.

Hillers, G., Retailleau, L., Campillo, M., Inbal, A., Ampuero, J. P. et Nishimura, T. (2015c). In situ observations of velocity changes in response to tidal deformation from analysis of the high-frequency ambient wavefield. *Journal of Geophysical Research B : Solid Earth*, 120(1):210–225.

Hobiger, M., Wegler, U., Shiomi, K. et Nakahara, H. (2012). Coseismic and postseismic elastic wave velocity variations caused by the 2008 Iwate-Miyagi Nairiku earthquake, Japan. *Journal of Geophysical Research : Solid Earth*, 117(B9).

Hotovec-Ellis, A. J., Gomberg, J., Vidale, J. E. et Creager, K. C. (2014). A continuous record of intereruption velocity change at Mount St. Helens from coda wave interferometry. *Journal of Geophysical Research : Solid Earth*, 119(3):2199–2214.

Hu, Y., Bürgmann, R., Uchida, N., Banerjee, P. et Freymueller, J. T. (2016). Stress-driven relaxation of heterogeneous upper mantle and time-dependent afterslip following the 2011 Tohoku earthquake. *Journal of Geophysical Research B : Solid Earth*, 121(1):385–411.

Ishibashi, K. (2004). Status of historical seismology in Japan. *Annals of Geophysics*.

Johnson, C. W., Fu, Y. et Bürgmann, R. (2017). Stress Models of the Annual Hydrospheric, Atmospheric, Thermal, and Tidal Loading Cycles on California Faults : Perturbation of Background Stress and Changes in Seismicity. *Journal of Geophysical Research : Solid Earth*.

Johnson, P. et Sutin, A. (2005). Slow dynamics and anomalous nonlinear fast dynamics in diverse solids. *The Journal of the Acoustical Society of America*.

Khandelwal, D. D., Gahalaut, V., Kumar, N., Kundu, B. et Yadav, R. K. (2014). Seasonal variation in the deformation rate in NW Himalayan region. *Natural Hazards*.

Lawrence, J. F. et Prieto, G. A. (2011). Attenuation tomography of the western United States from ambient seismic noise. *Journal of Geophysical Research : Solid Earth*.

Lin, F. C. et Ritzwoller, M. H. (2011). Helmholtz surface wave tomography for isotropic and azimuthally anisotropic structure. *Geophysical Journal International*.

Lin, F. C., Ritzwoller, M. H. et Snieder, R. (2009). Eikonal tomography : Surface wave tomography by phase front tracking across a regional broad-band seismic array. *Geophysical Journal International*.

Lobkis, O. I. et Weaver, R. L. (2003). Coda-Wave Interferometry in Finite Solids : Recovery of P-toS- Conversion Rates in an Elastodynamic Billiard. *Physical Review Letters*.

Longuet-Higgins, M. S. (1950). A Theory of the Origin of Microseisms. *Philosophical Transactions of the Royal Society A : Mathematical, Physical and Engineering Sciences*.

Lu, Y., Stehly, L. et Paul, A. (2018). High-resolution surface wave tomography of the European crust and uppermost mantle from ambient seismic noise. *Geophysical Journal International*, 214(2):1136–1150.

Lubimova, E. A. et Magnitzky, V. A. (1964). Thermoelastic stresses and the energy of earthquakes. *Journal of Geophysical Research*, 69(16):3443–3447.

Luttrell, K. et Sandwell, D. (2010). Ocean loading effects on stress at near shore plate boundary fault systems. *Journal of Geophysical Research : Solid Earth*, 115(8).

Lyakhovsky, V., Hamiel, Y., Ampuero, J. P. et Ben-zion, Y. (2009). Non-linear damage rheology and wave resonance in rocks. *Geophysical Journal International*.

Lyakhovsky, V., Reches, Z., Weinberger, R. et Scott, T. E. (1997). Non-linear elastic behaviour of damaged rocks. *Geophysical Journal International*.

Mao, S., Campillo, M., van der Hilst, R. D. et Brenguier, F. (2018). High temporal resolution monitoring of small variations in crustal strain by dense seismic arrays. *Submitted to Geophysical Research Letter*.

Margerin, L., Campillo, M. et Van Tiggelen, B. (2000). Monte Carlo simulation of multiple scattering of elastic waves. *Journal of Geophysical Research*.

Matsubara, M., Sato, H., Uehira, K., Mochizuki, M. et Kanazawa, T. (2017). Three-dimensional seismic velocity structure beneath Japanese islands and surroundings based on NIED seismic networks using both inland and offshore events. *Journal of Disaster Research*.

Matsumoto, K., Sato, T., Fujimoto, H., Tamura, Y., Nishino, M., Hino, R., Higashi, T. et Kanazawa, T. (2006). Ocean bottom pressure observation off Sanriku and comparison with ocean tide models Altimetry and barotropic signals from ocean models. *Geophysical Research Letters*, 33(16):3–7.

Meier, U., Shapiro, N. M. et Brenguier, F. (2010). Detecting seasonal variations in seismic velocities within Los Angeles basin from correlations of ambient seismic noise. *Geophysical Journal International*, 181(2):985–996.

Minato, S., Tsuji, T., Ohmi, S. et Matsuoka, T. (2012). Monitoring seismic velocity change caused by the 2011 Tohoku-oki earthquake using ambient noise records. *Geophysical Research Letters*, 39(9):n/a–n/a.

Mitchum, G. T., Cheney, R., Fu, L.-L., Le Provost, C., Menard, Y. et Woodworth, P. (2001). The future of sea surface height observations. Rapport technique.

Moreau, L., Stehly, L., Boué, P., Lu, Y., Larose, E. et Campillo, M. (2017). Improving ambient noise correlation functions with an SVD-based Wiener filter. *Geophysical Journal International*.

Morimoto, A., Yanagi, T. et Kaneko, A. (2000). Tidal correction of altimetric data in the Japan Sea. *Journal of Oceanography*.

Munekane, H. (2009). On Improving Precision of GPS-derived Height Time Series at GEONET Stations. pages 39–46.

Nakahara, H. (2006). A systematic study of theoretical relations between spatial correlation and Green's function in one-, two- and three-dimensional random scalar wavefields. *Geophysical Journal International*.

Nakajima, J. et Uchida, N. (2018). Repeated drainage from megathrusts during episodic slow slip. *Nature Geoscience*.

Nakamura, F., Kameyama, S. et Mizugaki, S. (2004). Rapid shrinkage of Kushiro Mire, the largest mire in Japan, due to increased sedimentation associated with land-use development in the catchment. *In Catena*, volume 55, pages 213–229.

Nakata, N., Chang, J. P., Lawrence, J. F. et Boué, P. (2015). Body wave extraction and tomography at Long Beach, California, with ambient-noise interferometry. *Journal of Geophysical Research : Solid Earth*.

Nakata, N. et Snieder, R. (2012). Estimating near-surface shear wave velocities in Japan by applying seismic interferometry to KiK-net data. *Journal of Geophysical Research : Solid Earth*, 117(1).

Nishida, K. (2013). Global propagation of body waves revealed by cross-correlation analysis of seismic hum. *Geophysical Research Letters*.

Nishida, K., Kawakatsu, H., Fukao, Y. et Obara, K. (2008a). Background Love and Rayleigh waves simultaneously generated at the Pacific Ocean floors. *Geophysical Research Letters*.

Nishida, K., Kawakatsu, H. et Obara, K. (2008b). Three-dimensional crustal S wave velocity structure in Japan using microseismic data recorded by Hi-net tiltmeters. *Journal of Geophysical Research : Solid Earth*, 113(10).

Nishida, K., Montagner, J.-P. J.-P. et Kawakatsu, H. (2009). Global Surface Wave Tomography Using Seismic Hum. *Science*.

Nur, A. (1971). Effects of stress on velocity anisotropy in rocks with cracks. *Journal of Geophysical Research*.

Nur, A. et Simmons, G. (1969). Stress-induced velocity anisotropy in rock : An experimental study. *Journal of Geophysical Research*.

Obara, K., Kasahara, K., Hori, S. et Okada, Y. (2005). A densely distributed high-sensitivity seismograph network in Japan :Hi-net by National Research Institute for Earth Science and DisasterPrevention. *Review of Scientific Instruments*, 76(2):021301.

Obermann, A., Froment, B., Campillo, M., Larose, E., Planès, T., Valette, B., Chen, J. H. et Liu, Q. Y. (2014). Seismic noise correlations to image structural and mechanical changes associated with the Mw 7.9 2008 Wenchuan earthquake. *Journal of Geophysical Research : Solid Earth*.

Obermann, A., Planès, T., Hadziioannou, C. et Campillo, M. (2016). Lapse-time-dependent coda-wave depth sensitivity to local velocity perturbations in 3-D heterogeneous elastic media. *Geophysical Journal International*, 207(1):59–66.

Obermann, A., Planès, T., Larose, E. et Campillo, M. (2018). 4-D Imaging of Subsurface Changes with Coda Waves : Numerical Studies of 3-D Combined Sensitivity Kernels and Applications to the Mw 7.9, 2008 Wenchuan Earthquake. *Pure and Applied Geophysics*.

Obermann, A., Planès, T., Larose, E., Sens-Schönfelder, C. et Campillo, M. (2013). Depth sensitivity of seismic coda waves to velocity perturbations in an elastic heterogeneous medium. *Geophysical Journal International*, 194(1).

O'Connell, R. J. et Budiansky, B. (1974). Seismic velocities in dry and saturated cracked solids. *Journal of Geophysical Research*.

Okada, Y., Kasahara, K., Hori, S., Obara, K., Sekiguchi, S., Fujiwara, H. et Yamamoto, A. (2004). Recent progress of seismic observation networks in Japan - Hi-net, F-net, K-net and KiK-net -. *Earth, Planets and Space*, 56(8).

Ozawa, S., Nishimura, T., Suito, H., Kobayashi, T., Tobita, M. et Imakiire, T. (2011). Coseismic and postseismic slip of the 2011 magnitude-9 Tohoku-Oki earthquake. *Nature*, 475(7356):373–377.

Paasschens, J. (1997). Solution of the time-dependent Boltzmann equation. *Physical Review E*.

Pacheco, C. et Snieder, R. (2005). Time-lapse travel time change of multiply scattered acoustic waves. *The Journal of the Acoustical Society of America*.

Paul, A., Campillo, M., Margerin, L., Larose, E. et Derode, A. (2005). Empirical synthesis of time-asymmetrical Green functions from the correlation of coda waves. *Journal of Geophysical Research : Solid Earth*.

Planès, T., Larose, E., Margerin, L., Rossetto, V. et Sens-Schönfelder, C. (2014). Decorrelation and phase-shift of coda waves induced by local changes : Multiple scattering approach and numerical validation. *Waves in Random and Complex Media*.

Poli, P., Campillo, M. et Pedersen, H. (2012a). Body-wave imaging of Earth's mantle discontinuities from ambient seismic noise. *Science*, 338(6110):1063–1065.

Poli, P., Pedersen, H. A. et Campillo, M. (2012b). Emergence of body waves from cross-correlation of short period seismic noise. *Geophysical Journal International*.

Pollitz, F. F. (1992). Postseismic Relaxation Theory on the Spherical Earth. *Bulletin of the Seismological Society of America*, 82(1):422–453.

Pollitz, F. F. (2005). Transient rheology of the upper mantle beneath central Alaska inferred from the crustal velocity field following the 2002 Denali earthquake. *Journal of Geophysical Research : Solid Earth*.

Poupinet, G., Ellsworth, W. L. et Frechet, J. (1984). Monitoring velocity variations in the crust using earthquake doublets : An application to the Calaveras Fault, California. *Journal of Geophysical Research*, 89(B7):5719.

Prieto, G. A., Denolle, M., Lawrence, J. F. et Beroza, G. C. (2011). On amplitude information carried by the ambient seismic field. *Comptes Rendus - Geoscience*.

Reasenberg, P. et Aki, K. (1974). A precise, continuous measurement of seismic velocity for monitoring in situ stress. *J. Geophys. Res.*, 79(2):399–406.

Rhie, J. et Romanowicz, B. (2004). Excitation of Earth ' s continuous free oscillations by atmosphere – ocean – seafloor coupling. *Nature*.

Richter, T., Sens-Schönfelder, C., Kind, R. et Asch, G. (2014). Comprehensive observation and modeling of earthquake and temperature-related seismic velocity changes in northern Chile with passive image interferometry. *Journal of Geophysical Research : Solid Earth*, 119(6):4747–4765.

Rivet, D., Brenguier, F. et Cappa, F. (2015). Improved detection of preeruptive seismic velocity drops at the Piton de la Fournaise volcano. *Geophysical Research Letters*, 42(15):6332–6339.

Rivet, D., Campillo, M., Radiguet, M., Zigone, D., Cruz-Atienza, V., Shapiro, N. M., Kostoglodov, V., Cotte, N., Cougoulat, G., Walpersdorf, A. et Daub, E. (2013). Seismic velocity changes, strain rate and non-volcanic tremors during the 2009-2010 slow slip event in Guerrero, Mexico. *Geophysical Journal International*, 196(1):447–460.

Roux, P., Sabra, K. G., Gerstoft, P., Kuperman, W. A. et Fehler, M. C. (2005). P-waves from cross-correlation of seismic noise. *Geophysical Research Letters*, 32(19).

Saito, T. (2010). Love-wave excitation due to the interaction between a propagating ocean wave and the sea-bottom topography. *Geophysical Journal International*.

Sanchez-Sesma, F. J. et Campillo, M. (2006). Retrieval of the Green Function From Cross-Correlation : The Canonical Elastic Problem. *Bulletin of the Seizmological Society of America*.

Sato, H. (1978). Mean free path of S-waves under the Kanto district of Japan. *J. Phys. Earth*.

Sawazaki, K., Kimura, H., Shiomi, K., Uchida, N., Takagi, R. et Snieder, R. (2015). Depth-dependence of seismic velocity change associated with the 2011 Tohoku

earthquake, Japan, revealed from repeating earthquake analysis and finite-difference wave propagation simulation. *Geophysical Journal International*, 201(2):741–763.

Schoenberg, M. (1980). Elastic wave behavior across linear slip interfaces. *The Journal of the Acoustical Society of America*.

Seiler, K.-P. et Gat, J. (2007). Mechanisms and Processes of Recharge. pages 31–68. Springer, Dordrecht.

Sens-Schönfelder, C., Snieder, R. et Li, X. (2018). A Model for Nonlinear Elasticity in Rocks Based on Friction of Internal Interfaces and Contact Aging. *Geophysical Journal International*.

Sens-Schönfelder, C. et Wegler, U. (2006). Passive image interferemetry and seasonal variations of seismic velocities at Merapi Volcano, Indonesia. *Geophysical Research Letters*, 33(21):L21302.

Shapiro, N. M. et Campillo, M. (2004). Emergence of broadband Rayleigh waves from correlations of the ambient seismic noise. *Geophysical Research Letters*, 31(7).

Shapiro, N. M., Campillo, M., Stehly, L. et Ritzwoller, M. H. (2005). High-resolution surface-wave tomography from ambient seismic noise. *Science*.

Shapiro, N. M., Ritzwoller, M. H. et Bensen, G. D. (2006). Surce location of the 26 sec microseism from cross-correlations of ambient seismic noise. *Geophysical Research Letters*, 33(18).

Shen, W., Ritzwoller, M. H., Schulte-Pelkum, V. et Lin, F.-C. (2012). Joint inversion of surface wave dispersion and receiver functions : a Bayesian Monte-Carlo approach. *Geophysical Journal International*.

Silver, P. G., Daley, T. M., Niu, F. et Majer, E. L. (2007a). Active source monitoring of cross-well seismic travel time for stress-induced changes. *Bulletin of the Seismological Society of America*, 97(1 B):281–293.

Silver, P. G., Daley, T. M., Niu, F. et Majer, E. L. (2007b). Active source monitoring of cross-well seismic travel time for stress-induced changes. *Bulletin of the Seismological Society of America*.

Snieder, R. et Beukel, A. (2004). The liquefaction cycle and the role of drainage in liquefaction. *Granular Matter*, 6:1–9.

Stehly, L., Campillo, M., Froment, B. et Weaver, R. L. (2008). Reconstructing Green's function by correlation of the coda of the correlation (C3) of ambient seismic noise. *Journal of Geophysical Research : Solid Earth*.

Stehly, L., Campillo, M. et Shapiro, N. M. (2006). A study of the seismic noise from its long-range correlation properties. *Journal Of Geophysical Research-Solid Earth*.

Stehly, L., Cupillard, P. et Romanowicz, B. (2011). Towards improving ambient noise tomography using simultaneously curvelet denoising filters and SEM simulations of seismic ambient noise. *Comptes Rendus - Geoscience*.

Stehly, L., Fry, B., Campillo, M., Shapiro, N. M., Guilbert, J., Boschi, L. et Giardini, D. (2009). Tomography of the Alpine region from observations of seismic ambient noise. *Geophysical Journal International*.

Stein, S. et Wysession, M. (2003). *An introduction to seismology, earthquakes, and earth structure*. Blackwell Pub.

Sun, T., Wang, K., Iinuma, T., Hino, R., He, J., Fujimoto, H., Kido, M., Osada, Y., Miura, S., Ohta, Y. et Hu, Y. (2014). Prevalence of viscoelastic relaxation after the 2011 Tohoku-oki earthquake. *Nature*, 514(7520):84–87.

Taira, T. et Brenguier, F. (2016). Response of hydrothermal system to stress transients at Lassen Volcanic Center, California, inferred from seismic interferometry with ambient noise. *Earth, Planets and Space*, 68(1):162.

Taira, T., Brenguier, F. et Kong, Q. (2015). Ambient noise-based monitoring of seismic velocity changes associated with the 2014 Mw 6.0 South Napa earthquake. *Geophysical Research Letters*, 42(17):6997–7004.

Talwani, P., Chen, L. et Gahalaut, K. (2007). Seismogenic permeability, ks. *Journal of Geophysical Research : Solid Earth*, 112(7):1–18.

Tiwari, V. M., Srinivas, N. et Singh, B. (2014). Hydrological changes and vertical crustal deformation in south India : Inference from GRACE, GPS and absolute gravity data. *Physics of the Earth and Planetary Interiors*.

Toksoz, M. N. et Lacoss, R. T. (1968). Microseisms : Mode Structure and Sources. *Science*, 159(3817):872–873.

Tonegawa, T., Hirahara, K. et Shiomi, K. (2006). Upper mantle imaging beneath the Japan Islands by Hi-net tiltmeter recordings. *Eath Planet Space*, 58:1007–1012.

Tonegawa, T., Nishida, K., Watanabe, T. et Shiomi, K. (2009). Seismic interferometry of teleseicmic S-wave coda for retrieval of body waves : An application to the Philippine Sea slab underneath the Japanese Islands. *In Geophysical Journal International*.

Trinh, P.-T., Brossier, R., Métivier, L., Tavard, L., Virieux, J. et Wellington, P. (2017). Efficient 3D elastic FWI using a spectral-element method on Cartesian-based mesh. *In SEG Technical Program Expanded Abstracts 2017*, pages 1533–1538. Society of Exploration Geophysicists.

Tsai, V. C. (2011). A model for seasonal changes in GPS positions and seismic wave speeds due to thermoelastic and hydrologic variations. *Journal of Geophysical Research : Solid Earth*, 116(4):1–9.

Uchida, N. et Matsuzawa, T. (2013). Pre- and postseismic slow slip surrounding the 2011 Tohoku-oki earthquake rupture. *Earth and Planetary Science Letters*, 374:81–91.

Wang, Q. Y., Brenguier, F., Campillo, M., Lecointre, A., Takeda, T. et Aoki, Y. (2017). Seasonal Crustal Seismic Velocity Changes Throughout Japan. *Journal of Geophysical Research : Solid Earth*.

Wapenaar, K. et Fokkema, J. (2006). Green's function representations for seismic interferometry. *GEOPHYSICS*.

Watanabe, S. I., Sato, M., Fujita, M., Ishikawa, T., Yokota, Y., Ujihara, N. et Asada, A. (2014). Evidence of viscoelastic deformation following the 2011 Tohoku-Oki earthquake revealed from seafloor geodetic observation. *Geophysical Research Letters*, 41(16):5789–5796.

Watson, K. M., Bock, Y. et Sandwell, D. T. (2002). Satellite interferometric observations of displacements associated with seasonal groundwater in the Los Angeles basin. *Journal of Geophysical Research : Solid Earth*.

Weaver, R., Froment, B. et Campillo, M. (2009). On the correlation of non-isotropically distributed ballistic scalar diffuse waves. *The Journal of the Acoustical Society of America*.

Weaver, R. et Lobkis, O. (2002). On the emergence of the Green's function in the correlations of a diffuse field : Pulse-echo using thermal phonons. *In Ultrasonics*.

Weaver, R. L. (1982). On diffuse waves in solid media. *The Journal of the Acoustical Society of America*.

Weaver, R. L. et Lobkis, O. I. (2001). Ultrasonics without a source : Thermal fluctuation correlations at mhz frequencies. *Physical Review Letters*.

Weaver, R. L. et Lobkis, O. I. (2004). Diffuse fields in open systems and the emergence of the Green's function (L). *The Journal of the Acoustical Society of America*.

Wegler, U., Nakahara, H., Sens-Schönfelder, C., Korn, M. et Shiomi, K. (2009). Sudden drop of seismic velocity after the 2004 Mw 6.6 mid-Niigata earthquake, Japan, observed with Passive Image Interferometry. *Journal of Geophysical Research*, 114(B6):B06305.

Wegler, U. et Sens-Schönfelder, C. (2007). Fault zone monitoring with passive image interferometry. *Geophysical Journal International*, 168(3):1029–1033.

Williams, S. D. et Penna, N. T. (2011). Non-tidal ocean loading effects on geodetic GPS heights. *Geophysical Research Letters*.

Yamagiwa, S., Miyazaki, S., Hirahara, K. et Fukahata, Y. (2015). Afterslip and viscoelastic relaxation following the 2011 Tohoku-oki earthquake (Mw9.0) inferred from inland GPS and seafloor GPS/Acoustic data. *Geophysical Research Letters*, 42(1):66–73.

Yamamura, K., Sano, O., Utada, H., Takei, Y., Nakao, S. et Fukao, Y. (2003). Long-term observation of in situ seismic velocity and attenuation. *Journal of Geophysical Research*, 108(B6):2317.

Yang, Y., Ritzwoller, M. H., Levshin, A. L. et Shapiro, N. M. (2007). Ambient noise Rayleigh wave tomography across Europe. *Geophysical Journal International*.

Yao, H., Beghein, C. et Van Der Hilst, R. D. (2008). Surface wave array tomography in SE Tibet from ambient seismic noise and two-station analysis - II. Crustal and upper-mantle structure. *Geophysical Journal International*.

Yao, H. et van der Hilst, R. D. (2009). Analysis of ambient noise energy distribution and phase velocity bias in ambient noise tomography, with application to SE Tibet. *Geophysical Journal International*.

Young, M. K., Rawlinson, N. et Bodin, T. (2013). Transdimensional inversion of ambient seismic noise for 3D shear velocity structure of the Tasmanian crust. *GEOPHYSICS*.

Zhan, Z., Ni, S., Helmberger, D. V. et Clayton, R. W. (2010). Retrieval of Moho-reflected shear wave arrivals from ambient seismic noise. *Geophysical Journal International*.

Zhan, Z., Tsai, V. C. et Clayton, R. W. (2013). Spurious velocity changes caused by temporal variations in ambient noise frequency content. *Geophysical Journal International*, 194(3):1574–1581.